2022-12-19

Short-Range Magnetic Correlations, Spontaneous Magnetovolume Effect, and Local Distortion in Magnetic Semiconductor MnTe

Raju Baral
Brigham Young University

Short-Range Magnetic Correlations, Spontaneous Magnetovolume Effect, and Local Distortion in Magnetic Semiconductor MnTe

Raju Baral

A dissertation submitted to the faculty of
Brigham Young University
in partial fulfillment of the requirements for the degree of

Doctor of Philosophy

Benjamin A. Frandsen, Chair
Richard Vanfleet
Karine Chesnel
John Colton
David Neilsen

Department of Physics and Astronomy

Brigham Young University

ABSTRACT

Short-Range Magnetic Correlations, Spontaneous Magnetovolume Effect, and Local Distortion in Magnetic Semiconductor MnTe

Raju Baral
Department of Physics and Astronomy, BYU
Doctor of Philosophy

The antiferromagnetic semiconductor MnTe has recently attracted significant interest as a potential high-performance thermoelectric material. Its promising thermoelectric properties are due in large part to short-range magnetic correlations in the paramagnetic state, which enhance the thermopower through the paramagnon drag effect. Using magnetic pair distribution function (mPDF) analysis of neutron total scattering data, we present a detailed, real-space picture of the short-range magnetic correlation in MnTe, offering a deeper view into the paramagnon drag effect and the nature of the correlated paramagnetic state. We confirm the presence of nanometer-scale antiferromagnetic correlations far into the paramagnetic state, show the evolution of the local magnetic order parameter across the Néel temperature $T_N = 307$K, and discover a spatially anisotropic magnetic correlation length. By combing our mPDF analysis with traditional atomic PDF analysis, we also gain detailed knowledge of the magnetostructural response in MnTe. We observed a spontaneous volume contraction of nearly 1%, the largest spontaneous magnetovolume effect reported so far for any antiferromagnetic system. The lattice strain scales linearly with the local magnetic order parameter, in contrast to the quadratic scaling observed for the conventional magnetostriction properties of this technologically relevant material. Using neutron and X-ray PDF analysis, we also investigated the local distortion on MnTe and Mn-based systems, MnS and MnO as a function of temperature. Such local distortion on MnTe increases with the rise in temperature and becomes more pronounced at 500 K.

Keywords: atomic pair distribution function, magnetic pair distribution function, thermoelectric effect, paramagnon drag, antiferromagnetism, short-range magnetism, local structure, magnetostructural coupling, emphanisis

ACKNOWLEDGMENTS

This research was made possible through a collaborative effort with excellent people and scholars over the course of my graduate career. I have the absolute honor and privilege to acknowledge some of them by name here at the start of my thesis.

First and foremost, I would like to express deepest gratitude to my research advisor, Dr. Benjamin A. Frandsen in the Department of Physics and Astronomy. I will always be grateful for his constant encouragement, patient guidance, the knowledge and wisdom he has imparted to me, and the trust and confidence he has expressed in me over the course of these 3 and a half years. I have utmost pride and respect of his professional and personal accomplishments.

I would also like to extend my acknowledgment to Braedon Jones, a student in Dr. Frandsen's lab, and all the other teammates in the Frandsen group. I thank the graduate coordinator of the Department of Physics and Astronomy Dr. Richard Vanfleet, for countless advice and support throughout my degree. I am also grateful to Dr. Karine Chesnel, Department of Physics and Astronomy, and Dr. Stacey J. Smith, Department of Chemistry and Biochemistry for allowing me to use their research laboratory equipment. Lastly, I would like to recognize the efforts of my friends, Aadesh Neupane and Aatish Neupane, for their assistance with python.

I also acknowledge the efforts and hard work of my collaborators and coauthors on the papers that I have published based on the research presented in this thesis. I would also like to recognize the work of the scientific and administrative staff at the experimental facilities Oak Ridge National Laboratory and Brookhaven National Laboratory where the research for this thesis has been conducted. None of this would have been possible without the support provided by our funding agency, Department of Energy (DOE), Office of Science, Office of Basic Energy Sciences through grant No. DE-SC0021134.

I express appreciation to my graduate advisory committee, who have shared their time and knowledge to help me through my PhD program. My committee members include Dr. Richard Vanfleet, Dr. Karine Chesnel, Dr. John Colton, and Dr. David Neilsen, chaired by Dr. Benjamin Frandsen.

Finally, I would like to acknowledge the immense support and love that I have received from my family. My wife, my confidant, Ayushma, who I owe my everything; my parents who are my biggest strength; my siblings, who have constantly encouraged me beyond limits.

Contents

List of Figures

Chapter 1

Local magnetic correlations, thermoelectrics and paramagnon drag effect

1.1 Introduction

The functional properties of many technologically useful materials depend crucially on their local structure. Local structure refers to the atomic and magnetic correlation on a local length scale from one to several interatomic distances. For many materials, local structure correlations are different from the average structure, and it is very important to understand those local structures along with the average long-range structures to understand the many exotic properties of the materials if we want to develop technologically functional devices. Fig. 1.1 represents the schematic illustration of local ferroelectric correlations that are well-defined over short-length scales but average to zero over longer-length scales, rendering them undetectable with conventional probes of the average structure [1]. Although this example is for locally correlated atomic displacements that give rise to short-range ferroelectricity, similar behavior can be observed in numerous other types of structural and magnetic correlations in materials. Therefore, the understanding and exploiting of

many materials depend on characterizing not only the average periodic structure but also the local structures (which often deviates from the average structure).

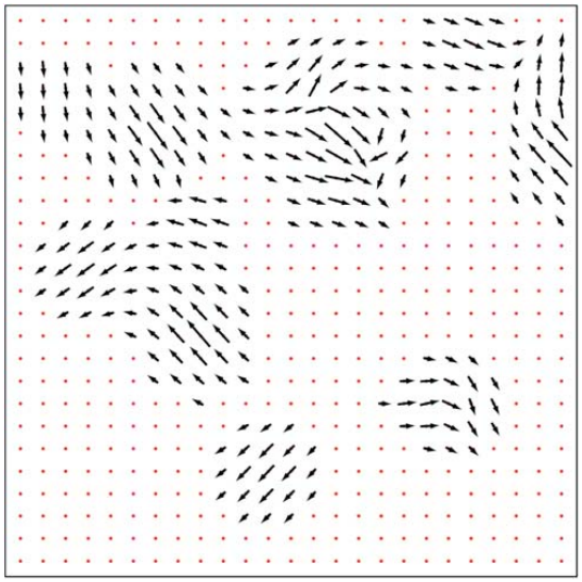

Figure 1.1 Local magnetic structures of ferroelectric domains. Figure adapted from [1].

1.2 Average and local structure

Bragg's law is widespread in the world of crystallography and is the fundamental foundation of diffraction experiments for structure determination. Bragg peaks observed in a diffraction pattern provide information about the average or global structure of the material, such as the average position, displacement, and occupancy of atoms in the unit cell. However, Bragg scattering is blind to short-range correlations that may deviate from the average structure, and yet it is precisely the local-level correlations that are most directly related to the interactions present in the material. Additionally, Bragg's law is based on the periodicity of the structure and cannot be applied if the crystal is not periodic, for example, in liquid and glass materials. Bragg's law likewise requires modification if the material has a very small particle size, for instance, a nanoparticle or bulk material

having a structure of few nanometers. Many materials like colossal magnetoresistive manganites, high-temperature superconductors, and ferroelectric materials have a complex structures due to their competing internal forces [9]. Such materials can have well-defined structural correlations on a local scale of about 1 to 100 nanometers, which we call the local structure, which nevertheless averages away to zero over longer length scales. Local structure is commonly observed in disordered materials where the material has defects or correlated disorder on the local scale and is not reflected in long-range crystallography. Similarly, amorphous solids, polymers, and nanostructures also have well-defined local structures while lacking long-range periodicity. Our understanding of the local structure on the atomic level can provide us with a fundamental understanding of many functional materials and how they work, making the study of local structure a crucial counterpart to studies of the average structure. Since conventional diffraction analysis of Bragg peaks is not sensitive to short-range correlations comprising the local structure, alternative techniques must be used. The technique of choice for this project is pair distribution function (PDF) analysis, which will be explained in detail later.

1.3 Short-range and long-range magnetic correlations

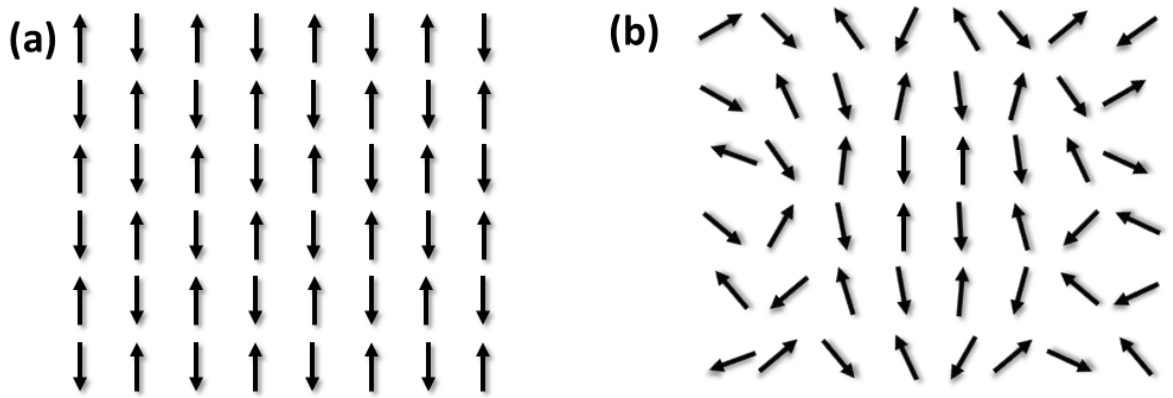

Figure 1.2 (a) Long-range and (b) short-range magnetic structure.

While the general notion of the structure of a solid is typically considered in terms of the atomic structure of materials, i.e. the spatial arrangement of the atoms comprising the solid, other important components of the overall structure may also be present. For example, in materials containing atoms with unpaired electrons, magnetic moments will be present in the solid, leading to the idea of the magnetic structure. Magnetic structure refers to the spatial arrangement of the relative orientation of the magnetic moments in the solid. As with atomic structure, the magnetic structure can have a long-range, periodic component as well as short-range correlations that average to zero over a long distance. Fig. 1.2 (a) shows a schematic illustration of long-range magnetic correlations, called as such because there is a well-defined pattern of relative orientations over a very long distance. This is a long-range antiferromagnetic magnetic structure because it has up-and-down alternating spins over very long distances. Due to the long-range periodicity of the magnetic arrangement, the spin correlation function for such long-range magnetic order is non-zero,

$$\lim_{r\to\infty} \langle S_0 \cdot S_i \rangle (r) \neq 0. \tag{1.1}$$

This is something that we expect for the long-range magnetic order. Any arbitrary spin at the origin (S_0) has a well-defined correlation with other spins S_i in the lattice. For example, referring to Fig. 1.2 (a), one can choose any arbitrary spin at the origin, and it forms an antiferromagnetic alignment with its first neighbor spins, whereas it makes ferromagnetic alignment with the second nearest spins, and again antiferromagnetic alignment with third spins, and so on. Such magnetic correlations exist for a very long distance in the case of a long-range magnetic system (infinitely long for an infinite crystal), and the average magnetic spin correlation for such a magnetic structure is non-zero.

In contrast, short-range magnetic correlations remain well defined and nonzero only over a finite separation distance, for example only a few inter-atomic spacing. A schematic picture of short-range-correlated magnetic moments in a small region of the material is shown in Fig. 1.2 (b). At first glance, it might look completely random but when looking in the center, there is a clear net preference for antiferromagnetic alignment over short distances. As we go further away, the spins

look more and more random and are less and less correlated. This type of magnetic correlation is called short-range magnetic correlation, where the spins are partially well-defined only to a few atoms and appear completely random at longer distances. The average spin correlation function for such a magnetic system is zero for long distances ($r \to \infty$),

$$\lim_{r\to\infty} \langle S_0 \cdot S_i \rangle (r) = 0. \tag{1.2}$$

However, we can still use the average spin correlation function to quantify how ordered two spins are with each other. It has been found that the local spin correlation function for short-range order die exponentially with inter-atomic distances,

$$\langle S_0 \cdot S_i \rangle (r) \sim e^{-r/\xi} \tag{1.3}$$

Here, r represents the inter-atomic distance and ξ is an exponential correlation length of these spins. This thesis focuses on the study and visualization of such type of magnetism, i.e., short-range magnetic order.

1.4 Thermoelectricity, the thermoelectric figure of merit, and paramagnon drag

Thermoelectric materials hold tremendous promise for energy applications. Such materials utilize a temperature gradient to induce an electrical voltage through the diffusion of charge carriers in response to the thermal gradient. For example, thermoelectric devices can use exhausted heat from vehicles or industries to obtain electricity and can provide novel possibilities for thermal energy harvesting or solid-state refrigeration [10–12]. But the recent challenge in the field of thermoelectrics is to find new materials or design existing materials that possess excellent thermoelectric properties, while also being economically and environmentally viable. The performance of a thermoelectric

material depends directly on the dimensionless thermoelectric figure of merit (zT) given by

$$zT = \frac{S^2 T}{\rho \kappa}, \tag{1.4}$$

where ρ is the electrical resistivity, S is the Seebeck coefficient (i.e., thermopower), T is temperature, and κ is the thermal conductivity. It should be noted that the value of S, ρ, and κ depends on temperature. By referring to equation 1.4, we can enhance the value of zT by lowering the values of ρ, and κ. However, it is extremely difficult to optimize both of them simultaneously for any material as they are interrelated in such a way that lowering the value of ρ will typically increase the value of κ, thus canceling out the overall effect in the thermoelectric figure of merit (zT). Hence, there is a relative scarcity of high-performance thermoelectrics. Significant effort has been dedicated to finding ways around the counteracting tendencies of the resistivity and thermal conductivity, e.g. through defect engineering or nanostructuring [13]. However, it remains an outstanding challenge to find thermoelectric materials suitable for widespread use.

One rather less-explored route toward higher zT values is to exploit the magnetic degree of freedom in metals and semiconductors with unpaired electrons. An example of this is magnon drag, wherein a flux of magnons (i.e. spin waves, or thermal excitations of the long-range magnetic ordering pattern) drags charge carriers through the lattice via exchange of linear momentum as shown in a Fig. 1.3, thereby enhancing the thermopower [14–16]. The requirement to have long-range magnetic order that supports well-defined magnons would appear to limit the applicability of magnon drag, particularly since magnetic order is typically weakened at high temperatures, where thermoelectric devices are most likely to be useful. However, it was recently shown that the thermopower can be enhanced even by short-range magnetic correlations, rather than true long-range order, through "paramagnon drag" [3, 17]. Analogous to magnons, paramagnons are thermal excitations in a partly correlated paramagnetic state, i.e. a state where the magnetic moments maintain short-range correlations even in the absence of long-range magnetic order. If the local magnetic correlations have a sufficiently long length and lifetime, paramagnons will look

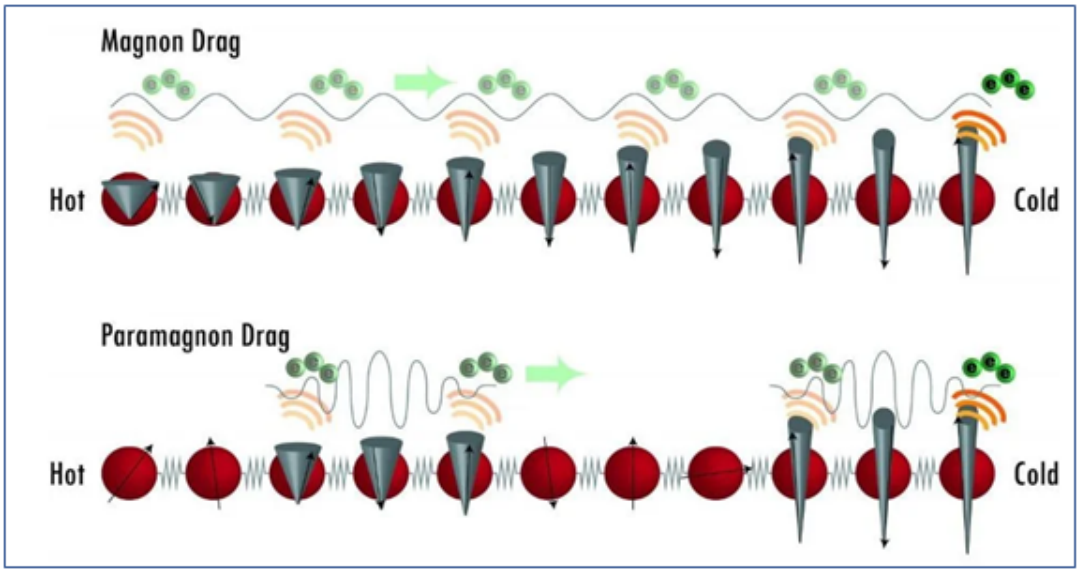

Figure 1.3 Magnon and paramagnon drag effect while transporting the electrons through the material. (Figure adapted from [2])

like magnons on the time- and length-scales of their interactions with itinerant charge carriers, allowing a paramagnon flux to enhance the thermopower in like fashion as magnon drag. Thus, magnetic enhancement of zT through drag effects is much more widely applicable than initially supposed, encompassing not only the relatively few materials with a well-ordered magnetic state at very high temperatures but also the class of materials with lower-temperature magnetic transitions that nevertheless retain significant short-range magnetic correlations to elevated temperatures, e.g., as afforded by large exchange interactions. Therefore, the discovery of paramagnon drag constitutes an important advancement in the field of thermoelectrics. It opens up a new tuning mechanism to enhance zT and turns the broad class of magnetic semiconductors into potential high-performance thermoelectric candidates. Large portions of this dissertation are focused on gaining an understanding of the short-range magnetic correlations giving rise to paramagnon drag in the antiferromagnetic semiconductor MnTe.

1.5 MnTe

MnTe is a layered hexagonal system with an electronic band gap of 1.3 eV. This compound has attracted significant interest since 1960s [18]due to its unusual combination of physical properties and its potential applications to technology. MnTe is one of the few 3*d* transition metal binary compounds that exhibits semiconducting transport properties [19]. The Mn^{2+} (S = 5/2) magnetic moments in MnTe order antiferromagnetically below $T_N = 307$ K [20], such that the spins align ferromagnetically within hexagonal sheets(along *ab* plane) and antiferromagnetically between sheets (along *c* - axis) [21] as shown in Fig. 1.4 (a). This property of MnTe has received particular enthusiasm in recent years due to intense excitement surrounding the application of antiferromagnetic semiconductors for spintronics [22–24].

Most relevant to this project, MnTe also possesses a sizeable thermoelectric response at elevated temperatures, adding to the technological importance of MnTe [19]. From a more fundamental perspective, MnTe has also attracted interest as a "crossroads" material [25, 26] because it shares characteristics of both strongly correlated Mott or charge-transfer insulators (e.g., narrow *d* bands) and also weakly correlated band insulators (e.g., the significant overlap of *p* and *d* orbitals), giving rise to rich and varied electronic and magnetic properties. Interestingly, the antiferromagnetism of MnTe appears to be closely tied to its thermoelectric behavior, and this is evidenced by a large response of the resistivity and Seebeck coefficient to the antiferromagnetic transition [21].

Returning to the thermoelectric properties of MnTe, it displays outstanding zT values when lightly doped with Li, Na, or Ag, approaching 1 around 800 -900 K [3, 19, 27, 28]. Fig. 1.4 (b) represents the variation of thermoelectric figure of merit for Li-doped MnTe as a function of temperature and there is clear evidence that with a very small amount of doping on MnTe effectively increases the value of zT at elevated temperature.

A recent study on Li-doped MnTe using inelastic neutron scattering techniques provides strong evidence that paramagnon drag is primarily responsible for the large zT value in doped MnTe [3]. In

fact, calculations have indicated that the observed zT is approximately a factor of 3 larger than the expected value if spin effects were absent [29]. The diffuse neutron scattering intensity observed in the paramagnetic state at 360 K, shown by the green diffuse intensity in Fig. 1.4 (c), is clear evidence of short-range magnetic correlations persisting above the long-range magnetic ordering temperature of 307 K. It has been argued that these short-range magnetic correlations have a sufficiently long lifetime and correlation length to trigger the paramagnon drag effect on MnTe [3].

The Paramagnon drag effect has been observed only in a small handful of materials [17], of which MnTe is the most prominent. Significantly, it has been shown to be relevant for both ferromagnets and antiferromagnets, which broadens its potential impact on the search for high-performance thermoelectrics [17]. However, paramagnon drag is still a relatively new phenomenon, and much remains to be understood regarding the fundamentals of this effect and how it can be most effectively utilized to identify or engineer promising thermoelectric materials. The proper understanding of the short-range magnetic correlations giving rise to paramagnon drag in MnTe and other thermoelectric materials is a crucial next step for progress in this field. So far, there is little work that directly investigates the nature of the short-range magnetic correlations in MnTe and other thermoelectric materials.

The experimental investigation of MnTe has been limited to bulk probes that are sensitive to the average structure and properties, such as conventional X-ray/neutron scattering, resistivity, magnetization, and thermodynamic measurements. However, in both thermoelectrics and spintronics materials like doped magnetic semiconductors, the local structure plays an important role in understanding material performance. In thermoelectrics, point defects and other forms of the nanoscale disorder can have a tremendous influence on thermal conductivity, significantly affecting the value of zT [30]. In magnetic semiconductors, the effect of dopants on their local environment in the host material can determine the effectiveness of magnetic coupling between neighboring moments [31]. Therefore, the experimental techniques that can probe local atomic and magnetic

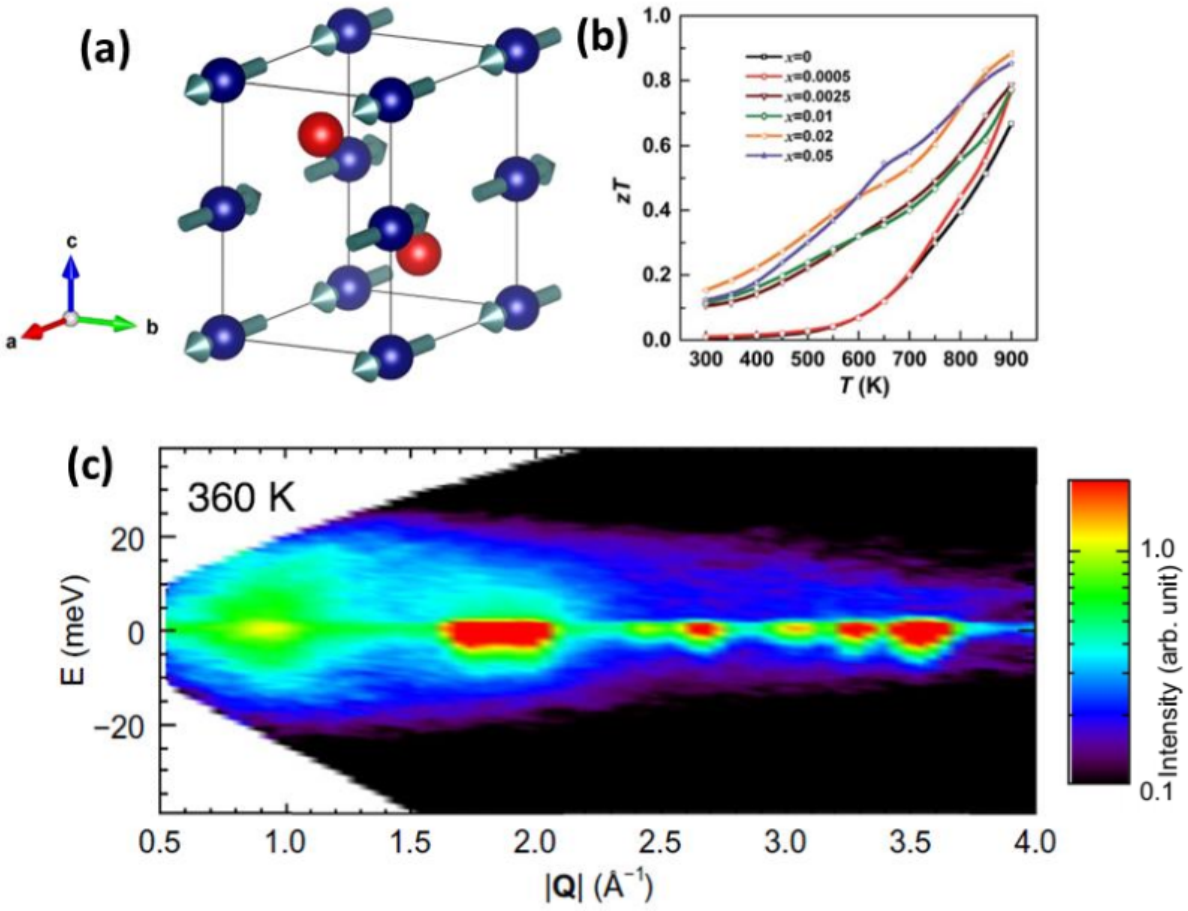

Figure 1.4 (a) Crystal structure of MnTe with moments. Blue and red spheres represent Mn and Te atoms respectively. (b) Variation of thermoelectric figure of merit(zT) as a function of the temperature of Li-doped MnTe (c) Inelastic scattering of MnTe at 360 K. Figure (b) and (c) are adapted from [3]

structures are necessary for advancing our understanding of MnTe.

In this thesis, I will use neutron and X-ray total scattering techniques, which are powerful probes of local structure, to study pure MnTe and Na-doped MnTe, using both one-dimensional (1D) and three-dimensional (3D) magnetic pair distribution function [6, 32–34] analysis. I will analyze real-space reconstructions of short-range antiferromagnetic correlations above the transition temperature to better understand paramagnon effects in pure MnTe and Na-doped MnTe. Using both atomic and magnetic pair distribution function (PDF and mPDF) data collected over a wide

temperature range, I will present a detailed picture of the evolution of the local atomic and magnetic structure of MnTe. Key results include quantitative characterization of the short-range magnetic correlations in the paramagnetic state above the transition temperature, observation of large and unconventional magnetostructural coupling across the magnetic transition, and analysis of a large and highly localized short-range distortion in pure and doped MnTe that grows with temperature. Along with neutron total scattering, I will highlight results of *ab initio* calculations of the magnetic correlations to achieve a comprehensive picture of the short-range AF correlations underlying the paramagnon drag effect in MnTe.

1.6 Outline of this thesis

The outline of this thesis is as follows. In Chapter 2, I will introduce atomic and magnetic pair distribution function (PDF) techniques, including one-dimensional and three-dimensional PDF analysis. In Chapter 3, I will introduce the experimental preparation details of the pure MnTe and 2% Na-doped MnTe, laboratory X-ray diffraction, and magnetic characterization of these materials. In Chapter 4, I will present the short-range magnetic correlations and paramagnon drag effect on these materials. In Chapter 5, I will discuss the magnetostructural and magnetovolume effects and in the last Chapter 6, I will present the local distortion of MnTe.

Chapter 2

Methods

2.1 Scattering

Scattering refers to the collision of particles (neutrons, electrons, photons, etc) with atoms or molecules. In diffraction experiments, the sample is illuminated by the beam of X-rays/neutrons, and we measure the intensity of the diffracted beam as a function of momentum transfer of the incident particles, which can be determined from the scattering angle (2θ) and the wavelength [32]. The scattered beam contains lots of information about the material, such as its atomic/nuclear structure (i.e. the spatial arrangement of the atoms) and magnetic structure (i.e. the spatial arrangement and orientation of the magnetic moments). Here, our purpose is to analyze the total scattering intensity to study local atomic and magnetic structure of the material of interest. The total scattering intensity is composed of several factors, including coherent (I_{coh}) and incoherent (I_{incoh}) intensity, multiple scattering (I_M) intensity, and background intensity (I_B).

$$I_{total} = I_{coh} + I_{incoh} + I_B + I_M \tag{2.1}$$

Multiple scattering can occur within the sample, whereas the sample holder, air, etc are responsible for the Background intensity. The background intensity can be measured as the observed intensity

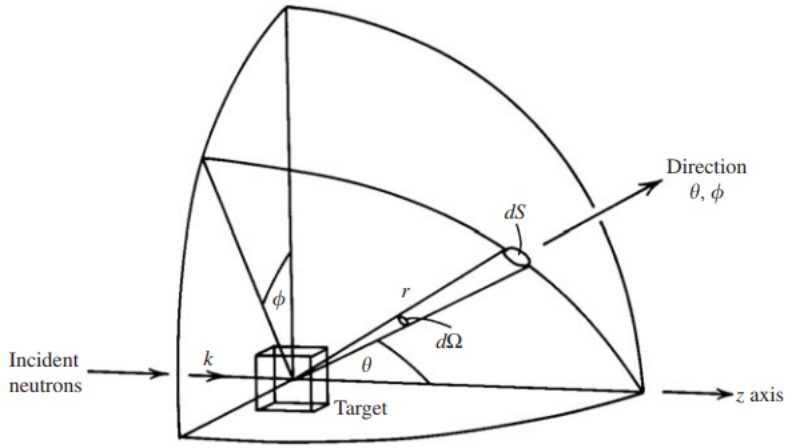

Figure 2.1 The geometry of neutron scattering experiment (Marshall and Lovesey 1971; Squires 1978).

without the sample inside the sample holder. The common causes of incoherent intensity are Compton scattering (for X-ray beams) and nuclear spin scattering (for neutron beams). All the informations about the structure and lattice dynamics are contained in the coherent scattering intensity. The coherent scattering intensity can further be expressed using scattering cross-section ($\frac{d\sigma_c}{d\Omega}$) as

$$I_c = APC\frac{d\sigma_c}{d\Omega} \tag{2.2}$$

where A, P, and C represent the absorption factor, polarization factor, and normalization factor, respectively [32]. To have a better understanding of scattering, I now present the basic theory of neutron scattering.

2.2 Basic theory of neutron scattering

Neutrons are uncharged particles that can interact with nuclei of any material through a strong nuclear force. The interaction of neutrons with the nuclei and the magnetic moments in the material can provide a lot of information about the nuclear and magnetic structure of the material. During

neutron scattering experiments, the incident neutrons interact primarily with nuclei and get scattered. If the material is magnetic, neutrons also get scattered from the magnetic moments.

A geometrical diagram of neutron scattering is shown in Fig. 2.1. Let the incident neutron have wave-vector $\mathbf{k}$ and state vector ψ_k. After scattering, the wave-vector is $\mathbf{k}'$ and state vector is $\psi_{k'}$, respectively. The scattering vector is represented by $\mathbf{Q}$ and is given $\mathbf{Q} = \mathbf{k} - \mathbf{k}'$. The scattered flux of neutrons detected by the detector of the angular element $d\Omega(= sin\theta\Delta\theta\Delta\phi)$ is given by

$$I(\theta,\phi) = N\frac{d\sigma}{d\Omega}d\Omega, \tag{2.3}$$

where N is the incident neutron flux (neutrons per second per unit area), $d\sigma/d\Omega$ is the differential scattering cross-section and (θ,ϕ) are the polar coordinates of the position of the detector. In a neutron scattering experiment, we measure the differential cross-section as a function of the direction of scattered particles or, equivalently, the momentum transfer ($\hbar\mathbf{Q}$) [35].

Let us assume elastic scattering where the energy of the incident neutron is equal to the scattered neutron. For any scattering experiment, we need to calculate the differential cross-section, and the calculation of the differential cross-section is done by using Fermi's Golden Rule, which gives the probability per unit time of transition from a state defined by wave-vector $\mathbf{k}$ to the state defined by wave-vector $\mathbf{k}'$, both having same energy $E = \frac{\hbar^2}{2m}$. Fermi's Golden Rule can be written as,

$$W_{k\to k'} = \frac{2\pi}{\hbar}\left|\int d\mathbf{r}\,\psi^*_{\mathbf{k}'}\hat{V}\,\psi_{\mathbf{k}}\right|^2 \rho_{\mathbf{k}'(E)}. \tag{2.4}$$

Where $\hat{V}$ is the interaction potential that causes the transition i.e., the interaction between the incident neutron and the target sample, and $\rho_{\mathbf{k}'(E)}$ represent the density of final scattering states per unit energy range. For the material contained in a volume L^3, the initial and final states are represented by

$$\psi_{\mathbf{k}} = \frac{1}{L^{3/2}}e^{(i\mathbf{k}.\mathbf{r})} \tag{2.5}$$

and

$$\psi_{\mathbf{k}'} = \frac{1}{L^{3/2}}e^{(i\mathbf{k}'.\mathbf{r})}. \tag{2.6}$$

The density of the final states is given by

$$\rho_{\mathbf{k}'(E)} = \left(\frac{L}{2\pi}\right)^3 \frac{d\mathbf{k}'}{dE}. \tag{2.7}$$

For elastic scattering,

$$d\mathbf{k}' = k'^2 d\Omega dk' = k^2 d\Omega dk. \tag{2.8}$$

Additionally,

$$E = \hbar^2 k^2 / 2m \tag{2.9}$$

and

$$dE = \frac{\hbar^2 k}{m} dk \tag{2.10}$$

This gives

$$\rho_{\mathbf{k}'(E)} = \left(\frac{L}{2\pi}\right)^3 \frac{mk}{\hbar^2} d\Omega. \tag{2.11}$$

Now, we need to determine the incident flux of neutrons to calculate the differential cross-section.

$$\text{Incident flux} = (\text{velocity of neutrons})/L^3 = \frac{\hbar k}{mL^3}. \tag{2.12}$$

Combining Equations 2.4, 2.11, and 2.12, we get

$$\frac{d\sigma}{d\Omega} = L^6 \left(\frac{m}{2\pi\hbar^2}\right)^2 \left| \int d\mathbf{r}\, \psi^*_{\mathbf{k}'} \hat{V} \psi_{\mathbf{k}} \right|^2 d\Omega. \tag{2.13}$$

$$\frac{d\sigma}{d\Omega} = |\langle \mathbf{k}|\hat{V}|\mathbf{k}'\rangle|^2 \tag{2.14}$$

The simplified equation 2.14 is obtained after using the notation, $(\frac{L^3 m}{2\pi\hbar^2}) \int d\mathbf{r}\, \psi^*_{\mathbf{k}'} \hat{V} \psi_{\mathbf{k}} = \langle \mathbf{k}|\hat{V}|\mathbf{k}'\rangle$.

The equation 2.14 further can be written as a function of scattering amplitude ($f(\mathbf{Q})$) as follows,

$$\frac{d\sigma}{d\Omega} = |f(\mathbf{Q})|^2 \tag{2.15}$$

The scattering amplitude ($f(\mathbf{Q})$) provides the probability that the particles can be deflected/scattered in a certain direction and the rate of scattering is directly proportional to the incident flux of the particles [35].

2.3 Scattering length

The scattering length for the neutron is invariant with respect to the scattering angle and wavelength, so we can write it as

$$f(\mathbf{Q}) = -b. \tag{2.16}$$

The term b is called scattering length and is a complex quantity. The imaginary part is responsible for the absorption of the neutron, but for the very small absorption of the neutron, we can treat b as a real quantity. The negative sign in the above equation is just a matter of convention. The magnitude of b gives the strength of the scattering and its sign indicates whether the interaction between the nucleus and incident neutron is repulsive (positive b) or attractive (negative b). The value of scattering length can also vary with the isotope of the same element as well but does not vary with the atomic number in a monotonic way [36]. The typical value of scattering lengths for Mn and Te is -3.73(2) fm and 5.80(3) fm respectively [37].

2.4 Scattering through the assembly of nuclei

For the neutron scattering of the assembly of atoms the mean scattering potential (also called as pseudopotential) for the nucleus at position $\mathbf{r}_i$ is given by,

$$\hat{V} = \frac{2\pi\hbar^2}{m} b_i \delta(\mathbf{r} - \mathbf{r}_i), \tag{2.17}$$

We call it pseudopotential because it is not a real potential experienced by the neutrons near the nucleus instead it satisfies the requirement of the Born approximation for isotropic scattering [35],

$$\langle \mathbf{k}|\hat{V}|\mathbf{k}'\rangle = \frac{2\pi\hbar^2}{m} b_i \int d\mathbf{r}\, e^{(-i\mathbf{k}'\cdot\mathbf{r})}\, \delta(\mathbf{r} - \mathbf{r}_i)\, e^{(i\mathbf{k}\cdot\mathbf{r})} \tag{2.18}$$

$$= \frac{2\pi\hbar^2}{m} b_i \int e^{(i(\mathbf{k}-\mathbf{k}')\cdot\mathbf{r}_i)} \tag{2.19}$$

$$= \frac{2\pi\hbar^2}{m} b_i\, e^{(i\mathbf{Q}\cdot\mathbf{r}_i)} \tag{2.20}$$

Thus for the coherent scattering, the equation 2.14 reduces to:

$$\frac{d\sigma}{d\Omega} = \left| \sum_i b_i e^{(i\mathbf{Q}\cdot\mathbf{r}_i)} \right|^2 \tag{2.21}$$

$$= \sum_{i,j} b_i b_j e^{(i\mathbf{Q}\cdot(\mathbf{r}_i - \mathbf{r}_j))} \tag{2.22}$$

$$= \sum_{i,j} b_i b_j \, e^{(i\mathbf{Q}\cdot(\mathbf{r}_{ij}))} \tag{2.23}$$

This equation shows the relation between differential cross-section with interatomic correlations due to the appearance of term $\mathbf{r}_{ij}$ in phase factor.

2.5 Coherent and Incoherent neutron scattering

Different isotopes of the same element have different nuclear scattering lengths. As a result neutron scattering patterns typically include a flat background of scattering known as incoherent scattering. However, neutron scattering completely depends on σ and b of the scattering material. If the scattering sample is composed of the atoms of same species, the neutrons are scattered in the same way and this type of scattering is called coherent scattering. If the scattering sample is composed of dissimilar atoms, they have a mixture of scattering centers. Such mixtures of scattering can lead to randomness in the scattered neutrons because all the atoms cannot respond to the neutrons in an identical way. We may lose the constructive interference in the scattering pattern and this leads to incoherent neutron diffraction [38]. The total differential cross-section can be written as the sum of coherent and incoherent differential cross-section;

$$\frac{d\sigma}{d\Omega} = (\frac{d\sigma}{d\Omega})_{coherent} + (\frac{d\sigma}{d\Omega})_{incoherent}$$

2.6 Pair distribution function (PDF)

Pair distribution function (PDF) analysis of total scattering data is one of the foremost techniques for studying the local structure of materials. It is referred to as a total scattering technique because it considers both Bragg scattering (from the long-range, average structure) and diffuse scattering (from short-range, local structure) [9]. One of the important benefits of PDF analysis is that it can extract the structural information contained in the diffuse scattering in a direct and intuitive way through the Fourier transform of the total scattering data. Diffuse scattering provides important information on the local deviation of the structure from the average structure, but it takes the form of broad and diffuse patterns in reciprocal space which are often difficult to analyze. PDF is a technique that can be used to study such diffuse patterns directly in real space. The PDF is related to the probability of finding an atom with respect to another atom at a given distance r. It can be thought of as a map of inter-atomic distances in the material. By analyzing the PDF data on different length scales, one can obtain detailed information on the nano-scale as well as the average long-range structure of materials in an intuitive, real-space format.

The PDF is obtained experimentally by Fourier transforming the normalized total scattering pattern (including both Bragg and diffuse scattering), yielding the atom-atom and, if magnetic scattering is present, the spin-spin pair correlation functions in real space. This is expressed by the integral

$$f(r) = \frac{2}{\pi}\int_0^\infty Q(S(Q)-1)\sin Qr\, dQ \tag{2.24}$$

where $\hbar Q$ is the magnitude of the change in momentum experienced by the scattered neutrons or X-rays, $S(Q)$ is the total scattering structure-function (essentially the scattered intensity normalized by the average scattering length of the sample), and r is real-space distance.

For an arbitrary arrangement of atoms, the neutron scattering structure-function is given by

$$S(Q) = 1 + \frac{1}{N < b >^2}\sum_{i\neq j} b_i b_j (\frac{\sin Qr_{ij}}{Qr_{ij}}) \tag{2.25}$$

where N is the number of atoms, b_i is the neutron scattering length of atom i, $< b >$ is an average scattering length of all the atoms in the sample, and r_{ij} is the distance between atom i and j.

Using this expression for $S(Q)$ and substituting it into equation (2.24) (detail of the expression can be found on [32]), we get,

$$f(r) = \frac{1}{N < b >^2} \sum_{i \neq j} \left(\frac{1}{r} b_i b_j \delta(r - r_{ij}) \right). \tag{2.26}$$

This expression can be used to calculate the atomic PDF for an arbitrary structure [32], e.g. for comparison to the experimental data obtained through equation 2.24.

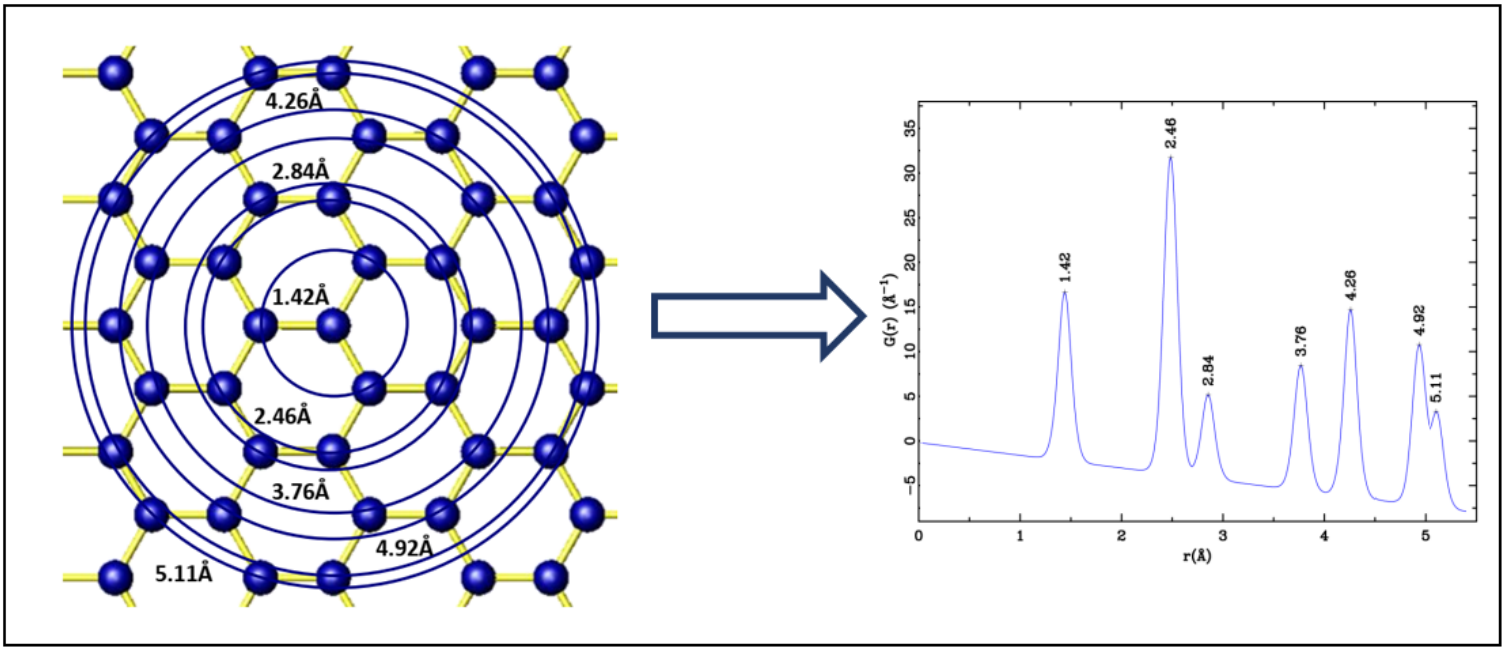

Figure 2.2 An example PDF pattern in real space. (Figure adapted from [4])

A typical PDF pattern in a real space is shown in figure 2.2. Peaks appear at atom-atom pair distances, which means the position of the peak gives us the average atom-atom bond length. For example, the first nearest atom's average bond length is about 1.42 Å, the second nearest atom's average bond distance is about 2.46 Å, and so on. Similarly, the area covered by the peak (the integrated intensity under the peak) gives us the coordination number. The peak width can also

provide the dynamic or static disorder of atom-atom pairs. For instance, the peak width as a function of temperature gives us information on the Debye temperature of a bond whereas the peak width as a function of atom-atom separation distance gives us information on correlated atomic dynamics. So, we can extract a lot of direct information just by observing the PDF pattern in real space. Additional details can be found in [32].

2.7 Experimental setup for total neutron scattering

The neutron total scattering experiments for this project were conducted primarily at the NOMAD beamline at the Spallation Neutron Source (SNS). Neutrons are produced at SNS through the collision of highly accelerated protons with heavy nuclei in a target (typically mercury). The neutrons produced in this process are slowed down via decoupled hydrogen moderator with an active surface area of 120 cm^2. These neutrons are then transported over the first 7 m through a system of fixed tapered Boron Nitride apertures, and from 7 m to 18.5 m, neutrons are transported through a super-mirror guide system, which is designed to increase the neutron flux. The last 2 m are mounted in an optic carousel and are hence removable. These neutrons finally fall on the sample mounted on the sample position which is surrounded by ^{3}He linear position-sensitive detectors to collect the scattered beam intensities [5]. The cut-away diagram of the NOMAD beamline is shown in Fig. 2.3.

Before proceeding to the experiment, we collect data from an empty sample container for the background subtraction. Then the powder sample is loaded in a vanadium can or quartz glass tube and is mounted on the sample position for the total neutron diffraction experiment at different temperatures. For our experiment at NOMAD, we used two different sample environments, a cryostat (2 K - 300 K) and a Nitrogen flow cryostream (100 K - 500 K). Once we get the data for our sample we always do the background subtraction using the data of the empty sample container.

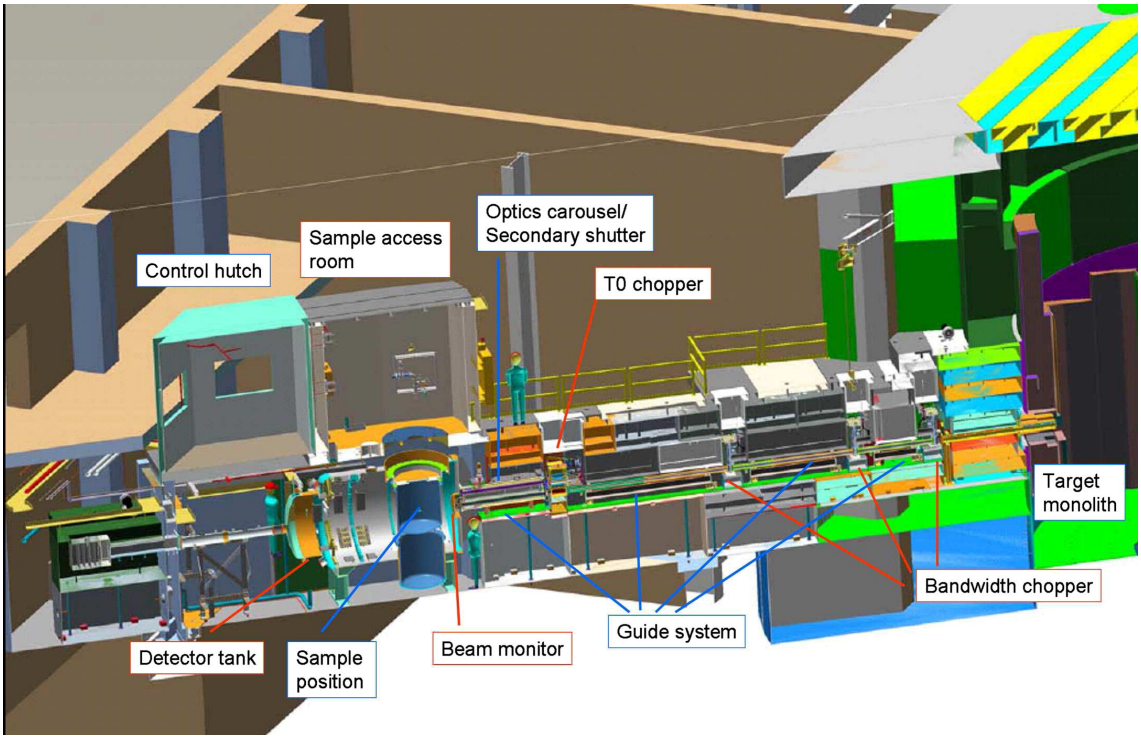

Figure 2.3 Cut-away overview diagram of NOMAD beamline. (Figure adapted from [5])

Temperature-dependent neutron total scattering experiments were performed on powder pure MnTe as well as Na-doped MnTe at the Nano Scale-Ordered Material Diffractometer (NOMAD) at the Spallation Neutron Source (SNS) of Oak Ridge National Laboratory (ORNL) [5]. The powder samples were loaded in quartz capillaries inside an argon glove box. The total scattering patterns were collected at several temperatures between 100 K to 500 K. The total neutron scattering data were reduced and transformed with $Q_{\text{max}} = 25$ Å^{-1} using the automatic data reduction scripts at NOMAD. The atomic and magnetic PDF analyses were performed using the DIFFPY suite [39] together with the diffpy.mpdf package for the mPDF calculations and fits. Additional descriptions of the mPDF technique and analysis are provided in Chapter 3, including details about how we account for the magnetic form factor.

Similarly, single crystal neutron diffraction patterns were collected at various temperatures on the CORELLI instrument [40] at the SNS using neutrons with incident energies between 10 and

200 meV. The crystal was oriented such that the *H*0*L* reciprocal space plane coincided with the horizontal scattering plane. At each temperature, the sample was rotated 360° around the vertical axis in steps of 3°, with data collected for 3 minutes at each angle. The data were merged together and symmetrized using Mantid [41]. The diffuse magnetic scattering above T_N was isolated by subtracting the diffraction data collected around 300 K from the higher-temperature data sets, with the KAREN algorithm [42] as implemented in Mantid used to fill in sharp negative holes in the data resulting from the subtraction of the magnetic Bragg peaks. The 3D-ΔmPDF patterns were generated via three-dimensional Fourier transformation of the scattering data in Mantid using the DeltaPDF3D module [43].

X-ray PDF data were collected at beamline 28-ID-1 at Brookheaven National Laboratory, National Synchrotron Light Source-II. The experimental setup is similar to neutron scattering at NOMAD except the detector uses is an amorphous silicon area detector placed at 20 cm away from the sample. The X-ray wavelength is typically about 0.19 Å. The X-ray PDF data for both pure and Na-doped MnTe were collected at various temperature grid from 5 K to 500 K with temperature step of 5 K. The X-ray data were reduced using xPDF suite software [44].

2.8 PDF data reduction and data analysis

Data reduction is the process during which we convert the raw scattering data from the experiment into PDF data that we can use for analysis and modeling. I will discuss the data reduction process done in the neutron time of flight experiments, such as at NOMAD. Data reduction at NOMAD is done by using a software called Addie [45]. The software is capable to perform normalization of the scattered data using the neutron scattering length of elements present in the sample, background subtraction using the measured background from the empty sample container, and additional corrections for inelasticity. Then the Fourier transform is done on the reduced scattering data after

choosing an appropriate value for the maximum Q value to include in the transform, which is typically between 25 and 35 Å^{-1}. The Fourier transformed corrected data is then our experimental PDF data.

Once we get the experimental PDF data, we can use a python based software called PDFgui [46] to extract the information from PDF data. We can load our PDF data and structural model into PDFgui which then can refine the lattice parameters and other structural parameters using a least-squares minimization to refine the model, where the calculated PDF matches closely as possible with the PDF data. Once the data is refined using the PDFgui software we get refined structure, lattice parameters, atomic positions, atomic displacement parameters, etc. We also use the python package diffpy.srfit to perform more flexible and automated fitting on PDF data.

2.9 Magnetic scattering and magnetic form factor

Neutrons are chargeless particles with spin-1/2. Each neutron carries a magnetic moment and behaves like a tiny bar magnet which makes it possible to study and analyze the magnetic structure of materials. The interaction of the neutron's spin with the unpaired electron of the material gives rise to magnetism in the material. so, we can use the neutron scattering technique to determine the spin configuration as well as the magnetic structure of any material. The scattered intensity of the magnetic material is composed of various intensities arising from spin-spin (I_M), spin-nucleus (I_{S-N}), and nucleus-nucleus (I_{N-N}) interference functions, i.e.

$$I_{total} = I_M + I_{S-N} + I_N. \tag{2.27}$$

The magnetic scattering intensity in terms of magnetic structure function ($S_M(Q)$) is,

$$I_M(Q) = f_M^2(Q) S_M(Q) \tag{2.28}$$

Here, $f_M(Q)$ represents the magnetic form factor, which is the Fourier transform of the spin

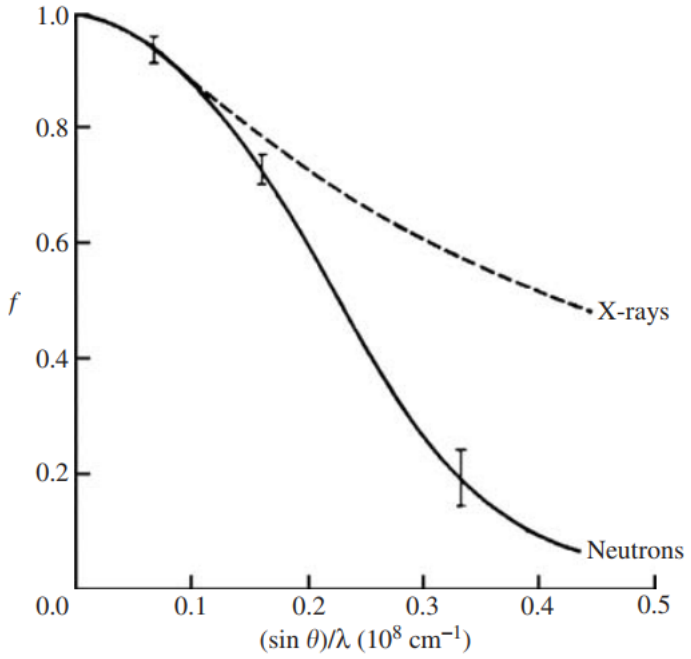

Figure 2.4 Comparison of neutron and X-ray form factor of Mn^{2+} (Bacon 1975).

density distribution function of an atom [32]. The magnetic form factor of Mn falls quickly in comparison to the X-ray form factor, as shown in Figure 2.3.

The magnetic differential scattering cross-section is given by [Lovesey, 1984b],

$$\frac{d\sigma}{d\Omega} = \left| \sum_i \gamma_n r_0 f_{mi}(\mathbf{Q}) exp(i\mathbf{Q}\cdot\mathbf{r}_i)\mathbf{S}_i \right|^2 \tag{2.29}$$

$$\frac{d\sigma}{d\Omega} = (\gamma_n r_0)^2 \sum_{i,j} f_{mi}(\mathbf{Q}) f_{mj}(\mathbf{Q}) exp(i\mathbf{Q}\cdot(r_i - r_j)) S_{\perp i}.S_{\perp j} \tag{2.30}$$

Here γ_n is the neutron gyromagnetic ratio, r_0 is the classical electron radius, $S_\perp$ represents the component of the magnetic moment perpendicular to the scattering vector $\mathbf{Q}$, and the $f_{mi}(\mathbf{Q})$ is the magnetic form factor of the i^{th} spin.

2.10 Magnetic Pair distribution function (mPDF)

On averaging equation 2.30 for a powder sample of a system having identical localized spins within the quasistatic approximation, we get,

$$\frac{d\sigma}{d\Omega} = \frac{2}{3}NS(S+1)(\gamma r_0)^2 f_m^2 + (\gamma r_0)^2 f_m^2 \sum_{i \neq j} [A_{ij} \frac{\sin \kappa r_{ij}}{\kappa r_{ij}} + B_{ij}(\frac{\sin \kappa r ij}{(\kappa r_{ij})^3} - \frac{cos \kappa r_{ij}}{(\kappa r_{ij})^2})] \tag{2.31}$$

Here, i and j represent the individual magnetic moments S_i and S_j separated by a distance r_{ij}, $A_{ij} = < S_i^y S_j^y >$, $B_{ij} = 2 < S_i^x S_j^x - < S_i^y S_j^y >$, N is the number of spins in the system, S is the spin quantum number, γ= 1.913 μ_N is the neutron magnetic moment, $r_0 = \frac{\mu_0 e^2}{4\pi m_e}$, f_m is the magnetic form factor, and κ is the magnitude of the scattering vector. The first term of the above equation represents the scattering from a collection of randomly oriented spins and is the result of self-scattering ($i = j$). A_{ij} and B_{ij} are locally defined for each spin pair using unit vectors,

$$\hat{\mathbf{x}} = \frac{\mathbf{r_j} - \mathbf{r_i}}{|\, \mathbf{r_j} - \mathbf{r_i} \,|} \tag{2.32}$$

and

$$\hat{\mathbf{y}} = \frac{\mathbf{S_i} - \hat{\mathbf{x}}(\mathbf{S_i}.\hat{\mathbf{x}})}{|\, \mathbf{S_i} - \hat{\mathbf{x}}(\mathbf{S_i}.\hat{\mathbf{x}}) \,|}. \tag{2.33}$$

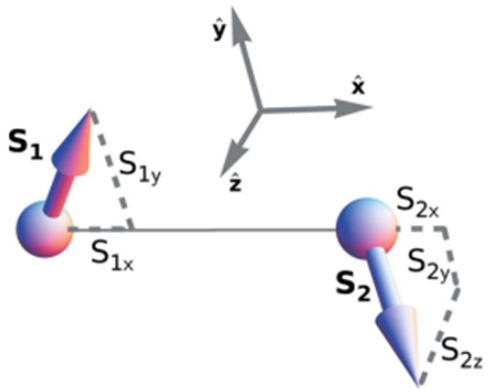

Figure 2.5 Resolution of spin vectors (Figure adapted from [6])

On dividing equation 2.31 by self-scattering factor ($\frac{2}{3}NS(S+1)(\gamma r_0)^2 f_m^2$) we get magnetic structure $S(\kappa)$:

$$S(\kappa) = \frac{\frac{d\sigma}{d\Omega}}{\frac{2}{3}NS(S+1)(\gamma r_0)^2 f_m^2} \tag{2.34}$$

$$S(\kappa) = 1 + \frac{3}{2NS(S+1)} \sum_{i \neq j} [A_{ij} \frac{\sin \kappa r_{ij}}{\kappa r_{ij}} + B_{ij} (\frac{\sin \kappa rij}{(\kappa r_{ij})^3} - \frac{\cos \kappa r_{ij}}{(\kappa r_{ij})^2})] \tag{2.35}$$

We define the reduced magnetic structure function as $F(\kappa) = \kappa[S(\kappa) - 1]$ and the above equation reduces to:

$$F(\kappa) = \frac{3}{2NS(S+1)} \sum_{i \neq j} [A_{ij} \frac{\sin \kappa r_{ij}}{r_{ij}} + B_{ij} (\frac{\sin \kappa r_{ij}}{\kappa^2 r_{ij}^3} - \frac{\cos \kappa r_{ij}}{\kappa r_{ij}^2})] \tag{2.36}$$

The reason to introduce the reduced magnetic structure function is to remove the contribution from self-scattering, and the Sine Fourier transform of the reduced magnetic structure function gives us the magnetic PDF in real space:

$$f_m(r) = \frac{2}{\pi} \int_0^\infty F(\kappa) \sin \kappa r \, d\kappa \tag{2.37}$$

$$f_m = \frac{2}{\pi} \frac{3}{2NS(S+1)} \sum_{i \neq j} \frac{1}{r_{ij}} (A_{ij} \int_0^\infty \sin \kappa r \sin \kappa r_{ij} \, d\kappa + \frac{B_{ij}}{r_{ij}^2} \int_0^\infty \frac{\sin \kappa r \sin \kappa r_{ij} \, d\kappa}{\kappa^2} - \frac{B_{ij}}{r_{ij}} \int_0^\infty \frac{\sin \kappa r \cos \kappa r_{ij} \, d\kappa}{\kappa}) \tag{2.38}$$

$$f_m = \frac{2}{\pi} \frac{3}{2NS(S+1)} \sum_{i \neq j} \frac{1}{r_{ij}} [A_{ij} \frac{\pi}{2} \delta(r - r_{ij})] + \frac{B_{ij}}{r_{ij}^2} \frac{\pi}{4} (r + r_{ij} - |r - r_{ij}|) - \frac{B_{ij}}{r_{ij}} \frac{\pi}{4} 2\Theta(r - r_{ij})] \tag{2.39}$$

$$f_m = \frac{1}{N} \frac{3}{2s(S+1)} \sum_{i \neq j} \frac{1}{r_{ij}} [A_{ij} \delta(r - r_{ij}) + \frac{1}{2} \frac{B_{ij}}{r_{ij}^2} (r + r_{ij} - |r - r_{ij}|) - \frac{B_{ij}}{r_{ij}} \Theta(r - r_{ij})] \tag{2.40}$$

For a single pair of spins,

$$(f_m)_{ij}(r < r_{ij}) = \frac{3}{2NS(S+1)} B_{ij} \frac{r}{r_{ij}^3}, \tag{2.41}$$

$$(f_m)_{ij}(r = r_{ij}) = \frac{3}{2NS(S+1)} B_{ij} [\frac{A_{ij}}{r} \delta(r - r_{ij}) + \frac{B_{ij}}{2r^2}] \tag{2.42}$$

and

$$(f_m)_{ij}(r > r_{ij}) = 0 \tag{2.43}$$

Thus the mPDF function can be written concisely as:

$$f_m(r) = \frac{1}{N}\frac{3}{2S(S+1)}\sum_{i\neq j}\left(\frac{A_{ij}}{r}\delta(r-r_{ij}) + B_{ij}\frac{r}{r_{ij}^3}\Theta(r_{ij}-r)\right) \tag{2.44}$$

where $\Theta(x)$ represents the Heaviside step function [6]. Equation 2.44 is the basic mPDF quantity of our interest. The mPDF function involves the delta function at spin-pair separation distances and is modulated by the orientational term A_{ij}, which is positive for ferromagnetic alignment along the y-direction and negative for antiferromagnetic alignments. mPDF also contains a term that is linear in r (which is absent in the PDF) which arises due to the fact that magnetic neutron scattering entirely depends on spatial as well as orientational correlations of magnetic moments [6].

2.11 Normalized and non-normalized magnetic PDF

To obtain normalized magnetic PDF, we have to follow three different steps: first, we need to isolate magnetic scattering intensity, which can be done by separating nuclear and magnetic contribution in momentum space. The second step is to normalize the separated magnetic signal by dividing it by the square of the magnetic form factor (f_m^2), and at last, we perform Fourier transform of the normalized pattern which gives us the normalized real-space magnetic PDF. However, non-normalized magnetic PDF refers to the magnetic pattern in real space which is not divided by the magnetic form factor. For instance, we can performed combined atomic and magnetic fits by transforming the total neutron scattering pattern in real space and separating the magnetic pattern. According to standard structural PDF protocols, the total PDF obtained from the total neutron scattering intensity is given by,

$$G_{total}(r) = F\{Q(\frac{I_{total}}{N\langle b\rangle^2} - \frac{\langle b^2\rangle}{\langle b\rangle^2})\} \tag{2.45}$$

Here, $F\{....\}$ represents the Fourier transform, total intensity (I_{total}) is composed of nuclear intensity (I_n) and magnetic intensity (I_m), N is the number of atoms, b is the nuclear scattering length, and the angled bracket represents an average of all nuclei present in the sample.

$$G_{total}(r) = F\{Q(\frac{I_n + I_m}{N\langle b\rangle^2} - \frac{\langle b^2\rangle}{\langle b\rangle^2})\} \tag{2.46}$$

$$G_{total}(r) = F\{Q(\frac{I_n}{N\langle b\rangle^2} - \frac{\langle b^2\rangle}{\langle b\rangle^2})\} + F\{Q(\frac{I_m}{N\langle b\rangle^2})\} \tag{2.47}$$

$$G_{total}(r) = G_n(r) + \frac{d(r)}{N\langle b\rangle^2} \tag{2.48}$$

Where, $G_n(r)$ is the atomic PDF and $d(r) = F\{QI_m(Q)\}$ is called unnormalized mPDF, as it does not involve division by the square of magnetic form factor. Using the convolution theorem, we can write,

$$d(r) = c_1 f(r) * S(r) + c_2 \frac{dS}{dr} \tag{2.49}$$

Here, c_1 and c_2 are constants and $c_1/c_2 = -\frac{1}{\sqrt{2\pi}}$ in full ordered state, $*$ represents the convolution operator, $S(r) = F\{f_m(Q)\} * F\{f_m(Q)\}$. And, $F\{f_m(Q)\}$ is equivalent to real space spin density and $d(r)$ is equivalent to proper magnetic PDF.

The result of a typical neutron PDF experiment on a magnetic material without neutron polarization analysis contains the atomic PDF as well as the unnormalized mPDF. And the magnetic pattern thus obtained after separating is a non-normalized magnetic PDF.

2.12 mPDF pattern of a single pair of spins

I will illustrate some of the examples of one-dimensional mPDF. If we just consider a pair of ferromagnetically aligned spin where both are pointed vertically upward in the same direction. We

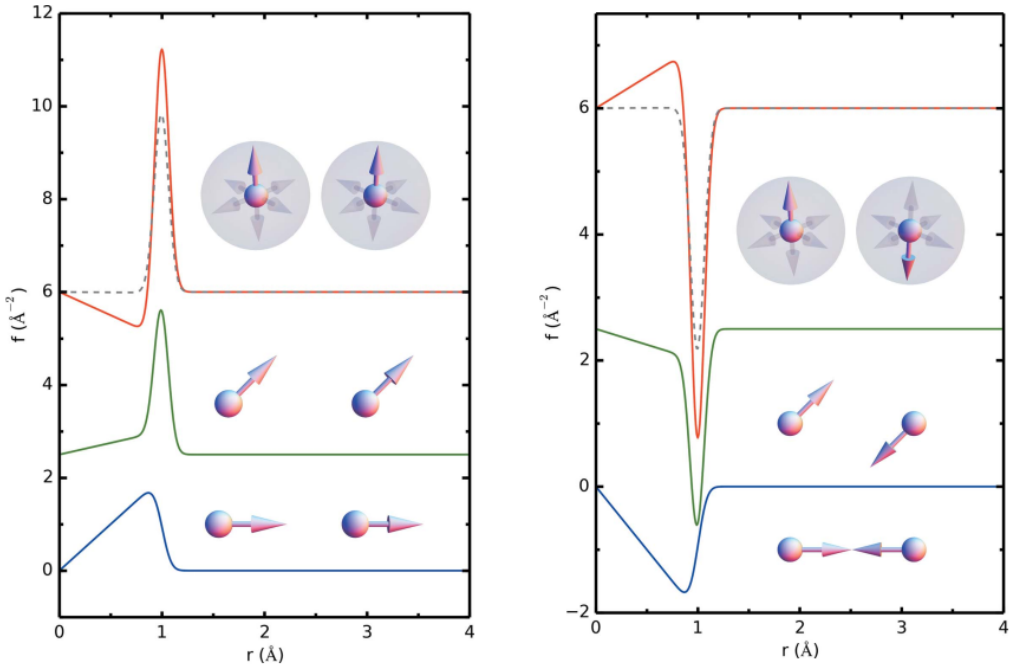

Figure 2.6 Simulated mPDFs of a pair of ferromagnetically (left) and antiferromagnetically (right) aligned spins in different spin orientations. (Figure adapted from [6])

get a positive peak in our mpdf pattern at spin separation distance along with the linear baseline. So, the positive peak in our mPDF pattern indicates that the spins are ferromagnetically aligned. The slope of the linear baseline and the height of the positive peak depend on the orientation of the spins, as shown in Fig. 2.6 (left). This was a simple example with a pair spin. But if we average the bunch of ferromagnetic pairs of spin in all possible orientations, the baseline vanishes and the peak height to 2/3 of the maximal value as shown by a dotted line. This is something we expect for uncorrelated ferromagnetic dimers. The mPDF pattern of a pair of AF spin looks similar to pair of FM spins but it has a negative peak at AF spin pair distance.

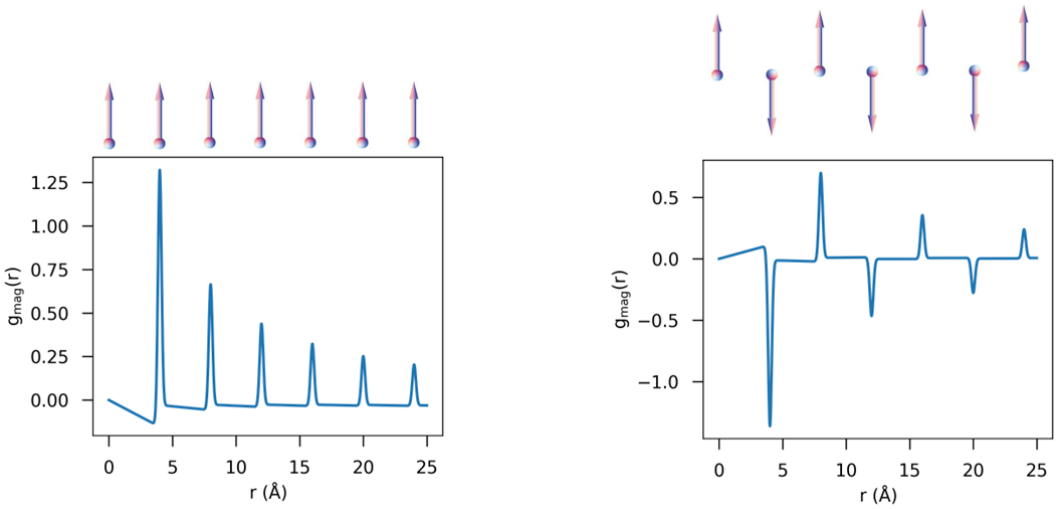

Figure 2.7 Simulated mPDFs of a 1D chain of ferromagnetically aligned spins (left), and antiferromagnetically coupled spins (Right). (Figure adapted from [6])

2.13 1D magnetic pair distribution (mPDF) pattern

Let's us consider a 1d array of spins all pointing vertically upward direction. we can see an array of positive peaks at spin separation distance in our mPDF pattern, this is because the first nearest spins, second nearest spins, third nearest spins, and so on, all make a ferromagnetic alignment pointing in the same direction, as a result, we only see positive peaks at spin separation distance in our mPDF pattern. When averaged over all possible spin directions, the peak height diminishes as $1/r$ and the baseline slope diminishes as $1/r^3$. However, the 1d arrays of AF spins give alternating negative and positive peaks at spin pair separation distance in our mPDF pattern. The first nearest spin is AF magnetically aligned which is a negative peak at the first nearest spin distance. Similarly, the second nearest spin makes FM alignment which gives a positive peak in our mPDF pattern and so on.

2.14 Extracting magnetic signal from neutron total scattering pattern

There are two different ways to separate the magnetic signals from the total scattering neutron pattern. The first one involves the conventional neutron diffraction measurement where the magnetic scattering pattern is separated from the nuclear scattering in momentum space. This can be done simply by performing a fit to the nuclear Bragg peaks and subtracting the residual, or by subtracting a high-temperature scattering pattern to isolate the temperature-dependent magnetic scattering that appears at a lower temperature. The magnetic scattering pattern thus obtained after subtraction can then be normalized by dividing the square of the magnetic form factor. This normalized magnetic pattern obtained in momentum space is then converted to mPDF by performing the Fourier sine transform. This method to separate the magnetic signal can be quite challenging in practice because even a very small error while subtracting can be significantly amplified while normalizing by magnetic form factor. In this case, the normalization step can be skipped, and a cleaner Fourier transform can be obtained, although the real-space resolution is greatly reduced compared to the properly normalized pattern. The second option is to separate nuclear and magnetic signals in real space. This involves the time of flight total neutron experiment to collect the atomic and magnetic PDF pattern at PDF optimized beamline. Thus, obtained patterns are then reduced using standard PDF protocols. The result contains the atomic as well as unnormalized mPDF. To conduct a quantitative mPDF refinement, first, we need to perform an atomic PDF refinement and then use the residual of atomic fit as input data for the mPDF refinement. Even better, we can model atomic and magnetic PDFs together to perform a simultaneous refinement against total PDF signals [47].

2.15 3D - ΔmPDF

The 3D - ΔmPDF measures the magnetic diffuse scattering of a single crystal and gives local spin-spin correlation which can be directly visualized in real space. The three-dimensional Fourier transform of diffuse neutron scattering cross-section of a single crystal gives us 3D - ΔmPDF,

$$3\mathrm{D}-\Delta\mathrm{mPDF}(\mathrm{r}) = F^{-1}\left[\frac{d\sigma_{\mathrm{diffuse}}}{d\Omega}\right] \tag{2.50}$$

$$3\mathrm{D}-\Delta\mathrm{mPDF}(\mathrm{r}) = \frac{r_0^2}{4\mu_B^2}\langle\delta\mathbf{M}\bar{\otimes}\delta\mathbf{M}) - \frac{1}{\pi^4}(\delta\mathbf{M}\bar{*}\Upsilon)\otimes(\delta\mathbf{M}\bar{*}\Upsilon)\rangle, \tag{2.51}$$

Here $\delta\mathbf{M}$ is a vector field representing the local deviation from the average magnetic structure, r represents the distance between two spins in real space. Similarly,r_0 and μ_B represent classical electron radius and the Bohr magneton respectively, and Υ represent the vector interaction of neutron spin with electronic magnetic moments of material, and $\Upsilon(\mathbf{r}) = \frac{\mathbf{r}}{|\mathbf{r}|^4}, if\ |\mathbf{r}| \neq 0$ and $\Upsilon(r) = 0, |r| = 0$. The first term in equation 2.51 will give the positive peak for the parallel moments i.e., an angle less than $\pi/2$, and a negative peak for the antiparallel moments (angle larger than $\pi/2$). But the first term will be zero for the perpendicular moments. The second term of the equation 2.51 gives the peak shape which elongated to the direction of moments. The second term is always weaker than the first term unless moments are perpendicular. So the positive peak in 3D - ΔmPDF is due to the spins aligning in the same direction and the negative peak is observed if the two spins align in opposite directions [48, 49].

2.16 Software for mPDF analysis

Magnetic pair distribution function (mPDF) technique was first introduced by [6] which can be used to investigate magnetic correlation, i.e, long-range and short-range magnetic correlation directly in real space. Using mPDF technique we can calculate normalized as well as unnormalized mPDF for any arbitrary magnetic structure. A python-based program called diffpy.mpdf is used

to study the magnetic structure in real space [49]. It is an open-source python program and can be easily available at https://github.com/FrandsenGroup/diffpy.mpdf. Using diffpy.mpdf we can build magnetic structures of any arbitrary complexity using a propagation vector or a magnetic unit cell. It can include multiple magnetic species in one structure and can do a 3D visualization of our magnetic structure.

Chapter 3

Synthesis and basic characterization

This chapter describes the details of the polycrystalline sample preparation of pure MnTe and 2% Na-doped MnTe (i.e., $Na_{0.02}Mn_{0.98}Te$), phase characterization of these materials using laboratory X-ray diffraction, and basic magnetic characterization. For completeness, this chapter also includes the procedure to grow the single crystal of MnTe, although this growth was carried out by our collaborators at Oak Ridge National Laboratory.

3.1 Polycrystalline and single crystal synthesis of MnTe

Polycrystalline samples of MnTe and $Mn_{0.98}Na_{0.02}Te$ were prepared by mixing Mn powder (99.95%), Te pieces (99.999%), and Na pieces (99.99%) in an argon glove box. These reactants were handled inside the glove box at all times, as they are sensitive to air. Exposing them to the air will degrade their quality through oxidation. The reactants were mixed together in the molar ratios given by the composition and were then loaded inside a quartz ampoule having a length of 20 cm and an internal diameter of 20 mm. The ampoule loaded with the reactants was then sealed with a valve top, removed from the glove box, and quickly transferred to a vacuum sealing station. We evacuated the argon gas which was initially contained inside the tube until the pressure

Figure 3.1 Photograph of the vacuum sealing system used for the synthesis.

inside the ampoule dropped to 10^{-5} torr. The ampoule was then flame-sealed using a H_2 + O_2 torch. We used a wet paper towel on the lower end of the tube (where the reactants were contained) to avoid unnecessary heating of the reactants during the sealing process. A picture of the vacuum system used for the synthesis is shown in Fig . 3.1. Once the sealing was completed, we trimmed the length of the ampoule with a diamond-tipped rotating saw blade to allow it to fit easily inside the box furnace. These ampoules containing the reactants were then heated inside the furnace at a temperature of 950 °C for 6 hours. We then opened the furnace at that temperature (wearing flame- and heat-protective equipment), removed the ampoules quickly with tongs, and quenched them into a large bucket containing ice water. This quenching process must be completed quickly to avoid damaging the heating coil of the furnace and maximizing the purity of the sample. One difficulty that we experienced during this process was the shattering of the ampoules while quenching in cold water. We found that shorter ampoules with a smaller total sample mass ($\sim$1 g) decreased the probability of the ampoule cracking during the quenching process. After a successful quenching of the ampoules, they were heated for another 3 days at 650 °C. Once the heating was completed, we cut open the ampules using a glass cutter and quickly transferred the samples into the glove box with less than a minute of exposure time. The samples were then ground into a fine powder inside the glove box. The powder was black in color after synthesis. These samples were stored inside the glove box until they were needed for experiments. This prevented any kind of contamination or reaction with air.

Our collaborators from Oak Ridge National Laboratory prepared a single crystal of pure MnTe. The crystal was grown from Te flux by heating a mixture of Mn:Te = 36:64 at 890°C for 12 days.

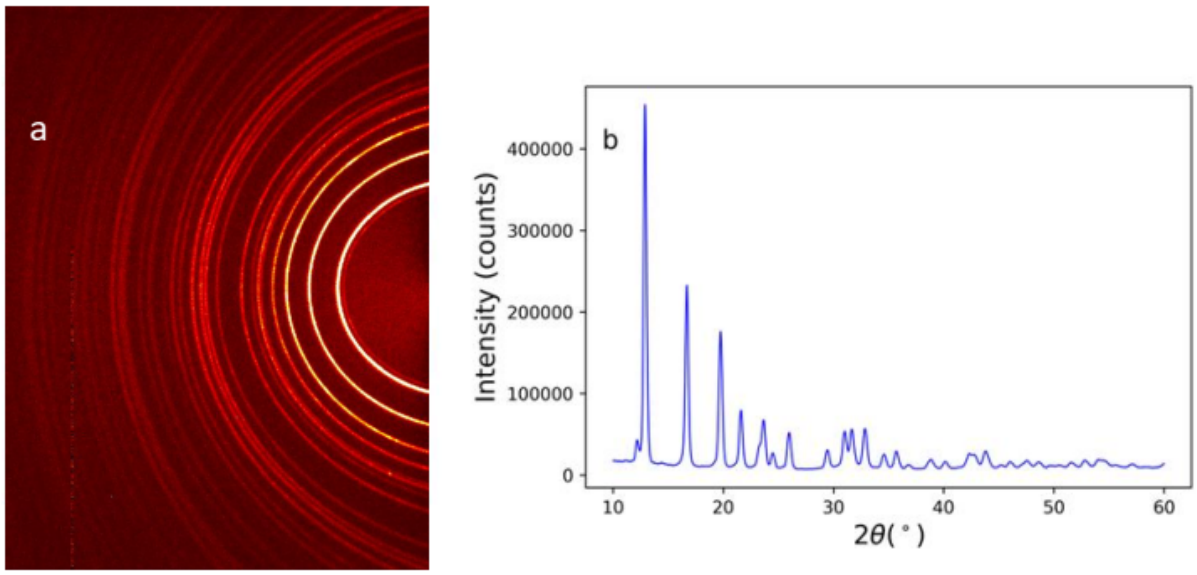

Figure 3.2 (a) Debye rings of MnTe obtained from laboratory X-ray diffraction. (b) X-ray diffraction pattern as a function of 2θ after integrating the Debye rings.

3.2 Basic structural and magnetic characterization

The purity of the prepared samples was checked using laboratory X-ray diffraction. Both polycrystalline samples, MnTe, and $Mn_{0.98}Na_{0.02}Te$, were loaded into polyimide capillaries of diameter 0.026 inches inside the glovebox. The capillaries were plugged at both ends using modeling clay. The samples were mounted on the Bruker-FR591 X-ray diffractometer located in the lab of Dr. Stacey Smith at Brigham Young University. After centering the capillaries with the goniometer, we collected data at room temperature with a Mo target (wavelength 0.71 Å) for 20 minutes for each sample. The powder diffraction pattern in the form of Debye rings is shown in Fig. 3.2 (a). We selected the scattering angle range of 2θ from 10° to 58° and integrated the powder patterns azimuthally to obtain one-dimensional patterns as shown in Fig. 3.2 (b).

Rietveld analysis of the powder X-ray diffraction (PXRD) patterns was done using GSAS-II software [50] using the published crystal structure of MnTe. This allowed us to verify the high purity of these samples. The Rietveld refinement is shown in Fig. 3.3 (b). The red open circles

represent the observed X-ray diffraction pattern and the black solid line is the Rietveld fit obtained using space group P63/mmc. The vertical blue ticks mark the Bragg peak positions. The overall fit residual is almost flat (represented by a green curve), indicating an excellent with $R_w = 0.048$. No impurity peaks are observable in the pattern. The X-ray diffraction pattern of $Mn_{0.98}Na_{0.02}Te$ is not shown here, but it looks nearly indistinguishable from pure MnTe, also with no observable impurity peaks.

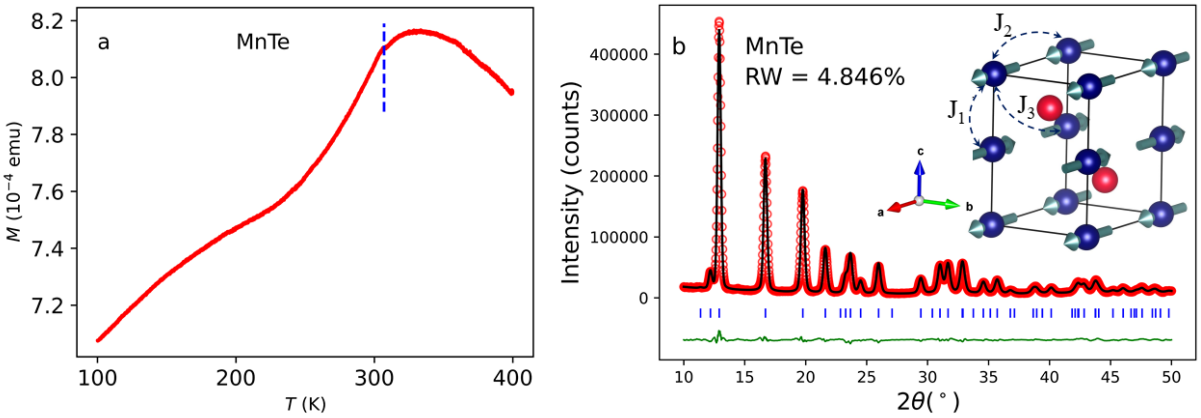

Figure 3.3 (a) Field-cooled measurement of MnTe performed under a field of $H = 1000$ Oe, where the magnetization is plotted as a function of temperature while warming up. The dashed vertical line marks $T_N = 307$ K. (b) The Rietveld refinement pattern (black curve) plotted on the top of X-ray diffraction (red symbols) of MnTe. The green curve shows the fit residual and the blue vertical ticks are the Bragg positions. Inset: Crystal and magnetic structure of MnTe. Blue and red spheres represent Mn and Te atoms, respectively. The dashed lines labeled J_1, J_2, and J_3 represent the magnetic exchange interactions between the first three nearest neighbors. (Figure adapted from [7])

Magnetization measurements of MnTe were carried out using a vibrating-sample magnetometer (VSM) instrument from Quantum Design. The measurements were done in the laboratory of Dr. Karine Chesnel at Brigham Young University. The powder sample of MnTe was loaded into three small capillary tubes inside the glovebox. The tubes were sealed at both ends using modeling clay. The three capillary tubes were then attached to the VSM sample holder and loaded into the VSM instrument. The magnetization was measured between 100 K and 400 K in both field cooling (FC)

and zero field cooling (ZFC) conditions. The FC measurements were carried out under various cooling field magnitudes of 100 Oe, 500 Oe, and 1000 Oe respectively. In Fig. 3.3(a), we display the FC measurement of MnTe performed under a field of $H = 1000$ Oe, showing the magnetization $M(T)$ as a function of temperature while warming up. The visible kink in the curve just above 300 K confirms the expected magnetic phase transition. These magnetization and X-ray diffraction results confirm the phase purity and expected magnetic behavior of the samples.

Chapter 4

Magnetic pair distribution function analysis of MnTe

Note: This chapter forms the basis of a paper that has been published (Matter, volume 5, Issue 6, P1853-1864), and as such, it reflects a collaborative effort from all coauthors. Those coauthors include Jacob Christensen, Parker Hamilton, Feng Ye, Karine Chesnel, Taylor D. Sparks, Rosa Ward, Jiaqiang Yan, Michael A. McGuire, Michael E. Manley, Julie B. Staunton,Raphaël P. Hermann, and Benjamin A. Frandsen.

4.1 Overview

Short-range magnetic correlations can significantly increase the thermopower of magnetic semiconductors, representing a noteworthy development in the decades-long effort to develop high-performance thermoelectric materials. Here, we reveal the nature of the thermopower-enhancing magnetic correlations in the antiferromagnetic semiconductor MnTe. Using magnetic pair distribution function analysis of neutron scattering data, we obtain a detailed, real-space view of robust, nanometer-scale, antiferromagnetic correlations that persist into the paramagnetic phase

above the Néel temperature T_N = 307 K. The magnetic correlation length in the paramagnetic state is significantly longer along the crystallographic *c* axis than within the *ab* plane, pointing to anisotropic magnetic interactions. *Ab initio* calculations of the spin-spin correlations using density functional theory in the disordered local moment approach reproduce this result with quantitative accuracy. These findings constitute the first real-space picture of short-range spin correlations in a magnetically enhanced thermoelectric and inform future efforts to optimize thermoelectric performance by magnetic means.

4.2 Introduction

Despite the tremendous promise of thermoelectric devices for environmentally friendly energy applications ranging from waste heat recovery to solid state refrigeration [10–12], relatively few material systems have been identified that possess excellent thermoelectric properties and are also economically and environmentally viable for widespread use. The material parameters that determine thermoelectric performance are encapsulated by the dimensionless figure of merit zT. Material design principles such as the "electron crystal, phonon glass" concept have led to improvements in zT in many materials, but additional routes toward superior thermoelectric performance may be required to unlock the full potential of thermoelectric devices. Recently, the paramagnon drag effect was discovered, in which local thermal fluctuations of the magnetization known as paramagnons drag charge carriers and impart to them a magnetic contribution to thermopower. This is significant because it opens a new avenue for optimizing thermoelectric properties in magnetic semiconductors. Analogous to magnon drag, paramagnons can also drag the charge carriers through the material even in a paramagnetic state if the paramagnons have a sufficiently long correlation length and lifetime. Enhancing the thermopower through paramagnon drag was first demonstrated in the high-performance thermoelectric candidate MnTe [3], an antiferromagnetic (AF) semiconductor

with the hexagonal NiAs structure type.

The discovery of paramagnon drag in MnTe demonstrated the viability of exploiting the spin degree of freedom to boost thermoelectric performance in novel ways [29]. However, significant work remains to be done to benchmark the paramagnon drag effect and establish a comprehensive understanding of its role in MnTe and other materials. Specifically, a real-space picture of the short-range AF correlations is lacking, as is a theoretical framework based on first principles that can explain the observed short-range magnetism and identify other candidate systems with promising paramagnon properties. Addressing these knowledge gaps will greatly enhance future efforts to harness paramagnon effects for thermoelectricity and other functionalities.

Here, we combine cutting-edge neutron total scattering techniques with sophisticated *ab initio* calculations to achieve a comprehensive picture of the short-range AF correlations underlying the paramagnon drag effect in MnTe. Using both three-dimensional (3D) and one-dimensional (1D) magnetic pair distribution function (PDF) [6, 32–34] analysis of neutron total scattering data, we present the first real-space visualization of nanometer-scale spin correlations in the paramagnetic state of MnTe and reveal a strongly anisotropic magnetic correlation length. These observations are quantitatively reproduced using density functional theory (DFT) with the self-interaction-corrected (SIC) local spin density approximation in the disordered local moment (DLM) approach (DLM-DFT-SIC) [51,52]. These results deepen our understanding of paramagnon phenomena in MnTe and related materials and highlight the value of combining magnetic PDF (mPDF) and DLM-DFT-SIC theory to establish the nature of short-range magnetic correlations in exquisite detail. The success of this approach for MnTe provides a valuable benchmark for future applications to other materials with magnetically enhanced functionalities.

4.3 Neutron total scattering structure function

The neutron total scattering structure function $S(Q)$ is shown for MnTe and Na-MnTe at various temperatures in Fig. 4.1. The $S(Q)$ plots of pure MnTe in panel (a) show prominent magnetic Bragg peaks below T_N=307 K, e.g. around 0.9 $Å^{-1}$ and 1.9 $Å^{-1}$. As the temperature increases above T_N, these sharp peaks become broad and diffuse features due to short-range magnetic correlations. Fig. 4.1(b) shows equivalent $S(Q)$ plots for $Mn_{0.98}Na_{0.02}Te$. The most notable difference is the absence of the strong magnetic peak around 0.9 $Å^{-1}$ at low temperature, which can be attributed to the reorientation of the spins from an in-plane direction in pure MnTe to along the c -axis in the doped compound. Only the components of the magnetization that are perpendicular to **Q** can contribute to the intensity, so the spins pointing along the $c-$ axis are parallel to the (001) Bragg peak and therefore do not contribute intensity. However, as the temperature is raised, some magnetic intensity is observed around 0.9 $Å^{-1}$, indicating that the spin direction gains some component perpendicular to c, as also observed for Li doping [53]. Above T_N, similar diffuse scattering as in pure MnTe is observed.

4.4 1D atomic and magnetic PDF fits

4.4.1 Fitting approach

To gain further information about the local atomic and magnetic structure of MnTe, we turn to PDF analysis. As mentioned previously, the PDF is obtained as the Fourier transform of the normalized neutron total scattering intensity, which includes both Bragg scattering from the long-range, average structure and diffuse scattering from short-range correlations. The result is a real-space map of the pairwise correlations between scatters in the material. Because neutrons interact both with nuclei and electronic magnetic moments, the total scattering intensity includes contributions from

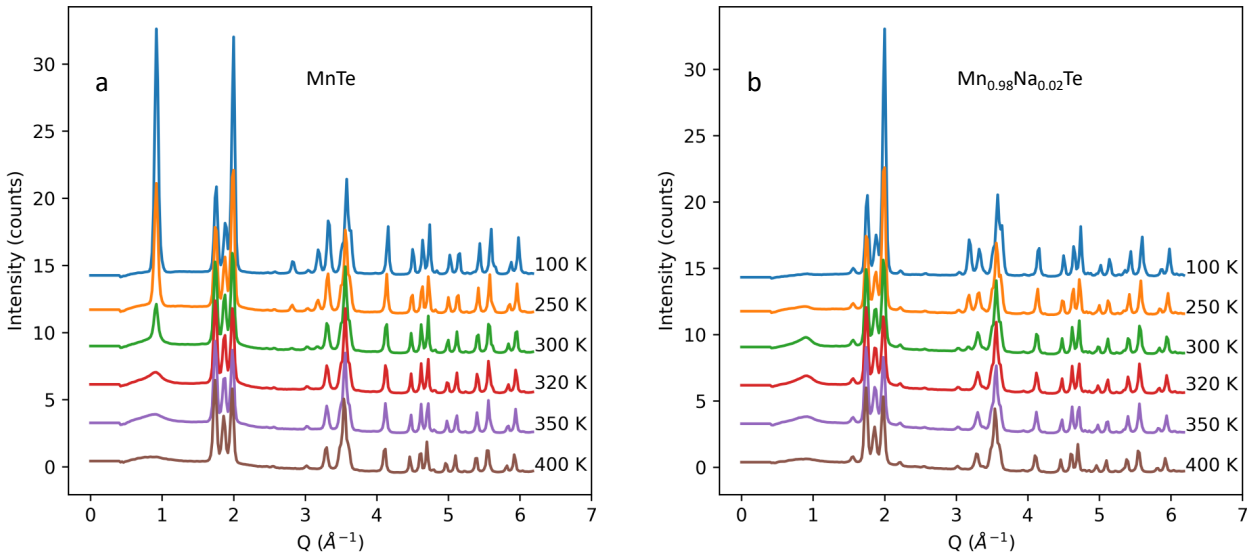

Figure 4.1 Total scattering structure function for MnTe and $Mn_{0.98}Na_{0.02}Te$. (a) $S(Q)$ curves for various temperatures for MnTe (b) Corresponding data for $Mn_{0.98}Na_{0.02}Te$.

both atomic and magnetic correlations, so the experimental PDF is the sum of the atomic PDF and the magnetic PDF components. The magnetic scattering is suppressed in reciprocal space due to the magnetic form factor, which greatly reduces the magnetic scattering intensity for Mn^{2+} spins beyond 5 - 6 $Å^{-1}$. The ideal mPDF signal would be obtained by dividing the magnetic intensity by the square of the magnetic form factor before computing the Fourier transform, but because the nuclear scattering is also present and is not subject to any such form factor suppression, that approach is impractical for a combined atomic and magnetic PDF experiment without neutron polarization analysis. Consequently, the experimental mPDF signal has much lower real-space resolution than the atomic PDF signal, as is evident in Fig. 4.4 of the section 4.5. Fortunately, this does not pose an insurmountable challenge to effective mPDF analysis, because there are fewer magnetic atoms than total atoms in the material, so a high-resolution mPDF signal is typically unnecessary for reliable modeling of the data. The broadening effect due to the magnetic form factor is explicitly included in the calculations in the diffpy.mpdf package by performing a convolution of

the ideal mPDF signal with the Fourier transform of the magnetic form factor convoluted with itself. This allows us to model the form factor effect accurately. These details are discussed extensively in Supp. Ref. [33].

One-dimensional atomic and magnetic fits to the neutron PDF data were done using the following iterative fitting approach. We first performed an atomic PDF fit, using the published structure as a starting point for the refinement. The calculated atomic PDF corresponding to this fit was then subtracted from the total PDF data, yielding a fit residual that was dominated by the experimental magnetic PDF signal but also contained any imperfections in the atomic PDF fit. This fit residual served as the input data for an initial mPDF refinement. A second atomic PDF fit was then conducted, but this time the input data was the total PDF data minus the best-fit calculated mPDF. The parameter values from the first atomic PDF fit were used as starting points for this next iteration. The reason for this second fit was to allow a more precise refinement of the structure against data from which the magnetic component had been largely removed. We then subtracted the best-fit atomic PDF from the original total PDF data and used the result as input data for a second mPDF fit. The calculated mPDF was then subtracted from the original data to perform a third atomic PDF fit, and finally, a third mPDF fit was conducted in the same fashion. We found that the goodness-of-fit metric R_w improved with each successive iteration, but additional fits beyond these three iterations resulted in no meaningful improvement. We also attempted a true corefinement of the atomic and magnetic structures together, but we found that the fits tended to terminate in local minima in this case leading to (very slightly) lower fit quality, whereas the iterative approach with alternating atomic and magnetic PDF fits was more robust.

The atomic PDF fit parameters included the lattice parameters a and c, the hexagonal symmetry-allowed anisotropic displacement parameters (ADPs), the z coordinates of the Te and Mn atomic sites (also allowed to vary within the symmetry of the space group), the linear correlated motion correction parameter, and an overall scale factor. The instrumental parameters Q_{damp} and Q_{broad}

were fixed to values determined from calibration fits to a silicon standard.

The magnetic model assumed the published antiferromagnetic structure but included as free parameters the paramagnetic scale factor (corresponding to the self-scattering component of the magnetic differential scattering cross section [33]), the ordered scale factor (related to the square of the locally ordered magnetic moment), and the direction of the magnetic moments as defined by the angle θ from the c axis. We note that the paramagnetic scale factor is based on the isotropic magnetic form factor for Mn^{2+} tabulated in Supplementary Ref. [54]. Since the self-scattering contribution is restricted largely to $r < 1$ Å [33], which was excluded from our fits, this parameter has only a minor effect on the fit but was nevertheless included for completeness. For the case of fits corresponding to short-range magnetic correlations (as opposed to long-range magnetic order), we additionally included two parameters quantifying the exponential correlation length along the c axis and in the ab plane called ξ_c and ξ_{ab}, respectively. For a given pair of magnetic moments with a separation vector $\mathbf{r}_{\text{sep}} = r_{\text{sep}}\hat{n}$, where r_{sep} is the distance separating them and $\hat{n}$ is the direction of the separation vector, the correlation length was calculated as

$$\xi(\hat{n}) = \left(\frac{n_x^2 + n_y^2}{\xi_{ab}^2} + \frac{n_z^2}{\xi_c^2} \right)^{-\frac{1}{2}}, \tag{4.1}$$

where n_x, n_y, n_z are the components of $\hat{n}$ in Cartesian coordinates. Thus, the correlation length corresponds to the surface of an ellipsoid in real space with semi-axes of ξ_{ab} along the Cartesian axes x and y and ξ_c along the Cartesian z direction. Relative to whichever moment was arbitrarily taken to be at the origin, then, the second magnetic moment in the pair has a magnitude of $m_0 \exp[-r_{\text{sep}}/\xi(\hat{n})]$, where m_0 is the magnitude of the moment at the origin.

We note that the default calibration at NOMAD has limited accuracy for $Q \leq 2.4$ Å^{-1}. The $(0,0,1)$ magnetic Bragg peak is located at $Q = 2\pi/c \approx 0.93$ Å^{-1}, meaning its apparent Q position in the data is affected by the suboptimal calibration. This introduces artifacts into the $S(Q)$ and $G(r)$ patterns. To correct for this, we recalibrated the $S(Q)$ data in the range $0.5 \leq Q \leq 2.4$ Å^{-1} using the known position of the magnetic Bragg peak at low temperature, which improved the quality of

the data and allowed more quantitatively accurate fits.

4.5 Fitting results

4.5.1 Fitting results at 100 K

We further performed one-dimensional atomic and magnetic PDF analysis of neutron total scattering data collected from powder samples of MnTe and Na-doped MnTe on a dense temperature grid across T_N. Figure 4.2(a) shows the atomic and magnetic PDF fits together at 100 K for pure MnTe.

The upper set of curves represent the total PDF data (blue symbols) and total calculated PDF (red curve), which includes the best-fit atomic and magnetic PDF signals together. We used the published atomic and magnetic structures [21] as the starting point for the refinement (see figure 3.3 (b) for full refinements). The fit is excellent ($R_w = 0.0576$), as seen by the small and featureless fit residual shown as the green curve at the bottom of the panel. The best fit occurs when the spins are aligned within the *ab* plane. Due to the hexagonal symmetry, no preferred direction within the *ab* plane could be detected, although Kriegner *et al.* [24] have established that the moments lie along nearest-neighbor Mn-Mn directions in the plane. Fig. 4.2(b) shows the same results for the Na-doped sample. We note that the best-fit spin orientation for the Na-doped sample is along the *c* axis, which accounts for the different shape of the mPDF signal compared to the pure sample and is confirmed by inspection of the magnetic Bragg peak intensities in the diffraction data, as shown in the figure 4.1. The different spin orientations for pure and doped MnTe at 100 K are illustrated in the insets of Fig. 4.2 (b). These findings agree with neutron diffraction data on Li-doped MnTe [53] and point to a delicate balance between competing ground states in MnTe.

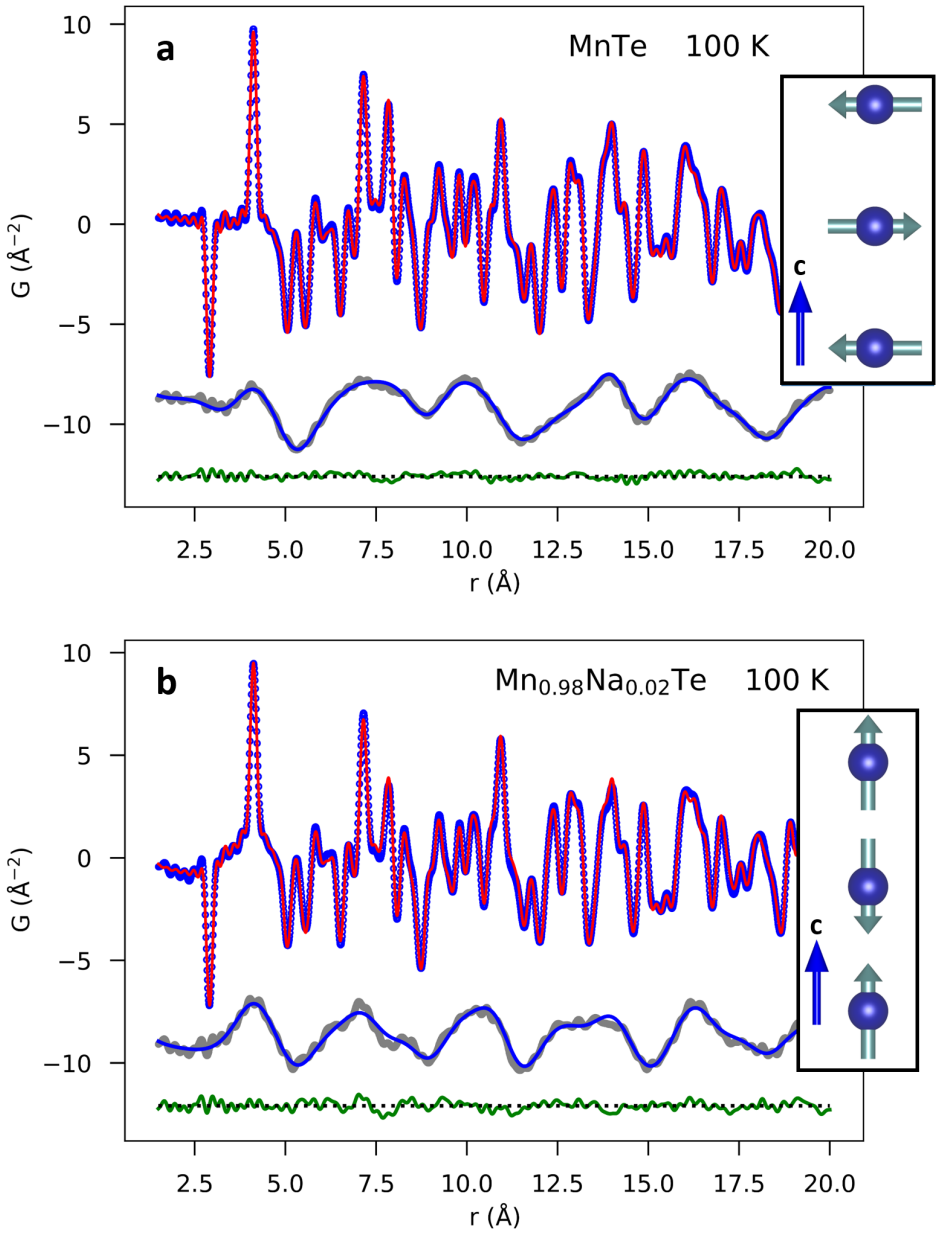

Figure 4.2 Combined atomic and magnetic PDF analysis for pure MnTe (a) and Na-doped MnTe (b) at 100 K, showing a strong magnetic signal and a reorientation of the sublattice magnetization from in the plane in pure MnTe to out of the plane in doped MnTe. The mPDF data (gray curve; assumed to be the difference between the observed total PDF and the calculated atomic PDF) and the calculated mPDF (solid blue curve) are offset vertically below the total PDF data and fit for clarity. Insets: Corresponding Mn spin orientations along the *c* axis.

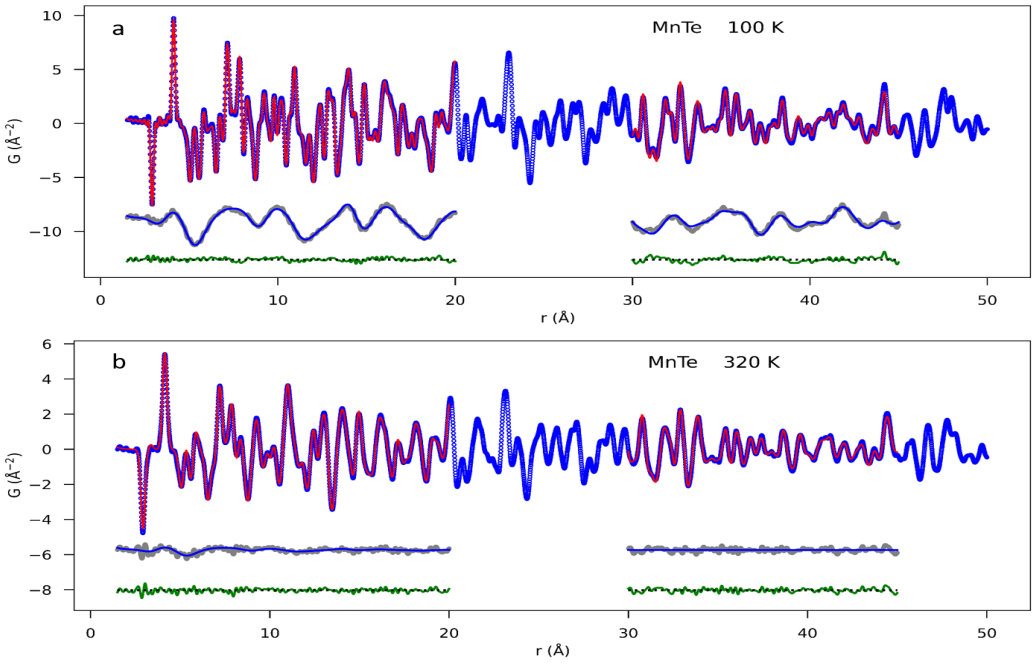

Figure 4.3 Combined atomic and magnetic PDF fits at 100 K (a) and 320 K (b) for the two different fitting ranges (1.5 – 20 Å and 30 – 45 Å).

4.5.2 Fitting results: high$-r$ fits and low$-r$ fits

In Fig. 4.3, we display the combined atomic and magnetic PDF fits at 100 K and 320 K for the two fitting ranges: low- r fits (1.5 – 20 Å), and high$-r$ fits (30 – 45 Å). The shorter fitting range captures the short-range magnetic correlations present above T_N, whereas the longer fitting range is representative of the genuine long-range magnetic order.

A single fit over the entire data range is possible, in principle. However, PDF patterns from NOMAD are known to have certain r-dependent distortions which significantly affect fits conducted over data ranges longer than 20 Å. For this reason, we avoid such long-range fits and instead focus on sections of the PDF data that allow us to probe the correlations of interest, e.g. the local correlations for the short-range fit and the global correlations for the long-range fit. We have also done fits for intermediate ranges such as 20 - 30 Å (not shown here), and the fit quality is equivalent to the other fitting ranges shown, but we focus here instead on fitting ranges that give us access

exclusively to the local correlations (1.5 – 20 Å) and the long-range correlations (30 – 45 Å).

We performed similar fits for the data sets collected in the paramagnetic state. In Fig. 4.4(a), we display the atomic and magnetic PDF fits for MnTe at 320 K, using the fitting range (1.5 – 20 Å). As seen in the lower set of curves, the mPDF component is reduced in magnitude and spatial extent compared to 100 K; nevertheless, it exhibits clear AF features in the low-r region. These short-range AF correlations can be modeled adequately by including an isotropic exponential envelope of the form $\exp(-r/\xi)$ in the calculated mPDF, where the correlation length ξ is a parameter in the fit. Qualitatively similar short-range features in the mPDF data are observed up to 500 K, the highest measured temperature. The locally ordered magnetic moment extracted from fits conducted over the ranges 1.5 – 20 Å and 30 – 45 Å are shown in figure 4.4(b) as the blue triangles and orange circles, respectively. The latter fitting range reveals an abrupt onset of long-range AF correlations at 307 K that can be well described as a continuous phase transition with a critical exponent of $\beta = 0.30 \pm 0.03$. In contrast, the short-range fits indicate that a significant fraction of the bare magnetic moment remains correlated among near neighbors up to at least 500 K. The thermal evolution of the locally ordered moment is reminiscent of a continuous phase transition biased by an applied field [55], suggesting that the local field created by neighboring spins plays the role of an applied field. Above T_N, the locally ordered moment can be well described by exponential decay that asymptotically approaches a constant value of 1.1 μ_B with a characteristic temperature scale of 90 K, as shown by the solid curve. Additional details about the mPDF fits are given in section 4.4.

We performed an additional set of mPDF fits above T_N over the range 1.5 - 20 Å in which we implemented a model with distinct correlation lengths along c (ξ_c) and in the ab plane (ξ_{ab}). At all temperatures above T_N, the best-fit values of ξ_c were longer than ξ_{ab} by approximately 50% [see Fig. 4.4(c)]. As seen in Fig. 4.4, both correlation lengths show a rapid decrease with temperature from T_N to about 350 K, but remain fairly constant at higher temperatures, similar to the local magnetic moment in Fig. 4.4(b). We note that the magnetic correlation lengths above

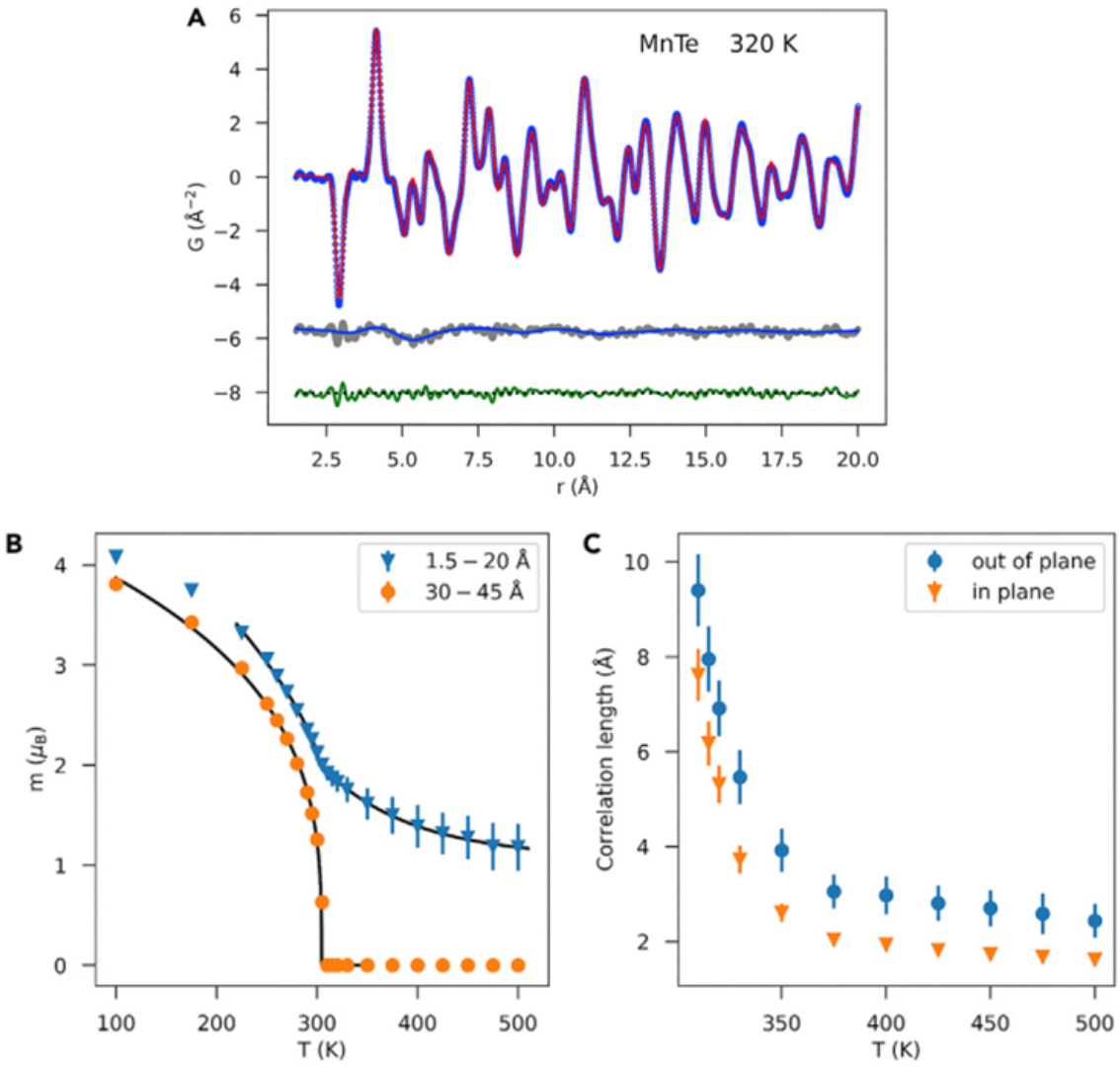

Figure 4.4 (a) Combined atomic and magnetic PDF fit for MnTe at 320 K, with the short-range AF correlations evidenced in the mPDF data (gray curve). (b) The ordered magnetic moment of MnTe as a function of temperature as determined from mPDF fits over a short fitting range (1.5-20 Å), blue triangles, representing the ordered moment for nearest-neighbor spin pairs) and a longer fitting range (30-45 Å), orange circles, representing the true long-range ordered moment). The solid curves are power-law fits described in the main text. Representative fits over the longer fitting range are shown in Fig. 4.3. (c) Temperature dependence of the best-fit correlation length along *c* (blue circles) and within the *ab* plane (orange triangles) in the paramagnetic regime, obtained from fits over 1.5 - 20 Å.

350 K determined from the 1D mPDF fits are on the order of a few Angstroms, which is smaller than the value obtained by Zheng et al [3] (2.5 nm). This disparity is partially ameliorated by multiplying the mPDF result by π to account for the different definitions of the magnetic correlation length used in the two works (see for example the Supplemental Material of Z. Dun *et al*, *Phys. Rev. B* **103**, 064424 (2021)). The remaining discrepancy is attributed to the fact that the 1D mPDF data effectively integrates overall neutron energy transfers, yielding the instantaneous spin-spin correlation function, while the previous work selected a narrow energy band around the elastic channel for calculating the correlation length, yielding the time-averaged correlation length.

4.6 Spin direction determined from mPDF fits

To determine the best-fit spin direction from the mPDF data at each temperature, we performed a series of mPDF fits where the angle θ between the spin and the c axis was set to values ranging from 0° to 90° in 5° steps. The azimuthal angle within the ab plane makes no difference for the orientationally averaged 1D mPDF due to the hexagonal symmetry, so it was fixed to zero (corresponding to the [100] direction) for simplicity. The goodness-of-fit metric R_w was then extracted from each fit, and the angle corresponding to the lowest value of R_w (hence the best overall fit) was designated as the best-fit angle. These are shown as the gray circles in Fig. 4.5. The shaded bars underneath the gray circles indicate the range of spin angles that result in R_w values within 0.5% of the optimal R_w value, where 0.5% was chosen as a reasonable threshold for meaningful differences between fits. The hue of the colored bar lightens proportionally with the increase in R_w from the optimal value, fading to white at the 0.5% threshold. Thus, these shaded bars represent a type of confidence interval for the best-fit spin direction as determined by the mPDF fits. Below about 250 K, the pure and doped compounds show a strong preference for an in-plane orientation ($\theta = 90^\circ$) and out-of-plane orientation ($\theta = 0^\circ$), respectively, with narrow confidence intervals. As

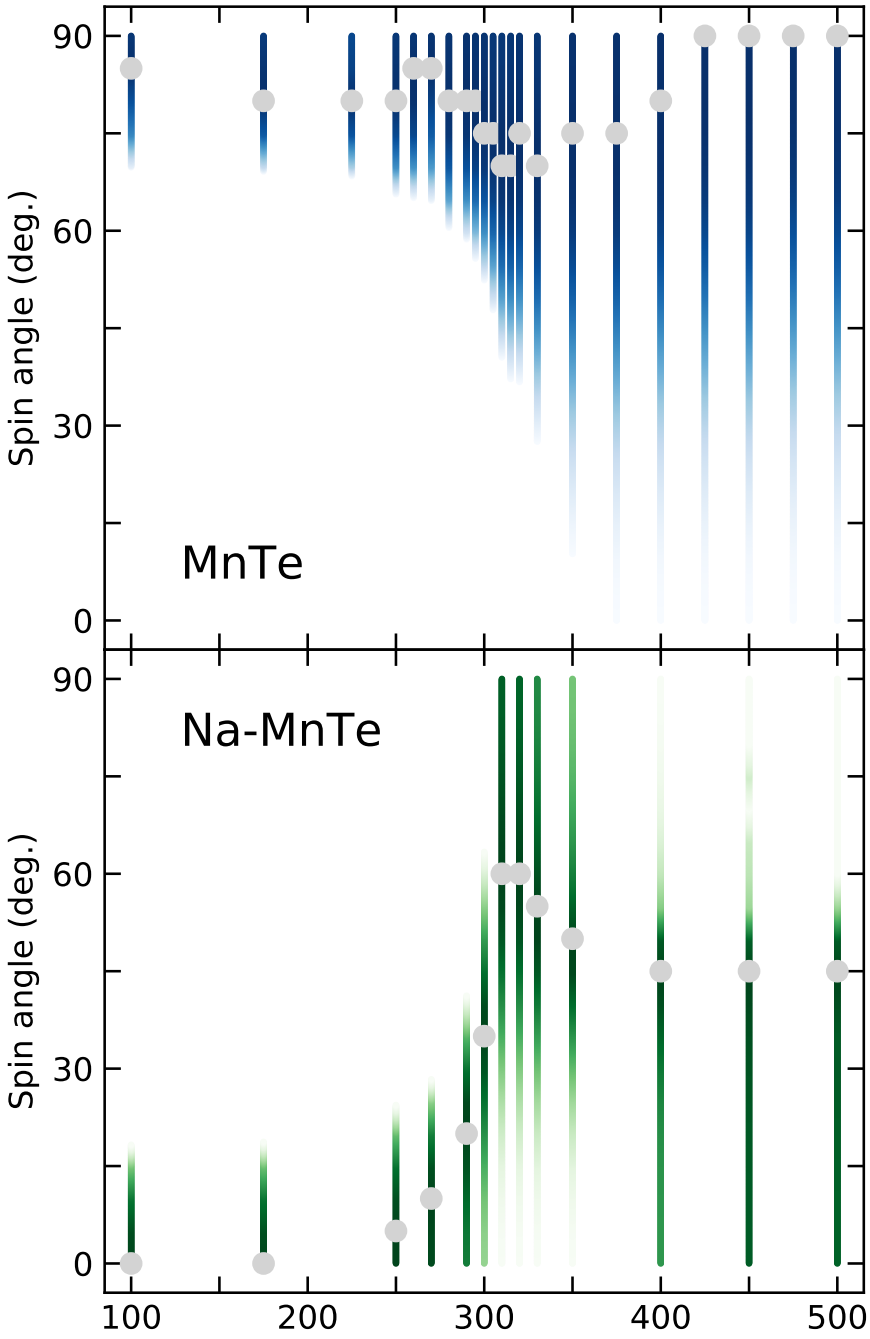

Figure 4.5 Best-fit spin directions for MnTe (top) and Na-doped MnTe (bottom). The vertical axis on the figure indicates the angle between the *c* axis of the unit cell and the direction of the ordered magnetic moment. The gray circles indicate the angle yielding the best fit for each temperature. The shaded bars represent a type of confidence interval as explained in the main body of the text.

the temperature increases further, the confidence intervals for both compounds widen due to the reduced weight of the magnetic component in the total PDF. Additionally, the best-fit spin angle for the doped compound cants away from the *c* axis and assumes an angle of 60° at T_N, i.e. 30° above the *ab* plane. Above T_N, the 0.5% R_w threshold covers the entire angular range, although there is still a slight improvement to the fit for spin angles closer to the *ab* plane for the pure compound and closer to the *c* axis for the doped compound. In any case, the strong directional preference of the ordered spins that is present deep in the ground state is largely absent from the high-temperature mPDF data presented here.

4.7 DLM-SIC-DFT calculations

4.7.1 Theoretical details

We also compared the experimental mPDF results to the predictions from *ab initio*. The calculations of the spin correlations were carried out using the disordered local moment - density functional theory (DLM-DFT) of finite-temperature magnetism [51,56] in which strong electronic correlations, evident in transition metal oxides [52], lanthanide metals [57,58] and rare earth- transition metal permanent magnets [59,60], for example, are treated with the self-interaction correction [61]. The DLM-DFT incorporates the effects of thermally induced magnetic excitations and can thus describe quantitatively both rare earth (RE) and transition metal (TM) magnetism at finite temperatures. From its *ab initio* Gibbs free energy of a magnetic material [62] complex magnetic interactions can be extracted for use in further modeling. The interactions can turn out to have both components linking pairs of sites, which indicates the most stable magnetic phases including non-collinear, frustrated or long period states, and components multi-site in nature depending on the state and extent of magnetic order. No prior assumption of any specific effective spin Hamiltonian is made, and quantitatively accurate magnetic phase diagrams and also caloric effects can be obtained from

this approach e.g. [56, 58, 62].

When applied to MnTe, the theory accounts for the insulating gap and its persistence into the paramagnetic phase, the magnetic ordering temperature T_N, and the onset of the AF state below T_N. Our first-principles DLM-DFT calculations find the ground-state Mn-ion configuration to be Mn^{2+} with five localized d states constituting a half-filled shell in line with Hund's first rule. For the comparison with the experimental PDF data of this paper, the key quantity from the theory is the lattice Fourier transform (LFT), $\mathscr{S}^{(2)}_{a,b}(\mathbf{q})$, of the direct correlation function for the local Mn moments in the paramagnetic state. The magnetic correlation function in real space, $C_{0,n} = \langle \mathbf{s}_0 \cdot \mathbf{s}_n \rangle$, is determined from this fundamental quantity. The subscripts a,b denote the sites within the unit cell; for MnTe, these are the two sites in the hexagonal NiAs unit cell occupied by Mn atoms. Here, $\mathbf{s}_0$ represents a classical Heisenberg spin-like local moment arbitrarily chosen to be at the origin, $\mathbf{s}_n$ represents a spin in the nth coordination shell, and the angled brackets denote an average over all the spins in that shell. For MnTe, calculations of $\mathscr{S}^{(2)}_{a,b}(\mathbf{q})$ were performed for a grid of 56 wavevectors, $\mathbf{q}$, in the irreducible segment of the Brillouin zone. We found the $C_{0,n}$'s using an Onsager cavity field calculation [63] by solving the coupled integral equations, $C^{-1}_{a,b}(\mathbf{q}) = [\delta_{a,b} - \beta(\mathscr{S}^{(2)}_{a,b}(\mathbf{q}) - \Lambda_a \delta_{a,b})]$ and $\Lambda_a = \int \sum_b \mathscr{S}^{(2)}_{a,b}(\mathbf{q}) C_{b,a}(\mathbf{q}) d\mathbf{q}$ for the LFT of the magnetic correlation function, $C_{a,b}(\mathbf{q})$. This pair of equations ensure that the sum rule $\langle s_a^2 \rangle = 1$ is met. Furthermore, the real-space direct correlation quantities describe the magnetic exchange interactions, the J 's, between the Mn spins on different shells.

4.8 Theoretical results and comparison to experimental data

The observed short-range magnetic correlations invite comparison with theoretical predictions. The spin correlation functions for the first nine coordination shells were calculated *ab initio* as a function of temperature in the paramagnetic regime using the DLM-DFT-SIC approach [52]. The dashed

curves in Fig. 4.6(a) show the correlation functions $\langle \mathbf{S}_0 \cdot \mathbf{S}_n \rangle$, where $\mathbf{S}_0$ is an arbitrary spin, $\mathbf{S}_n$ is a spin in the n^{th} coordination shell relative to $\mathbf{S}_0$, and the angled brackets represent an average over all $\mathbf{S}_n$ in the shell. The spins in the calculation have unit length. Negative and positive values correspond to net antiferromagnetic and ferromagnetic correlations, respectively. Corresponding spin correlation functions extracted from the 1D mPDF fits are displayed as diamond symbols in Fig. 4.6(a). The experimental and theoretical results show remarkable agreement above 350 K, demonstrating that the DLM-DFT-SIC approach can be used to predict high-temperature magnetic correlations in MnTe with quantitative accuracy. The agreement is worse at lower temperatures, where critical behavior associated with the phase transition becomes more dominant. The anisotropic nature of the spin correlations, which is captured naturally by the *ab initio* calculations, is illustrated in Fig. 4.6(b). The absolute value of each $\langle \mathbf{S}_0 \cdot \mathbf{S}_n \rangle$ calculated at 350 K is plotted as a function of coordination shell radius. If the spin correlations were to decay isotropically with distance, then the calculated correlation functions would lie along a smooth, monotonic curve that decreases with shell radius. However, the results are non-monotonic with distance, and we instead observe two distinct bands of correlation functions: a band of comparatively stronger correlations (indicated by the shaded oval) comprised of coordination shells where the spin separation vectors lie along the *c* direction or close to it, and a band of weaker correlations with spin pairs located more in the *ab* plane.

4.9 Obtaining and modeling the three-dimensional delta magnetic pair distribution function (3D-ΔmPDF)

To confirm and extend the results of our 1D atomic and magnetic PDF analysis, we also performed 3D-PDF analysis using a single crystal of MnTe. Single crystal neutron diffraction experiments were carried out on the CORELLI instrument to measure the scattered intensity in large volumes

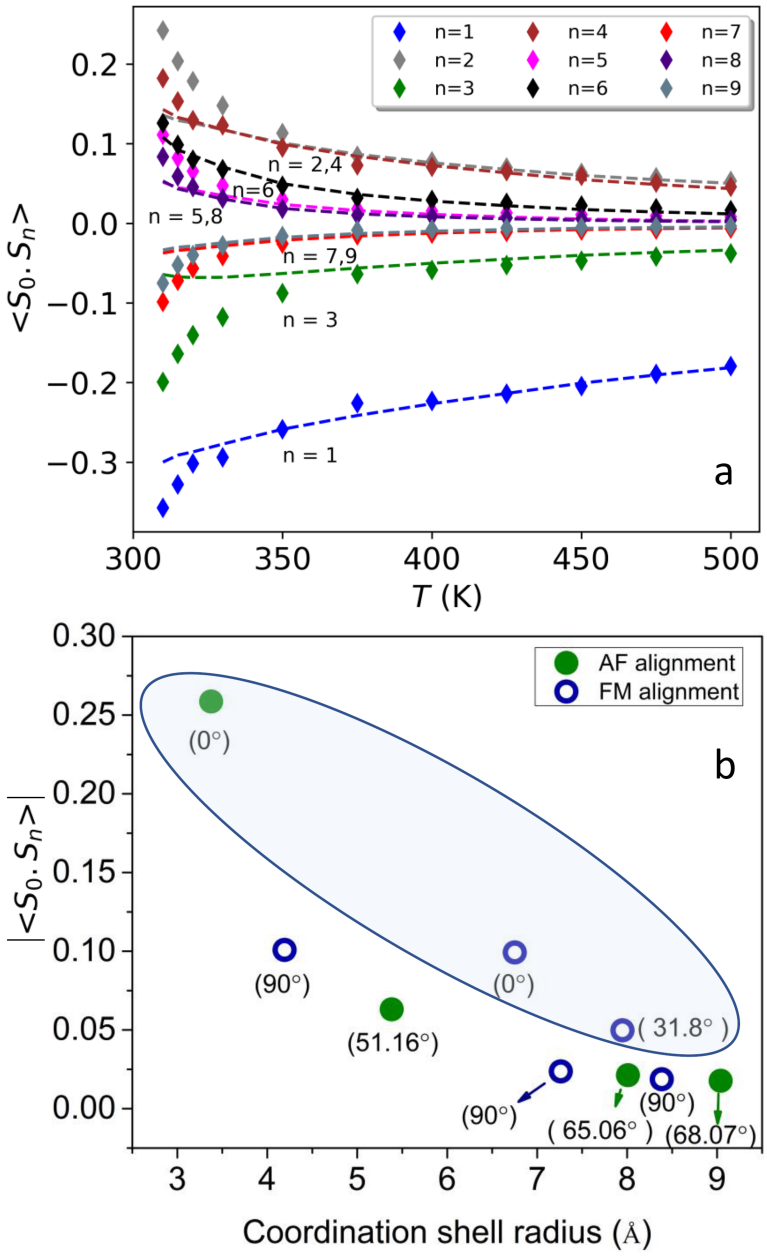

Figure 4.6 (a) Theoretical and experimental spin correlation functions $\langle \mathbf{S}_0 \cdot \mathbf{S}_n \rangle$ versus temperature for the first nine nearest neighbors. The dotted line represents the theoretical and the symbols represent the experimental magnetic correlations. (b) $\langle \mathbf{S}_0 \cdot \mathbf{S}_n \rangle$ versus coordination shell radius for the calculations at 350 K. Filled (open) symbols represent antiferromagnetic (ferromagnetic) alignment. The angle shown for each data point is the angle to the *c* axis formed by each spin pair comprising the respective coordination shells. The shaded oval highlights anomalously strong correlations.

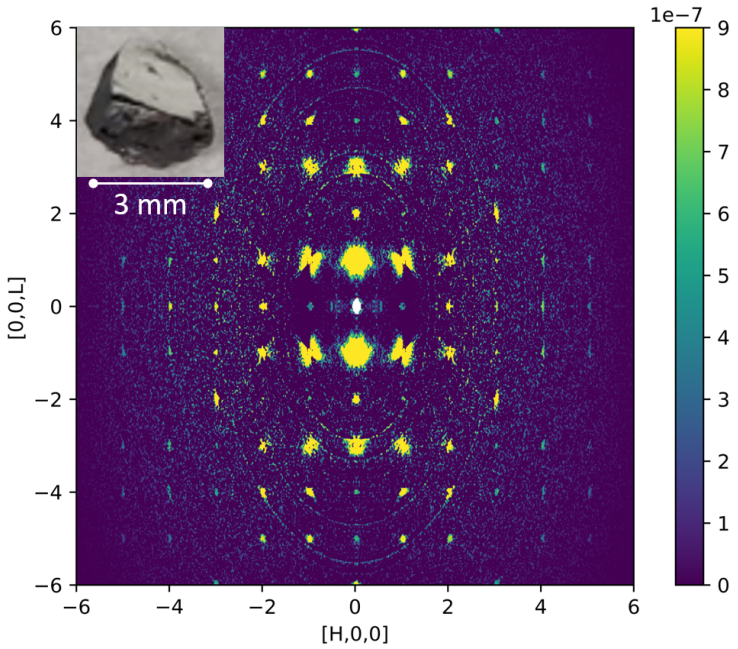

Figure 4.7 Diffuse magnetic scattering in MnTe at 340 K. Inset: Photo of the single crystal used for the experiment.

of reciprocal space. The sample had a mass of 96.4 mg with all three dimensions similar in size ($\sim$3 mm), as seen in the inset of Fig. 4.7. At each temperature, the sample was rotated through 360° in steps of 3°. Due to the wavelength range of the incident neutrons ($\sim 0.64 - 2.86$ Å), this angular step size allows continuous coverage of reciprocal space. The resulting 120 scattering patterns were then merged together, symmetrized according to the point group $6/mmm$, and normalized by the scattering from a vanadium reference sample, all within Mantid [41]. To isolate the diffuse magnetic scattering above T_N, we subtracted the data collected at 300 K (in the ordered state) from the data collected at 340 K. This largely removed the nuclear Bragg peaks and background signal from the instrument and sample can, but it also created sharp negative features at the positions of the magnetic Bragg peaks. To eliminate these features and minimize other artifacts of the temperature subtraction, we utilized the KAREN algorithm [42] as implemented in Mantid, which identifies statistical outliers and replaces them with a smooth interpolating function. This resulted

in the intermediate scattering pattern shown in Fig. 4.7, where we clearly observe diffuse magnetic scattering centered around the original positions of the magnetic Bragg peaks present below T_N.

This intermediate scattering pattern was passed through the DeltaPDF3D module [43] in Mantid, a three-dimensional fast Fourier transform (FFT) algorithm that yields the 3D-ΔmPDF. To reduce noise in the FFT, we restricted the input scattering data to a sphere of reciprocal space with a radius of approximately 9 Å^{-1}. This does not exclude any meaningful magnetic scattering because the magnetic form factor suppresses scattering at high $\mathbf{Q}$.

In Fig. 4.8, we show slices of the 3D-ΔmPDF at 340 K for the $(x,0,z)$ plane (also shown in the main manuscript) and the $(x,y,0)$ plane in panels (a) and (b), respectively. These were taken from the totally integrated diffraction data, i.e., with the correlation chopper switched off. The alternating spin orientation along the z direction is clearly seen as the alternating bright and dark spots in panel (a), while the ferromagnetic alignment within the xy plane is illustrated in panel (b). We note that certain artifacts remain in the data as a result of noise, imperfections in the temperature subtraction, and Fourier ripples from the FFT. These artifacts include the "peanut-shaped" modulation of the signal in the $(x,0,z)$ plane and the weak diagonal lines in the $(x,y,0)$ plane. Fortunately, these do not interfere with the interpretation of the main features of the 3D-ΔmPDF data. We show the corresponding calculated 3D-ΔmPDF patterns in panels (c) and (d), where the model assumed the standard MnTe antiferromagnetic structure but with anisotropic correlation lengths applied, as discussed in the previous section. The correlation lengths were determined from fits to line cuts through the 3D-ΔmPDF data. We performed the calculations using a home-built extension of the diffpy.mpdf python package following the definition of the 3D-ΔmPDF given in Ref. [34].

For comparison, we also display in Fig. 4.9 the 3D-ΔmPDF in the $(x,0,z)$ generated from the diffraction data with the correlation chopper enabled, which selects just the neutrons scattered elastically (with approximately ± 2 meV). As discussed in the main text, the correlation lengths are longer for the elastic 3D-ΔmPDF than they are for the totally integrated 3D-ΔmPDF. This is evident

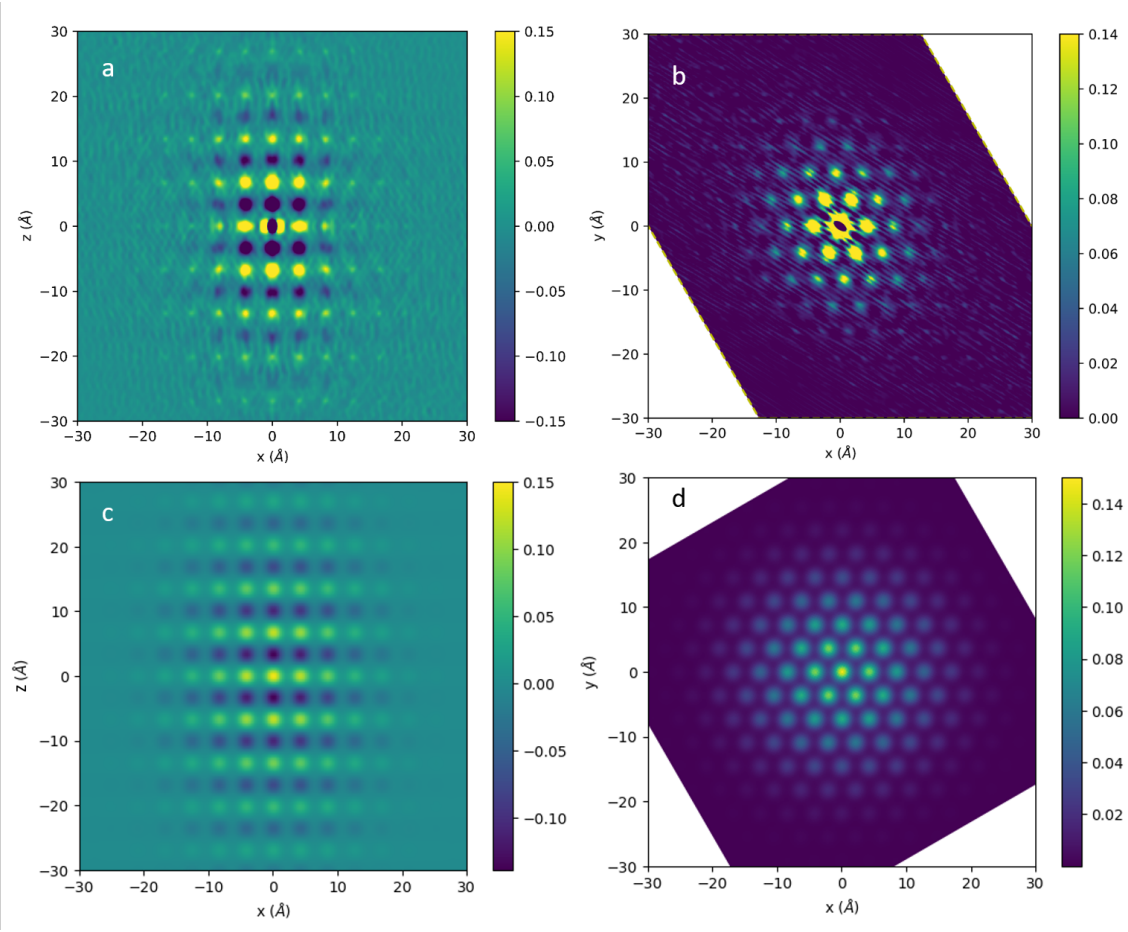

Figure 4.8 (a, b) Experimental 3D-ΔmPDF pattern at 340 K in the $(x,0,z)$ plane (a) and $(x,y,0)$ plane (b). Note that the intensity scale is arbitrary. (c, d) Corresponding calculated 3D-ΔmPDF patterns using the anisotropic correlation lengths determined from fits to line cuts through the 3D-ΔmPDF data.

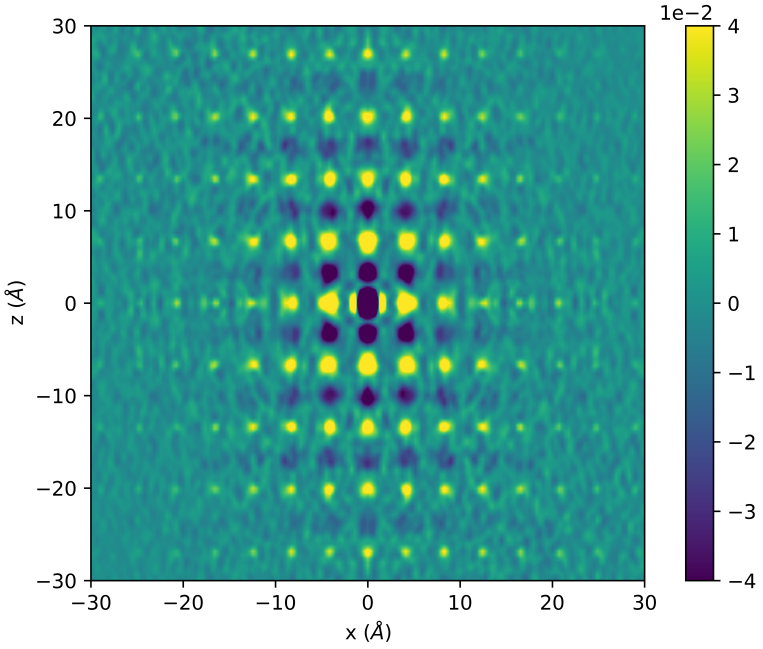

Figure 4.9 Experimental 3D-ΔmPDF pattern at 340 K in the $(x, 0, z)$ plane obtained from the elastic channel of the diffraction pattern.

in Fig. 4.9 from the fact that well-defined bright and dark spots persist out to further distances than in Fig. 4.8(a).

4.10 Three-dimensional delta magnetic pair distribution function (3D-ΔmPDF) results

We begin by examining the single-crystal neutron diffraction and three-dimensional difference mPDF (3D-ΔmPDF [34]) data to gain insight into the short-range AF correlations above T_N. In Fig. 4.10(a), we display the 3D-ΔmPDF at $T \sim 340$ K in the xz plane, such that the a (c) crystallographic direction is parallel to the horizontal (vertical) axis [see Fig. 3.3 for a view of the crystal structure]. This figure provides a direct view of the short-range AF correlations in the paramagnetic state of MnTe in real space. Moving vertically up and down the pattern, we observe

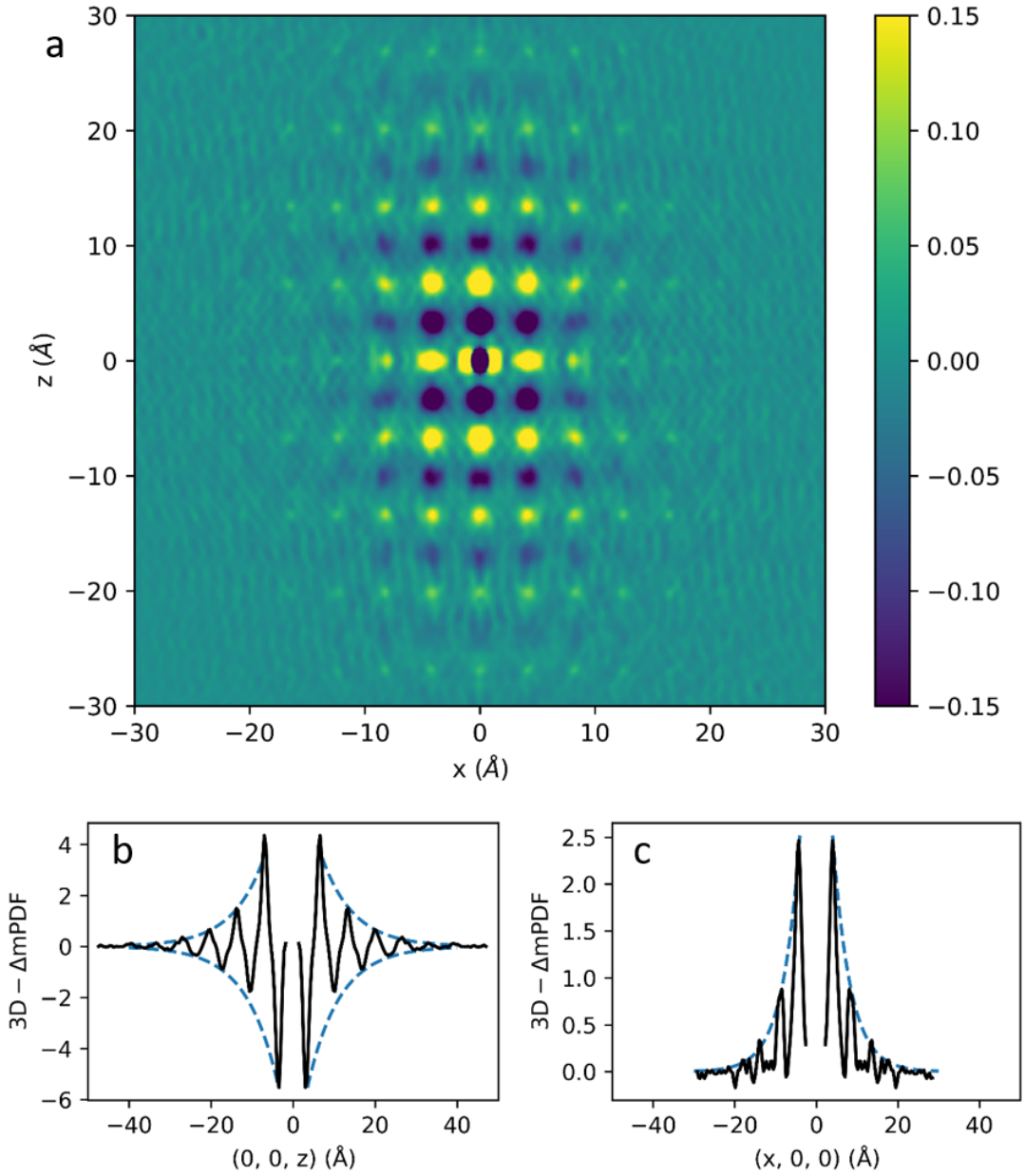

Figure 4.10 (a) 3D-ΔmPDF pattern showing short-range, anisotropic AF correlations in the xz plane of MnTe at $T \sim 340$ K. Positive (negative) values of the 3D-ΔmPDF indicate net ferromagnetic (antiferromagnetic) correlations between spins separated by the corresponding real-space vector. The units shown in the color bar are arbitrary. (b) Cut through the 3D-ΔmPDF data along the z direction with $x = y = 0$. Dashed curves illustrate the best-fit exponential envelope with a correlation length of 7.7(4) Å. (c) Same as (b), but with the cut taken along the x direction. The best-fit correlation length is 4.3(2) Å along this direction.

alternating dark and bright regions indicative of antiferromagnetic correlations along c, while the horizontal direction exhibits rows with uniform color, indicative of ferromagnetic correlations in the ab plane. Thus, the short-range magnetic correlations are qualitatively similar to those in the long-range ordered state.

Interestingly, Fig. 4.10(a) reveals a striking anisotropy in the correlation length, with correlations along z clearly visible to about ± 30 , while those along x have a much shorter spatial extent. This is a more direct visualization of the anisotropy that was revealed from the fits to the 1D-mPDF data. The anisotropic correlation length can be quantified by taking cuts of the displayed data along the $x = 0$ and $z = 0$ lines and fitting an exponential envelope to the correlation profile, as shown in Fig. 4.10(b, c). This procedure yields correlation lengths of 7.7(4) Å and 4.3(2) Å, respectively. We note that this 3D-ΔmPDF pattern was collected without any energy discrimination on the instrument and should therefore be considered a totally integrated PDF pattern [64], which probes the instantaneous magnetic correlations. When just the neutrons scattered within the elastic bandwidth of ~ 2 meV are selected (hence providing sensitivity to the correlations with a lifetime longer than $\sim$2 ps), the out-of-plane and in-plane correlation lengths are 14.8(9) Å and 5.8(3) Å, respectively. Additional details regarding the 3D-ΔmPDF analysis are given in the section 4.9, including simulated 3D-ΔmPDF patterns from models of the short-range magnetic order. Although the diffuse magnetic scattering pattern in reciprocal space contains the same information about the short-range magnetic correlations as does the 3D-ΔmPDF, these results highlight the value of transforming the data into real space, where visual inspection and straightforward analysis immediately reveals the salient details of the magnetic correlations.

4.11 Discussion

The results presented here provide a unique, real-space picture of the short-range magnetic correlations in the correlated paramagnet state of MnTe. The 3D-ΔmPDF and 1D-mPDF analyses reveal nanometer-scale, spatially anisotropic correlations that persist up to at least 500 K. The relative stability of the correlation length and the locally ordered moment above 350 K suggests that these short-range spin correlations remain present to much higher temperatures than measured in the current work, supporting the relevance of the paramagnon drag scenario at elevated temperatures where zT approaches 1 in doped samples.

The newly revealed anisotropy of the correlations, i.e. the fact that $\xi_c > \xi_{ab}$, can be viewed as a natural consequence of the relative strength of the AF out-of-plane exchange interaction J_1 compared to the much weaker ferromagnetic in-plane interaction J_2, both of which have been determined from inelastic neutron scattering data [21] and calculations [65] (see Fig. 3.3 (b) for a schematic showing the exchange interactions). The discrepancy between J_1 and J_2 can be rationalized from a structural viewpoint in the context of superexchange theory [66] by noting that along c, the Mn-Mn distance is $\sim$3.36 Å and the Mn-Te-Mn exchange pathway forms an angle of $\sim$70° (favoring strong antiferromagnetism), while within the *ab* plane, the Mn-Mn distance is $\sim$4.15 Å and the Mn-Te-Mn angle is $\sim$90° (favoring weaker ferromagnetism). Thus, MnTe possesses a magnetic character somewhat similar to that of strongly interacting AF chains. We note that J_3 favors AF alignment between the third-nearest neighbors, which, when combined with the action of J_1, also contributes to the in-plane ferromagnetic correlation. The presence of anisotropic exchange interactions was recently proposed as a favorable ingredient for paramagnon-enhanced thermopower [29], as supported by the present work on MnTe.

The anisotropic magnetic correlation length in the paramagnetic regime also raises the interesting possibility that the thermopower itself could be anisotropic. For paramagnon drag to be effective, the spatial extent of the magnetic correlations must exceed the mobile electrons' de Broglie wavelength

(λ_{dB}) and effective Bohr radius (a^*), and the lifetime of the magnetic correlations must likewise exceed the electron-on-paramagnon scattering time [3]. The ratio of the correlation lifetime to the electron-on-paramagnon scattering time would not be expected to be spatially anisotropic, and considering that this ratio is significantly larger than the ratios of the correlation length to λ_{dB} and a^* [3], the anisotropic magnetic correlation length may not necessarily have a significant effect on the thermopower. This question could be answered by direction-dependent thermopower measurements of a doped single crystal of MnTe, but such a sample does not exist to our knowledge. Theoretical modeling may also shed light on this issue.

The excellent agreement between the observed short-range spin correlations and the calculated correlations from the *ab initio* DLM-DFT-SIC approach is notable for two reasons. First, it demonstrates that we now have a quantitatively accurate, first-principles model of the magnetic properties of MnTe in the high-temperature regime, where thermoelectric applications would be most likely. This lays the groundwork for future theoretical investigations of MnTe, including potential ways to improve the thermoelectric performance by paramagnon engineering. Second, these results further establish the DLM-DFT-SIC approach as a versatile and reliable method of predicting finite-temperature magnetic properties, having now seen success in numerous materials with diverse magnetic and electronic properties [56, 57, 60, 67–70]. Specific to the search for high-performance thermoelectric systems, this *ab initio* framework can be used to screen candidate materials for the possibility of short-range magnetic correlations that may enhance zT through paramagnon drag.

4.12 Conclusion

In summary, we have performed mPDF analysis and *ab initio* calculations of MnTe to reveal the real-space nature of the short-range magnetic correlations responsible for enhancing zT above

T_N. We have shown that robust, short-range magnetic correlations persist on the nanometer scale well above T_N, consistent with the paramagnon picture proposed to explain the high value of zT. Further, we have demonstrated that these magnetic correlations are anisotropic, with a longer correlation length out of the plane than in the plane, a consequence of anisotropic exchange interactions. *Ab initio* calculations using the DLM-DFT-SIC method predict the observed anisotropic magnetic correlations with quantitative accuracy, validating this approach for the theoretical study of magnetically enhanced thermoelectric candidates. By offering unprecedented insight into the nature of the short-range magnetic correlations responsible for the enhanced thermoelectric response in MnTe, these results provide a vital benchmark for future efforts to quantify, understand, and optimize spin-driven thermoelectric enhancement due to short-range magnetic order in MnTe and other magnetic semiconductors.

Chapter 5

Magnetovolume effect in MnTe and Na-doped MnTe

Note: This chapter forms the basis of a paper that will be submitted for publication, and as such, it reflects a collaborative effort from all co-authors. Those coauthors include Raphaël P. Hermann, Branton Campbell, and Milinda Abeykoon.

5.1 Overview

We study the spontaneous magnetovolume effects and magnetostructural coupling in MnTe and Na-doped MnTe using the X-ray pair distribution function technique. We observe the largest spontaneous magnetovolume effect reported so far on any antiferromagnetic system, reaching a volume contraction of $\Delta V/V \sim -8 \times 10^{-3}$ for both MnTe and Na-MnTe . Comparing the structural response to the local magnetic order determined by mPDF analysis, we find a linear correlation between the magnitude of the magnetovolume shift and the locally ordered magnetic moment. This linear dependence of the structural response on the magnetic moment is counter to the conventional quadratic magnetostriction response and instead hints at a more unusual form of magnetostructural

coupling reminiscent of an intrinsic piezomagnetic response.

5.2 Introduction

Magnetostructural coupling refers to the coupling of the crystal structure with the magnetic degree of freedom. Materials with this type of coupling play a crucial role in various functional materials. For example, giant magnetocaloric [71] materials exhibit a magnetically-driven structural phase transition or magnetoelastic phase transition in response to an applied magnetic field and the intrinsic ferromagnetic phase transition, which can be utilized for solid-state refrigeration. Magnetostuctural coupling is also relevant to multiferroics [72, 73] and multifunctional anti-perovskites [74], where the intertwined magnetic order and structural parameters can lead to unusual conversion between electric and magnetic fields, enabling novel devices. Magnetostriction, by which the unit cell dimensions change in response to an applied magnetic field or intrinsic magnetic order, is widely exploited in sensors, actuators, transducers, and other practical energy conversion devices [75].

Given the technological importance of magnetostructural coupling, it is likewise important to understand the fundamental physics behind the origin of these behaviors. Here we focus on magnetostriction, specifically the magnetovolume effect. This refers to the magnetostrictive response of the unit cell volume to an applied magnetic field (driven magnetostriction/magnetovolume effect) or intrinsic magnetic order (spontaneous magnetostriction/magnetovolume effect). In the case of the spontaneous magnetovolume effect, it is observed as a change in unit cell volume as a function of temperature that goes beyond the usual thermal expansion trend. For example, it can manifest as an anomalous contraction or expansion of the volume across a magnetic phase transition, seen as a departure from the high-temperature thermal expansion trend above the magnetic transition. The driven magnetostriction response of ferromagnets is quite well understood in terms of domain wall movements, but spontaneous magnetostriction–in particular for antiferromagnets–remains much

less well studied, inviting further investigation.

In this paper, our focus is to characterize and understand the spontaneous magnetovolume and magnetostructural coupling observed in MnTe and Na-doped MnTe. We use X-ray PDF data on a very fine temperature grid to track the evolution of the lattice parameters and unit cell volume across the antiferromagnetic transition around 307 K. We observe the largest magnetovolume effect for any antiferromagnetic material reported to date, with strong contractions along the *c* axis and within the *ab* plane as the temperature is lowered into the magnetically ordered state. Intriguingly, the magnetovolume response starts well above the Néel temperature, indicating that the short-range magnetic correlations in the paramagnetic state investigated previously are responsible for driving a long-range lattice response. We argue that once the temperature is lowered to $\sim$375 K, the magnetic correlation length is long enough to trigger the lattice response. However, above 375 K, the correlation length is too small to show any noticeable magnetostructural coupling. Finally, we demonstrate a linear dependence of the volume shift on the locally ordered magnetic moment, in contrast to the quadratic dependence expected for conventional magnetostriction. This linear response is reminiscent of a type of intrinsic piezomagnetism that may arise due to the presence of robust internal fields even in the paramagnetic state. We discuss these results in the context of the Landau free energy.

5.3 Experimental details

The preparation details of the polycrystalline samples MnTe and 2% Na doped MnTe were already discussed on Chapter 3. X-ray pair distribution (xPDF) experiments were performed at beamline 28-ID-1 of National Laboratory Synchroton Light Source II at Brookhaven National Laboratory using the X-ray wavelength of 0.19 Å. The pure (MnTe) and doped (2% Na doped MnTe) samples were loaded into a thin polyimide tubing of length 10 mm inside the glove box and were sealed with

modeling clay. These samples were then placed in liquid Helium cryostat mounted on the beamline and the diffraction pattern was collected on a large area detector made of amorphous silicon. The diffraction patterns were azimuthally integrated using FIT2D [76] to obtain a one-dimensional pattern. These one-dimensional patterns were then normalized and Fourier-transform using Q_{max} = 25 $Å^{-1}$ to reproduce the X-ray PDF data using XPDFsuite software [44]. The X-ray PDF analysis were performed using PDFgui [46]

5.4 Results

5.4.1 Temperature dependence of the lattice parameters and unit cell volume

The X-ray PDF data were collected on a dense temperature grid between 5 K to 500 K in steps of 5 K. Fig. 5.1 (a) shows the representative X-ray pair distribution fit (xPDF) of MnTe using the published crystal structure. The agreement between the observed data (represented by blue symbols) and calculated pattern (represented by red curve) confirms the good quality of the fit with R_w = 8.2%. The fit residual shown by the green curve at the bottom of the panel (offset for clarity) likewise demonstrates the relatively good fit quality. The insert shows the crystal and magnetic structure of MnTe with Mn-spins on the *ab*-plane. Note that in the X-ray PDF data, the magnetic contribution is negligible, in contrast to the neutron PDF, where both the atomic and magnetic PDF components were clearly visible and could be reliably modeled. For that reason, the fits to the X-ray PDF data include only the atomic structure. Fig. 5.1(b) shows the representative fit of Na-doped MnTe with R_w = 9.3%, and insert shows the structure and spin orientations of 2% Na-doped MnTe. The fit quality is reduced slightly compared to the pure compound, most likely due to the disorder caused by the sodium impurity ions. Our previous study of magnetic pair distribution function (mPDF) analysis of Na-doped MnTe shows that the Mn-spins oriented vertically along the *c*-axis [7].

In Fig. 5.2 (a) and (b), we display the temperature dependence of the best-fit lattice parameters

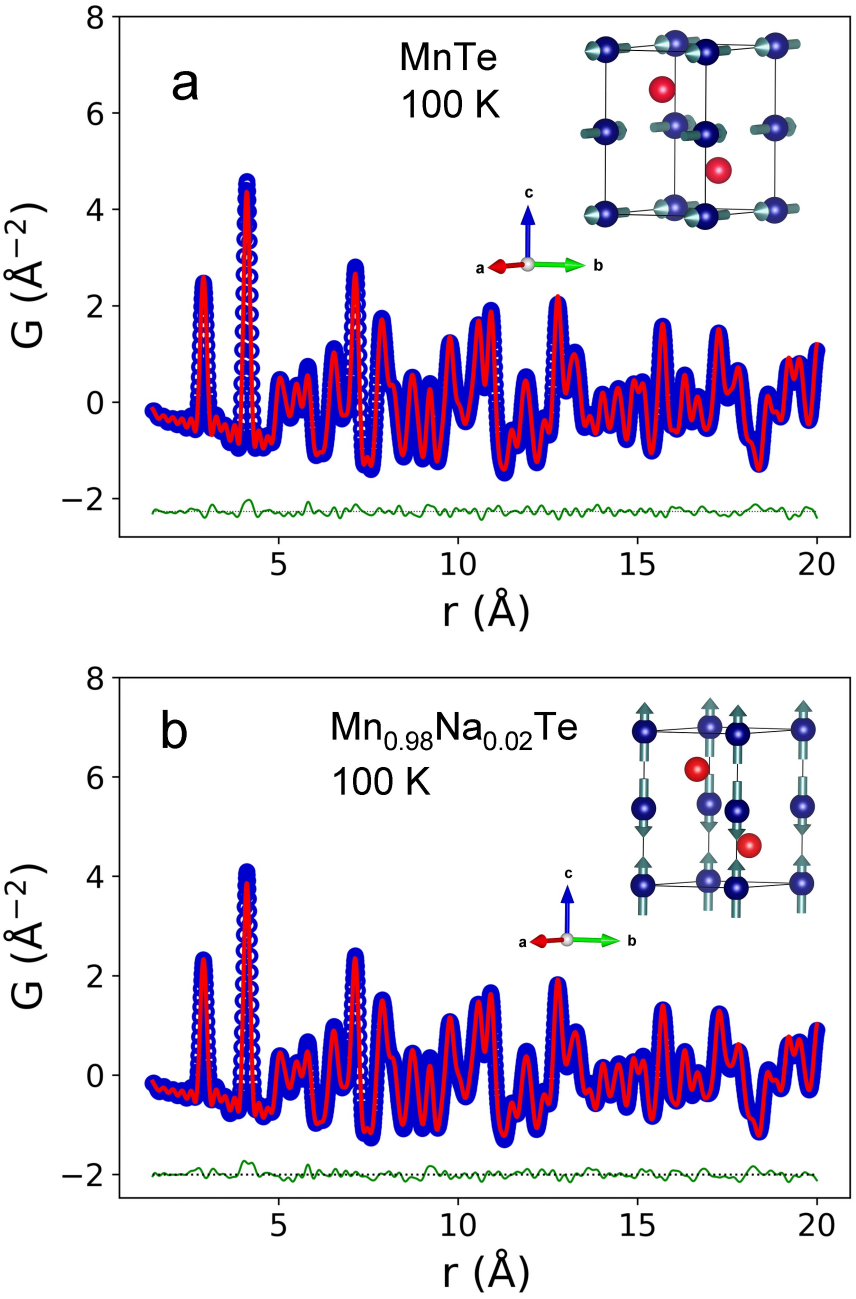

Figure 5.1 (a) X-ray PDF data (blue symbols) and fit (red curve) for MnTe at 100 K. The green curve represents the fit residual, offset vertically for clarity. Insert: crystal and magnetic structure of MnTe. Blue and red spheres represent Mn and Te atoms, respectively. (b) X-ray PDF fits for 2% Na-doped MnTe. Insert: crystal and magnetic structure of Na-doped MnTe.

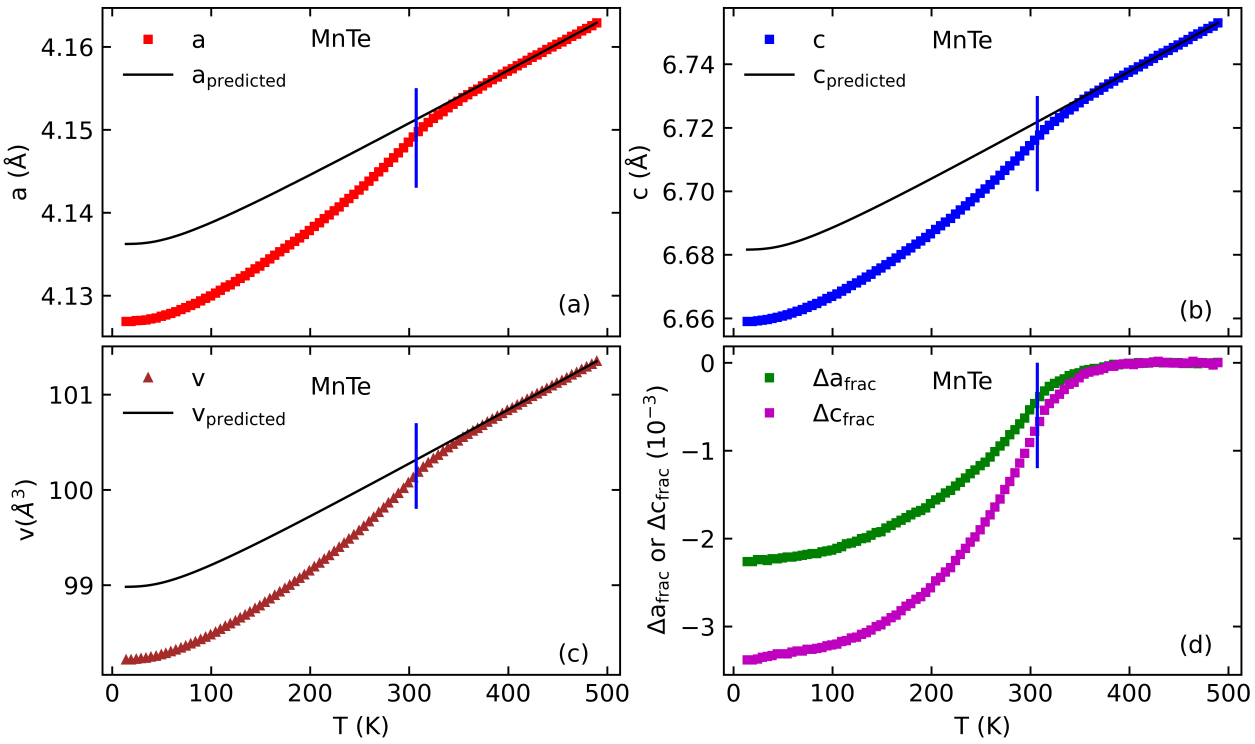

Figure 5.2 (a-b) Temperature dependence of the lattice parameters a (red symbols) and c (blue symbols) determined from the X-ray PDF fits of MnTe. (c) The variation of unit cell volume (V) of MnTe as a function of temperature. The thin black lines show the high-temperature Grüeneissen fits extrapolated to lower temperatures. (d) Anisotropic magnetostriction in pure MnTe is quantified by Δa_{frac} (green symbols) and Δc_{frac} (magenta symbols) as a function of temperature.

a, and c for pure MnTe determined from the fits conducted in PDFgui. Both lattice parameters (a and c) show a linear temperature dependence above 350 K, but an anomalous decrease is observed as the temperature is lowered towards the Néel temperature (T_N 307 K). A similar trend is also observed when we plotted unit cell volume (V) with the temperature of MnTe, which is shown by brown symbols in Fig. 5.2 (c). The lattice parameters and unit cell volume of Na-doped MnTe are shown in Fig. 5.3 (a-c). The results for Na-doped MnTe look very similar to pure MnTe. For both pure and Na-substituted MnTe, then, there is a clear contraction of the unit cell volume that occurs in conjunction with the establishment of the antiferromagnetic order.

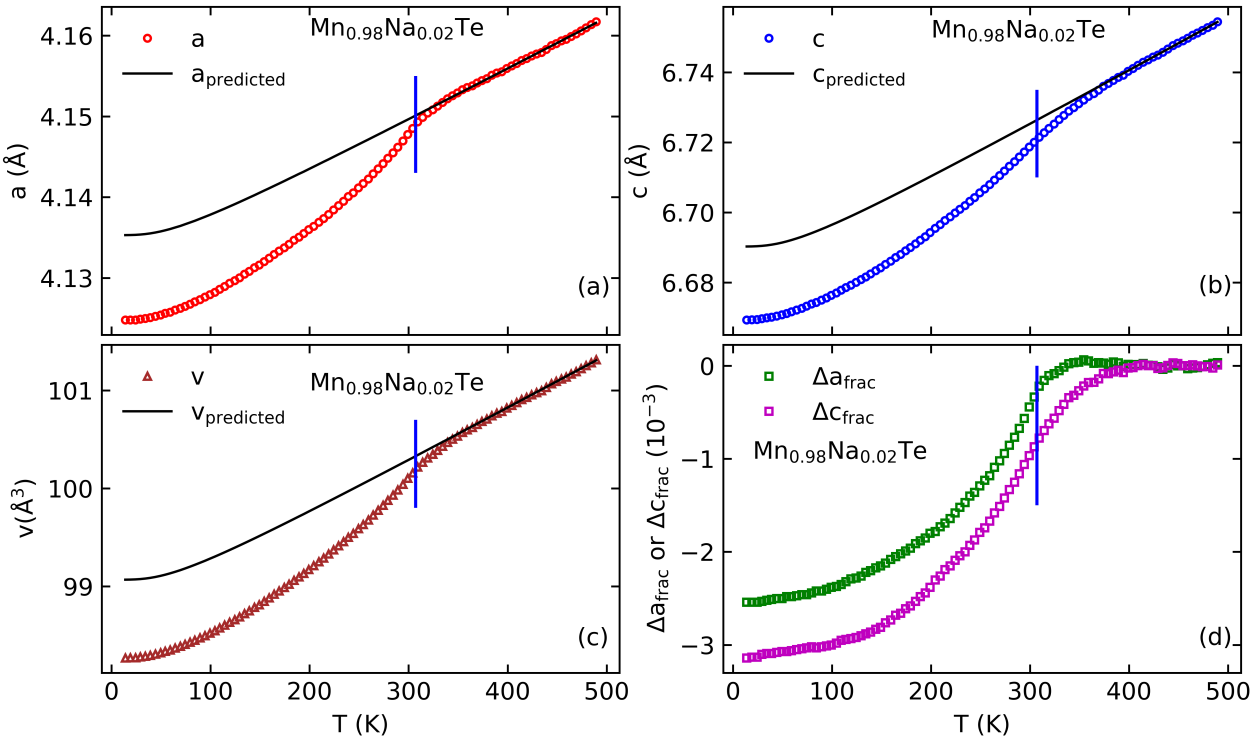

Figure 5.3 (a-b) Temperature dependence of the lattice parameters a (red symbols) and c (blue symbols) determined from the X-ray PDF fits of Na-doped MnTe. (c) The variation of unit cell volume (V) of Na-doped MnTe as a function of temperature. The thin black lines show the high-temperature Grüneisen fits extrapolated to low temperature. (d) The fractional change in lattice parameters (Δa_{frac} and Δc_{frac}) plotted together as a function of the temperature of Na-doped MnTe.

5.4.2 Quantifying the magnetovolume effect using the Grüneisen equation of state

To gain a more quantitative understanding of the magnetovolume effect in MnTe, we turn to modeling of the high-temperature lattice parameter and unit cell volume trends. The objective is to predict what the lattice parameter value would be as a function of temperature in the *absence* of any magnetism, and then compare that prediction to the observed lattice parameter values. This

difference between the observed lattice parameters and the expected lattice parameters in the absence of magnetism then represents the magnetostructural coupling in MnTe.

One approach would be to use a simple linear fit to the extracted lattice parameters for 350 K and above, where the influence of the magnetism on the structure appears to be negligible, and then extrapolate the linear trend to lower temperatures, down to 5 K to match the data. However, such a simplistic approach would introduce errors at temperatures significantly below the Debye temperature, where phonon modes begin to freeze out and linear thermal expansion is no longer expected. A more accurate approach is to adopt the Grüneisen equation of state for zero temperature (along with Debye approximation of the internal energy). The Grüneisen equation of state, modified for lattice parameter [77, 78], is given by

$$y(T) = \alpha T(\frac{T}{T_D})^3 \int_0^{T_D/T} \frac{x^3}{(e^x - 1)}\, dx + y_0, \tag{5.1}$$

where $\alpha = 9Nk_B\gamma/B_0$, γ is the Grüneisen parameter, B_0 is the bulk modulus at 0 K, T_D is the Debye temperature and y_0 is the lattice parameter at 0 K. Similarly, the Grüneisen equation for the temperature dependence of volume [77, 78] is given by

$$V(T) = \alpha T(\frac{T}{T_D})^3 \int_0^{T_D/T} \frac{x^3}{(e^x - 1)}\, dx + V_0, \tag{5.2}$$

where $V(T)$ and V_0 are the unit cell volumes at temperature T, and 0 K, respectively.

In the approach using the Grüneisen equation, one must select a value for the Debye temperature, then fit the model to the data in the high-temperature regime where the magnetism has a negligible effect on the data, and then extrapolate the model to lower temperatures. This model successfully captures the leveling off of the thermal expansion at sufficiently low temperatures that is missed by the simple linear thermal expansion model.

To model the MnTe and Na-doped MnTe, we did Grüneisen equation fits for the lattice parameter and unit cell data 400 K and above, using the experimentally determined value of the Debye temperature of T_D = 223 K reported in previous work [3]. We then extrapolated the calculated lattice

parameters and unit cell volume to a lower temperature, as shown by the black solid line in Fig. 5.2. This curve thus represents the expected temperature dependence of the unit cell dimensions without the influence of any magnetism. The fit results gave us $\frac{\gamma}{B_0} = 3.479 \times 10^{-11}$ Pa^{-1} and $V_0 = 98.9815$ Å^3. We also perform similar fits using a Debye temperature of 140 K as predicted theoretically elsewhere [16]. The effect on the fit is quite minimal, meaning that the model is not very sensitive to the precise value of the Debye temperature. In that case, we stick to the experimentally estimated Debye temperature of 223 K for our calculation.

We also performed similar Grüneisen equation fits to the Na-doped MnTe (shown by the black line in Fig. 5.3) using the same Debye temperature $T_D = 223$ K. The fitting results gave us $\frac{\gamma}{B_0} = 3.2896 \times 10^{-11}$ Pa^{-1} and $V_0 = 99.0678$ Å^3.

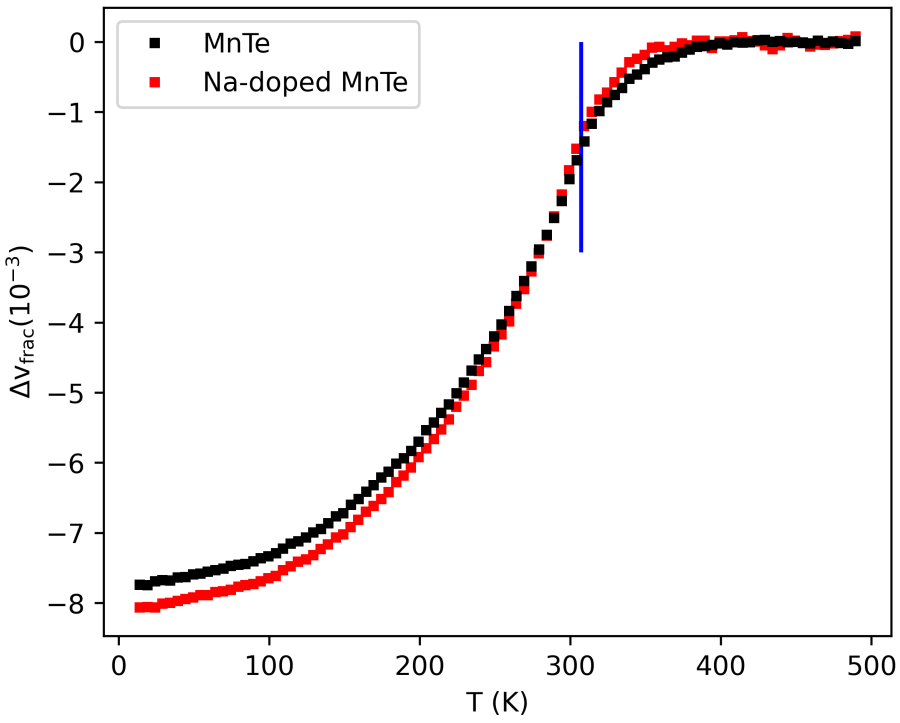

Figure 5.4 Fractional change in volume with temperature. Black and red square symbols represent the fractional change in volume of pure MnTe and Na-doped MnTe respectively. The vertical blue line represents the Néel temperature (307 K).

From the experimental lattice parameters and the predicted lattice parameters using the Grüneisen model, we can calculate the fractional change in lattice parameters due to the influence of the magnetism. This is obtained by subtracting the individual lattice parameters at various temperatures ranging from 5 K to 500 K from paramagnetic predicted (extrapolated line) lattice values determined through Grüneisen equation fits, then normalized by the paramagnetic predicted lattice values to give a dimensionless quantity representing the magnetovolume effect. Shown explicitly, we have

$$\Delta a_{frac} = \frac{a - a_{predicted}}{a_{predicted}} = \frac{\Delta a}{a_{predicted}}, \tag{5.3}$$

$$\Delta c_{frac} = \frac{c - c_{predicted}}{c_{predicted}} = \frac{\Delta c}{c_{predicted}}, \tag{5.4}$$

and

$$\Delta V_{frac} = \frac{V - V_{predicted}}{V_{predicted}} = \frac{\Delta V}{V_{predicted}}. \tag{5.5}$$

Fig. 5.2 (d) shows the fractional change in refined lattice parameters Δa_{frac} and Δc_{frac} of MnTe with temperature plotted together. The fractional change in lattice parameter c (Δc_{frac}) is about 50% larger than the fractional change in lattice parameter a (Δa_{frac}). A similar trend is also observed for the Na-doped MnTe shown in Fig. 5.3 (d), where Δc_{frac} is larger than Δa_{frac}, but the difference between them is less than it is for the pure MnTe sample. We also note that the lattice c begins to respond slightly higher temperature (around 375 K) than for lattice a.

One way to verify the accuracy of the current approach is to note that Δa_{frac} and Δc_{frac} are zero for $\sim$400 K and above. This indicates that the high-temperature trend is successfully captured by the model, and that the magnetically induced volume contraction is not influencing the model in the high-temperature limit. If we were to select 307 K and above for the Grüneisen fits, then the non-magnetic model would be distorted by the magnetically induced response of the lattice parameters that we see for temperatures up to 350 K. In this case, the fractional lattice parameter shifts would not approach zero in the high-temperature limit, but would instead have some systematic deviation from zero.

In addition to the temperature dependence of the lattice parameters, we also plot the variation of the unit cell volume with temperature for pure MnTe and Na-doped MnTe samples in Fig. 5.2 (c) and 5.3 (c), respectively. The black solid line represents the Grüneisen fit done on the unit cell volume using the equation 5.2. The magnitude of the fractional change in volume (ΔV_{frac}) was observed to be about 7.7×10^{-3} for pure MnTe and about 8.0×10^{-3} for Na-doped MnTe, which are shown in the Fig. 5.4. This is the largest spontaneous magnetovolume effect reported for any antiferromagnetic material to date. We can compare this result to model antiferromagnets like CrF_2 (-7.72×10^{-4}), CuF_2 (-1.16×10^{-4}) [78], MnF_2 (-10.02×10^{-4}), and NiF_2 (-4.5×10^{-4}) [77]. Thus, MnTe exhibits exceptionally large magnetostructural coupling for an antiferromagnet.

5.4.3 Local magnetic moment coupling with lattice and volume shift

The temperature dependence of the lattice parameter shift makes it clear that magnetism is implicated in the contraction of the lattice as the temperature is lowered across the magnetic transition. However, the lattice response begins well above the Néel temperature, indicating that the short-range magnetic correlations present in the paramagnetic state are already sufficient to induce a change in the long-range crystal structure. To explore the connection between the magnetism and the lattice response in more detail, we compare the X-ray PDF results with the mPDF results obtained from the neutron PDF experiments described previously.

Fig. 5.5 (a) shows the local magnetic order parameter (LMOP) plotted on the left vertical axis (orange squares) and the volume shift (blue symbols) plotted on the right vertical axis versus temperature. The values of LMOP are taken from our previous mPDF analysis [7]. We define the LMOP as the magnitude of the ordered magnetic moment between nearest-neighbor Mn spins as determined by the mPDF fits conducted on the fitting range $1.5 - 20$ Å. In the purely long-range ordered state, the LMOP is the same as the average sublattice magnetization. In the short-range ordered state above the Néel temperature, the ordered moment between a pair of spins decreases

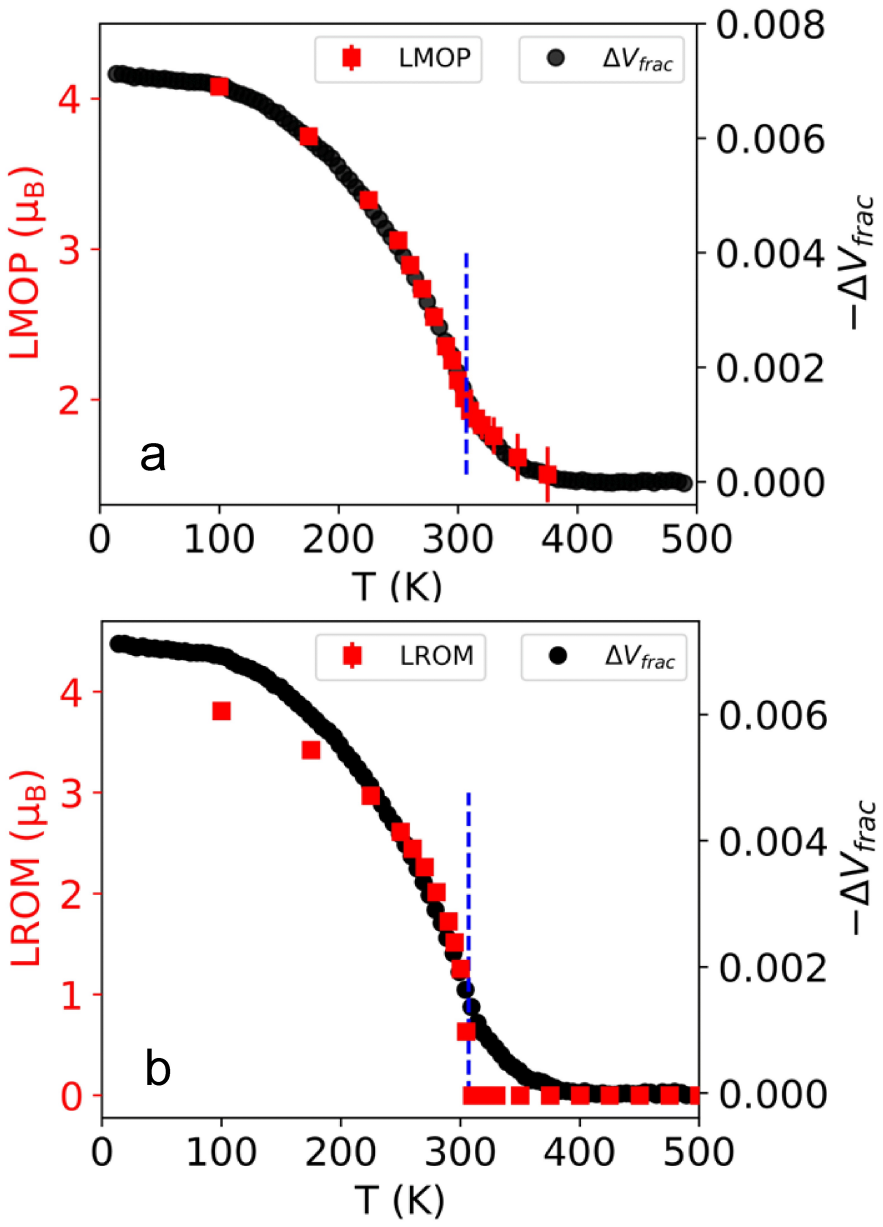

Figure 5.5 (a) Local magnetic order parameter (LMOP) represented by red symbols in the left vertical axis and volume shifts ($-\Delta v_{frac}$) represented by a black symbol in right vertical axis with temperature. (b) Long-range order moment (LROM) and volume shifts with temperature. A vertical blue dash line is drawn at the transition temperature (307 K).

exponentially with separation distance, so the LMOP refers specifically to the nearest-neighbor spin pair. The volume shift ($\Delta V/V$ equivalent to ΔV_{frac}) is plotted as a positive quantity, but in reality it is negative due to the contraction of the lattice caused by the magnetism. We can see that there is a close correspondence between the volume shifts and the LMOP i.e., they have a one-to-one linear relationship between them. In Fig. 5.5 (b), we plot the long-range ordered moment (LROM) (left vertical axis) and volume shifts (right vertical axis) with temperature. The correlation between the volume shift and the LROM is not nearly as linear and direct as the LMOP and the volume shift, indicating that the relevant coupling is between the lattice and the short-range magnetic correlations, not the long-range correlations. Here the long-range ordered moment was calculated using the fitting range (30 - 45) Å.

The fractional change in lattice *a* is plotted against the LOMP in Fig. 5.6 (a). The linear trend is clearly visible in the data. The dashed line is the best-fit line for the data points colored red, which correspond to the data collected at 375 K and below. The open gray symbols represent the data collected above 375 K, where the lattice response is independent of the locally ordered magnetic moment, indicating that the magnetostructural coupling only kicks in below 375 K when the short-range magnetic correlations have reached a threshold correlation length. Indeed, referring back to Fig. 4.4(c), between 375 K and 350 K is where the correlation length begins to increase dramatically as the temperature is lowered further toward the Néel transition. Therefore, we can interpret these results as indicating that the lattice response couples linearly to the short-range magnetic correlations once those correlations have reached a length scale on the order of the unit cell dimensions. We see consistent behavior with the fractional change in lattice *c* and the fractional volume contraction (see Fig.5.6 (b, c)). In panel (c), we also plot in black symbols the fractional volume contraction against the long-range ordered moment. Notably, the volume changes significantly even when the long-range moment is zero, once again demonstrating that the lattice couples to the local magnetism rather than the long-range, average magnetism. However, the linear trend is recovered at sufficiently

low temperatures (upper right region of the plot) where the black symbols approach the red symbols. The lattice response observed for the Na-doped MnTe compound is extremely similar and is not shown here.

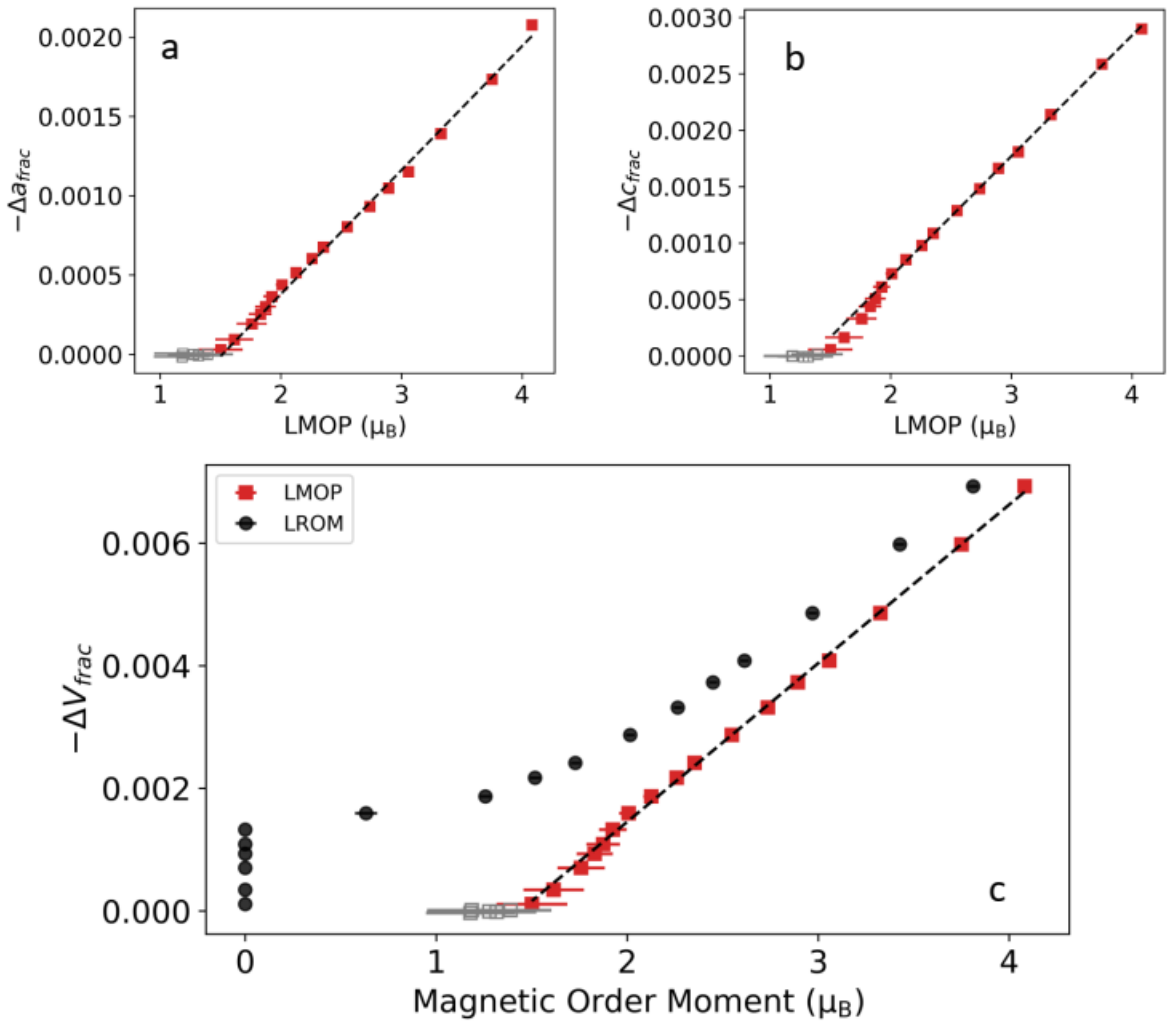

Figure 5.6 (a) Local magnetic order parameter (LMOP) and a_{frac}. (b) Local order moment parameter (LMOP) with c_{frac}. (c) Long range order moment (LROM) represented by black circles and local magnetic order parameter (red symbol) plotted together with volume shifts ($-\Delta V_{frac}$) for pure MnTe. Black dashed line represents the linear fit done below 375 K and open gray symbols represent the moments above 375 K.

5.5 Discussion

The preceding analysis of the magnetostructural response of MnTe reveals three interesting features. First, the magnitude of the magnetovolume effect is exceptionally large for an antiferromagnet, about 0.8%. Second, the response begins around 375 K, well above the Néel temperature of 307 K below which long-range magnetic order sets in. Third, the lattice response scales linearly with the local magnetic order parameter. We discuss each of these features in turn.

Regarding the large magnetovolume effect in MnTe, it is notable for being the largest reported spontaneous magnetovolume effect in an antiferromagnet (approximately an order of magnitude larger than that observed in classic antiferromagnets like CuF_2 and MnF_2), making MnTe inherently interesting for that reason. The large volume contraction is aided by the fact that both the a and c lattice parameters respond in the same way to the magnetism, i.e. contracting in response to the magnetic correlations. Therefore, they work in concert to shrink the overall unit cell volume significantly. In other cases, a large lattice contraction in one direction may be partially counteracted by an expansion in one or more other dimensions to restore the unit cell volume to what it would be in the absence of magnetism. This has been observed, for example, in various ferromagnetic magnetocalorics [79]. In the case of MnTe, the energy savings accrued by bringing the Mn atoms closer together, and therefore optimizing the magnetic exchange interactions, dominates over the elastic energy cost. Interestingly, the in-plane exchange interaction J_2 (see Fig. 3.1) is significantly weaker than the nearest-neighbor out-of-plane interaction J_1 and the second-nearest-neighbor out-of-plane interaction J_3 (-21.5 K, 0.67 K, and -2.87 K for J_1, J_2, and J_3, respectively [21]). This might suggest that elastic energy would dominate the in-plane lattice response (i.e. the a lattice parameter), leading to a very small response to the magnetic order. Indeed, we do observe that the a-axis lattice response is only about half as large as the c-axis response, which we can attribute to the larger J_1 exchange interaction, but the a-axis response is still larger than one might expect on the basis of J_2 alone. However, if we also consider that J_3 benefits not only from shortening c but

also shortening a, then the sizeable contraction of a is understandable.

We now address the observation that the lattice parameters (both a and c) in MnTe start to contract around 375 K, which is well above the magnetic ordering temperature (307 K) (see Fig. 5.2 (d)). The fact that the lattice response scales linearly with the growth of the short-range magnetic correlations in the paramagnetic state, which were characterized by our earlier mPDF work [7], demonstrates that the lattice shift above the Néel temperature is magnetically driven. This is direct evidence that short-range magnetic correlations are sufficient to trigger a long-range lattice response, a possibility that is often overlooked in typical theoretical treatments of magnetostructural coupling. These results therefore suggest that a more generalized treatment of magnetostructural coupling that explicitly considers short-range magnetic characterizations would be a valuable endeavor. To that end, we note that the magnitude of the local magnetic order parameter is not the only important factor for the lattice response; the correlation length is also implicated, since we see the linear coupling turn on only below 375 K, the temperature below which the correlation length begins to increase above its high-temperature plateau (see Fig. 4.4(c)). However, once the correlation length has reached a sufficient value and the lattice coupling to the short-range magnetism has turned on, the lattice contraction is determined largely by the locally ordered moment, and the continued increase of the correlation length as the temperature is lowered does not affect the lattice response. These observations provide useful insights into models of magnetostructural coupling when short-range magnetic correlations are present. We note that some efforts to establish a theoretical framework for relating short-range magnetic correlations to the lattice response have been made already [80]. We expect this coupling between the long-range lattice structure and short-range magnetic correlations to be relevant to numerous other magnetic materials that have significant short-range magnetism in the paramagnetic state.

We also comment briefly on the observation that for Na-doped MnTe, the lattice parameter c begins to contract at 375 K, but a only shows a significant response below about 345 K (see Fig. 5.3

(d)). The slow response of lattice a in comparison to lattice c could be due to the fact that we are adding disorder to the system in the form of Na dopant ions, which may disrupt the weaker in-plane correlations more than the more robust out-of-plane correlations. We know that the presence of Na perturbs the magnetocrystalline anisotropy, causing a switching of the moment from in-plane for pure MnTe to out of a plane for Na-doped MnTe composition, demonstrating that the system is already quite sensitive to the presence of dopants.

Finally, we discuss the linear nature of the coupling between the lattice contraction and the local magnetic order parameter. This linear behavior is in contrast to conventional magnetostriction, for which lattice strains couple to the square of the ordered magnetic moment. This can be understood by examining the free energy. The invariance with respect to time reversal requires that only even powers of the magnetization m be present in the absence of an external magnetic field, such that $t \rightarrow -t$ causes $m \rightarrow -m$ but does not reverse the sign of the free energy. Thus, the leading free energy terms involving lattice strain and the magnetic order parameter are given by

$$u = c_1 m^2 + c_2 e^2 + c_3 e m^2, \tag{5.6}$$

where c_1, c_2, and c_3 are constants, e is the lattice strain, and m represents the magnetic order parameter. On differentiating the above equation with respect to lattice strain e and setting the result to zero, we find $e = \frac{-c_3}{2c_2} m^2$. Thus, the lattice couples with the square of the ordered moment, which is something we expect for conventional magnetostriction.

We then must ask the question of how a linear lattice response to the local magnetic order parameter can be possible. If we note the behavior of the short-range magnetic correlations in the paramagnetic state displayed back in Fig. 4.4, we see that the high-temperature behavior approaches a stable, temperature-independent state with a local magnetic order parameter of approximately 1 μ_B and a correlation length of approximately 3 Å. We can consider this to be a sort of constant "background field", and as the temperature is lowered toward the Néel temperature, longer-range magnetic correlations (but still not infinitely long correlations) build up on top of this constant

short-range background field. With this picture in mind, we can express the free energy explicitly in terms of the short-range ordered moment m_s from the background field and the longer-range moment m_l as

$$u = c_1 m_s^2 + c_2 m_l^2 + c_3 e^2 + c_4 e m_s m_l. \tag{5.7}$$

On differentiating the above equation with respect to the lattice strain and setting the result to zero, we obtain $e = -\frac{c_4}{2c_2} m_s m_l$. This implies that lattice strain couples linearly with m_l channel, assuming that m_s is independent of temperature (as is suggested by our mPDF analysis). In this way, we can rationalize the linear response of the lattice to the growth of the local magnetic correlations on top of the constant background of short-range magnetism. To our knowledge, this type of behavior has never been reported before, suggesting that this is a novel scenario for magnetostructural coupling. Indeed, a linear lattice response is typically associated with piezomagnetism, by which the lattice dimensions change in response to an applied magnetic field in linear fashion. The picture of piezomagnetism becomes less well defined in the case of the spontaneous magnetovolume effect observed here in the absence of any external magnetic field, but if we consider the constant background field of short-range magnetic correlations to play the role of the external field, then we can draw an analogy to a piezomagnetic response in MnTe. This interesting situation in MnTe may motivate additional studies to search for similar effects in other magnetic materials.

5.6 Conclusion

In summary, by combining our mPDF analysis with X-ray PDF analysis, we gained a detailed picture of the magnetostructural response in MnTe. We observed a spontaneous volume contraction of 0.8%, the largest spontaneous magnetovolume effect reported so far for any antiferromagnetic system. We demonstrated that the relevant coupling is between the long-range lattice and the short-range magnetic correlations, rather than the long-range ordered magnetic moment. We showed

that the lattice strain scales linearly with the local magnetic order parameter, in contrast to the quadratic scaling observed for the conventional magnetostriction properties of this technologically relevant material, and we rationalized this by considering two separate magnetic order parameters, one for the very short-ranged, temperature-independent correlations that survive up to the highest measured temperatures, and the other for the longer-range correlations that grow as the temperature is lowered. Finally, this study highlights the unique value of combined atomic and magnetic PDF analysis in materials with magnetostructural coupling.

Chapter 6

Local distortion in MnTe

Note: This chapter forms the basis of a paper that will be submitted for publication, and as such, it reflects a collaborative effort from all coauthors. Those coauthors include Raphaël P. Hermann, Emil Bozin, and Milinda Abeykoon.

6.1 Overview

Using PDF analysis, we have observed a large distortion in the local structure of MnTe involving an off-centering of the Te atom. We investigate the temperature dependence of this local distortion and find that it grows continuously with increasing temperature, appearing as a distinct feature in the PDF fit residual around 100 K and becoming more pronounced at higher temperature. This is contrary to the typical behavior of local symmetry breaking developing as the temperature is lowered, pointing to a more unusual origin of this feature. We compare the observed distortion in MnTe to known local distortions in other thermoelectrics such as PbTe called "emphanisis", which is likewise found with increasing temperature. Although there are important differences between the chemical and structural origin of emphanisis in other thermoelectrics and the distortion observed in MnTe, the commonalities may point to a more ubiquitous phenomenon. To that end, we also

performed a comparative analysis with other Mn-based systems MnS and MnO, where a similar distortion was also found.

6.2 Introduction

In recent years, various high-symmetry thermoelectric materials have been found to exhibit a local distortion observable in the low-r region of the PDF data that appears with warming, while no change is seen in their average crystal structure. This was first discovered in the cubic thermoelectric materials PbTe and PbS [81], where the Pb atom shifts off its high-symmetry position upon warming up to higher temperature. However, the Pb shifts in neighboring unit cells are not strongly aligned with each other, leaving the average structure cubic even while the Pb atoms individually occupy non-cubic positions. This behavior in PbTe is believed to be due to stereochemical activity with $6s^2$ lone pair in Pb^{2+}. This phenomenon of spontaneous off-centering of the atom at elevated temperature has been named "emphanisis". This is illustrated for a selenium-based cubic thermoelectric in Fig. 6.1 (adpated from [8]), where one can see the undistorted and distorted (off-centered) positions of the Se atoms. Fig. 6.1 (a) shows the undistorted position of the Se atoms, whereas Fig. 6.1 (b) shows the distortion of Se atoms along the crystallographic directions [111] while warming up. This type of distortion creates long and short bond lengths with neighbouring atoms, and can disrupt the phonon transport [8] leading to low thermal conductivity and thus an enhanced thermoelectric figure of merit (zT), since thermal conductivity is inversely related to zT.

This type of emphanisis effect has been observed in multiple other thermoelectric materials [8, 82, 83], various perovskite systems [84], and non-magnetic Scheelite [85]. The common thread across these materials is the presence of an unbonded "lone pair" of electrons, which is not easily accommodated in the high structural symmetry of the host crystal. This can lead to local symmetry breaking that appears in a dynamical fashion as the temperature is raised.

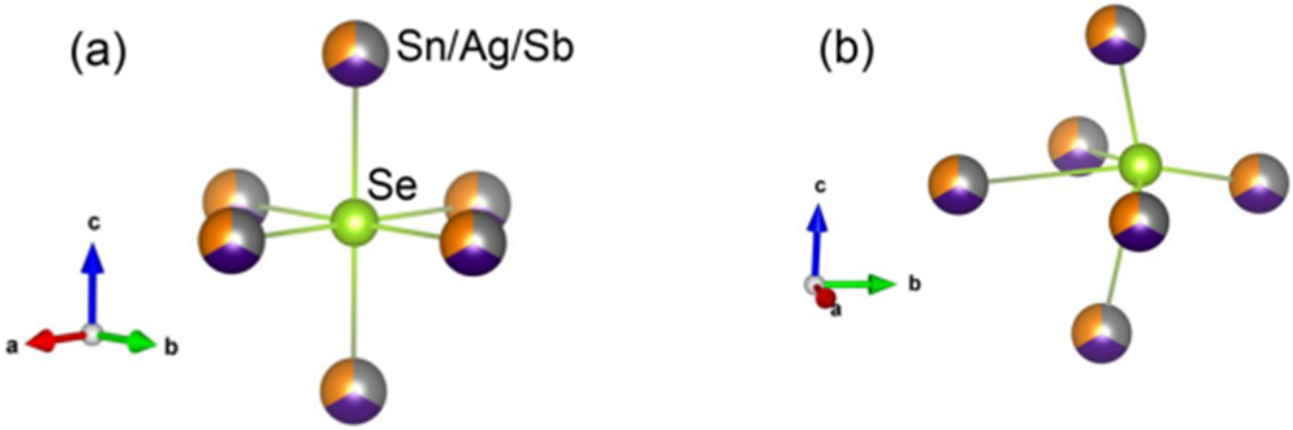

Figure 6.1 (a) Octahedral environment of Se with Se in an undistorted position. (b) Emphanitic distortion of Se along a crystallographic [111] direction. Figure adapted from [8].

Due to the short-range nature of the structural distortions characteristic of emphanisis, PDF analysis has been an excellent tool to study this phenomenon [32]. The emphanitic off-centering of the ions leads to short and long bonds, which are manifest in an asymmetry or splitting in the first few peaks of the PDF pattern. The ability to collect PDF data rapidly at synchrotron X-ray sources allows for a thorough temperature-dependent study of the local structure of materials, making it ideal for studying emphanisis. Neutron PDF does not offer such rapid data collection as X-ray PDF, but the differing scattering contrast between X-rays and neutrons makes it highly complementary to X-ray PDF for emphanisis studies.

Here, we investigate the high-performance thermoelectric candidate MnTe with X-ray and neutron PDF to determine the local structure as a function of temperature. We observe significant distortion in low-r region of the PDF that grows upon warming and cannot be modeled by the long-range hexagonal crystal structure. This distortion is strikingly similar to the distortion observed in the canonical emphanitic materials, both in terms of the temperature dependence and the specific features in the PDF data. Interestingly, MnTe does not have any lone pairs, indicating that a different

mechanism is at work for the emphanisis-like behavior observed. This implies that emphanisis could be a broader phenomenon with multiple mechanisms and more widespread applicability. To support this idea, we demonstrate similar emphanisis-like behavior in MnO and MnS.

6.3 Experimental details

The details of sample preparation and basic characterization of MnTe was already discussed on Chapter 3. Similarly, the experimental details of neutron PDF and X-ray PDF of MnTe was also discussed on Chapter 4, and Chapter 5, respectively. Both xPDF and nPDF data were fitted using the PDFgui software [46] and the python package diffpy.mpdf.

6.4 Results and discussion

We fit the hexagonal $P63/mmc$ structural model to the X-ray PDF data, which we collected between 5 K and 500 K in steps of 5 K. The fitting range we chose was 1.5 – 20 Å. Fig. 6.2 shows the fits zoomed into the first peak and also displayed over the full fitting range for the representative temperatures 100 K, 350 K, and 450 K. A mismatch between the model and the data is clearly seen for the first nearest neighbor peak at 350 K, where the experimental peak is shifted to lower r and becomes more asymmetric relative to the calculated peak. This results in a spike in the fit residual at that position. Smaller misfits are also observed for the second large peak in the data. For higher r, however, the calculation matches the position and height of the peaks very accurately, indicating that the local distortion averages away to zero beyond about 5 Å. At 450 K, the mismatch is even more pronounced, indicating that the local distortion increases on warming. In contrast, the distortion is smaller at 100 K, with the calculated and observed peak positions and shapes agreeing closely.

The shifting of the first peak to lower r relative to the calculated peak is somewhat unexpected,

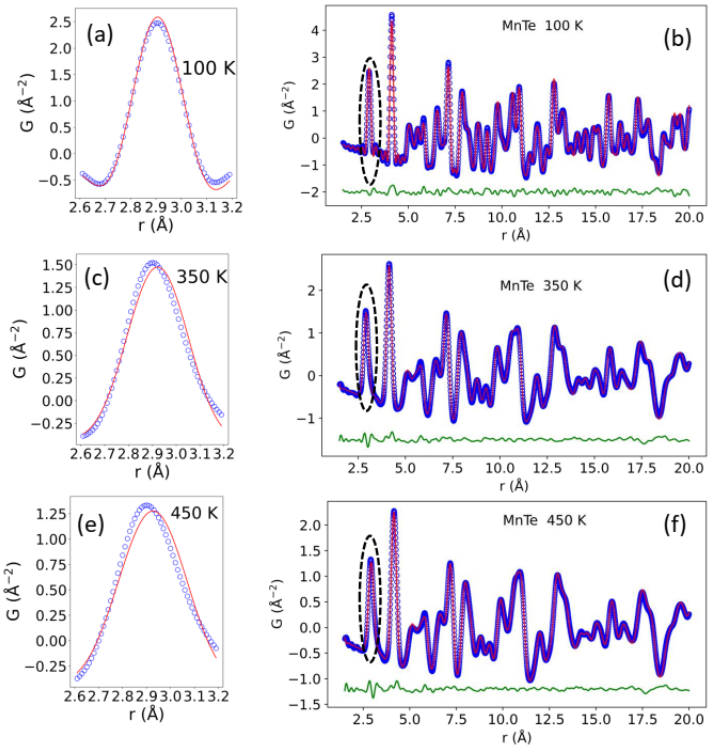

Figure 6.2 X-ray PDF fits of MnTe.Blue open circles represent experimental PDF and the red solid line represents the calculated fits using $P63/mmc$ model. A flat green curve (offset for clarity) is the fit residual. Right panel graphs show the xPDF fits at 100K, 350 K, and 450 K, respectively, whereas, left panel graphs show the zoom-in figure of nearest neighbor distribution at respective temperatures.

since thermal expansion will normally cause the peaks to shift to a higher *r*- region with increasing temperature. A waterfall plot showing the first 6 Å of the PDF data between 5 K and 500 K is shown in Fig. 6.3, where the first peak shows a slight shift to the left with increasing temperature, while the second peak shows the usual shift to the right due to thermal expansion. The vertical dashed lines mark the position of the peak maxima at 5 K to serve as reference points as the temperature is increased.

To gain a more comprehensive understanding of this local distortion as a function of temperature, we extracted the position of the nearest-neighbor peak maximum from the experimental data and from the best-fit calculated PDF and compared the two sets of values. The results are shown in Fig. 6.4. We see that the calculated and observed peak maxima agree well below about 50 K, but the discrepancy increases continuously as the temperature is raised. Thus, although the misfit is not obvious for the 100 K data shown in Fig. 6.2(a), it is nevertheless still present at 100 K and somewhat below, and it grows steadily as the temperature increases.

To confirm the presence of this distortion, we return to the neutron PDF data discussed earlier in the context of the magnetic PDF. Fig. 6.5 shows the fitted nPDF data (right panel) at 100 K, 350 K, and 450 K, respectively, together with a zoomed-in view of the first nearest peaks at those respective temperatures. Similar to the xPDF, the first peak of the experimental nPDF pattern also shifts towards the left relative to the calculated peak and becomes asymmetric with a rise in temperature. Note that the negative scattering length of manganese causes the first peak (corresponding to Mn-Te pairs) to be negative in the nPDF pattern.

This local distortion is characterized by a contraction and asymmetric skew of the Mn-Te nearest neighbor bond length as the temperature is raised. This is consistent with the idea of Te shifting off its high-symmetry position, similar to the published reports of emphanisis. Noting that each Te atom sits in the center of a triangular prism with six equidistant nearest neighbor atoms (see Fig. 6.6(c)), a shift of the Te atom toward one face of the triangular prism as shown by the arrows would shorten

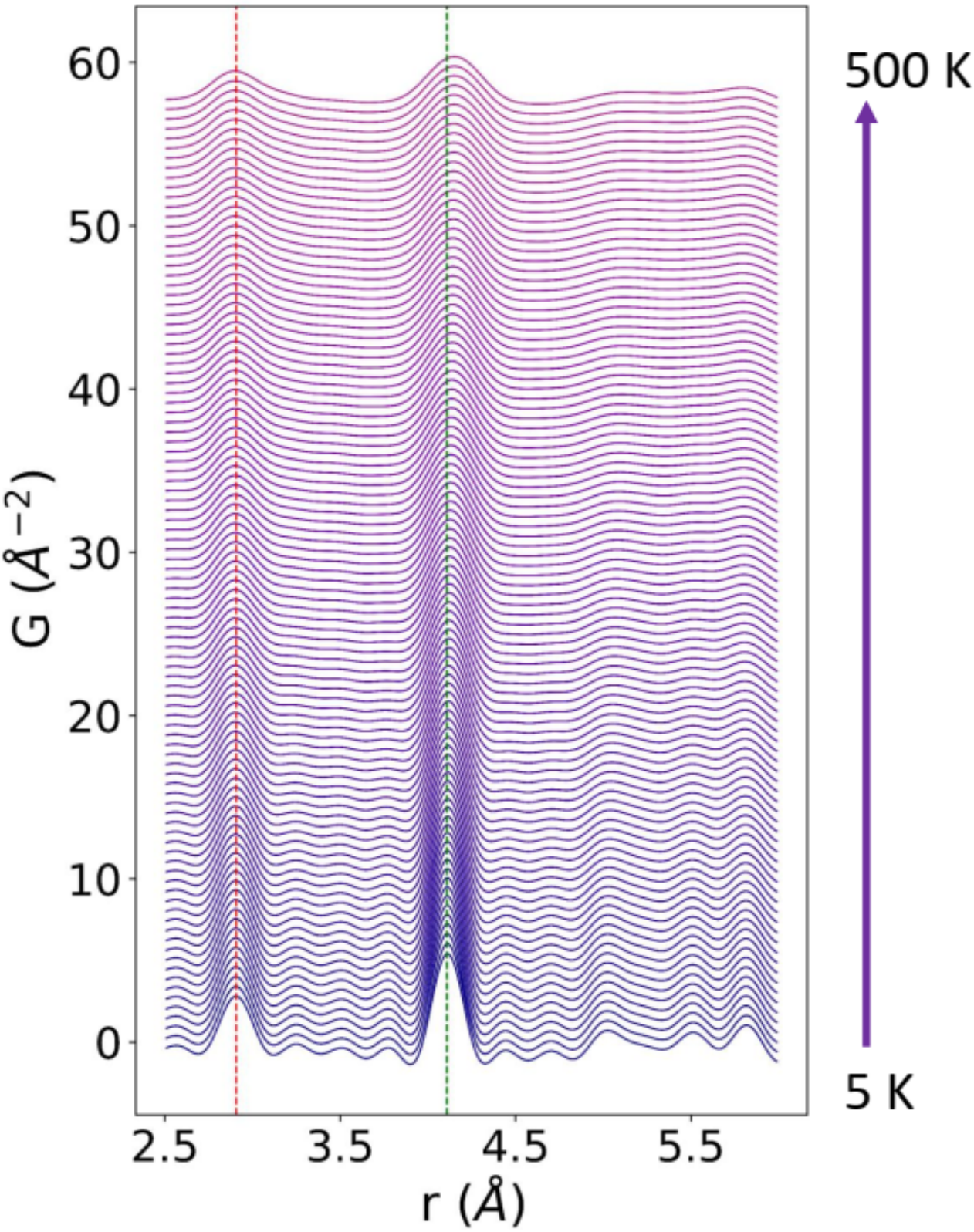

Figure 6.3 Waterfall plot representing first and second peaks, generated through X-ray PDF $G(r)$ data from 5 K to 500 K (offset for clear view).

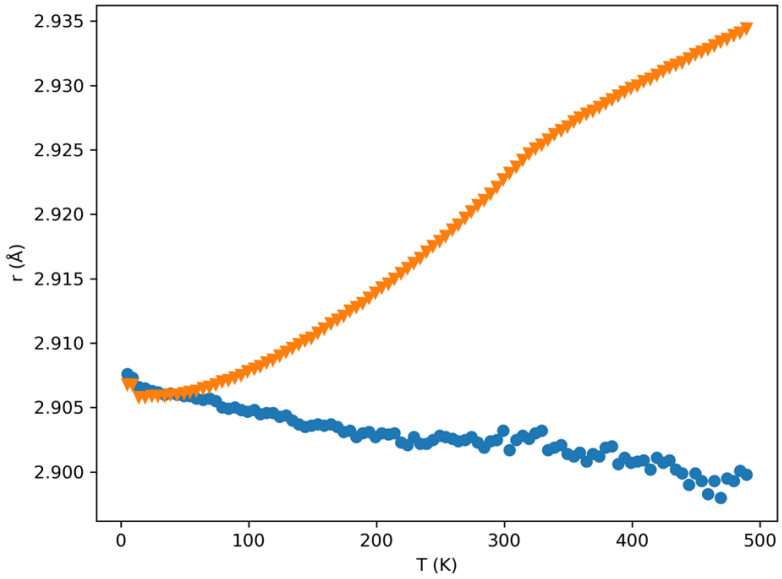

Figure 6.4 Variation of the position of the first peak maximum of the experimental xPDF data $G(r)$ and the calculated xPDF pattern G_{cal} with temperature. Blue symbol represents the position of peak maxima of experimental xPDF pattern, and orange symbol represents the position of peak maxima of calculated pattern of first peak.

the nearest-neighbor Mn-Te bond for four of the Mn atoms and lengthen it for the other two Mn atoms in the triangular prism. This would explain the slight shifting of the experimental peak to lower r and the asymmetric broadening. To test this idea, we performed a fit over the range 1.5 – 3.5 Å using a model where the Te atoms were allowed to shift in this manner. The unit cell dimensions remained fixed to the values determined from the longer range fits, since they cannot be refined reliably over the 1.5 – 3.5 Å fitting range. In Fig. 6.6(a) and (b), we show the fit with the undistorted model and the distorted model, respectively. The distorted model describes the data significantly better, capturing the shift of the peak maximum to lower *r*and the slight asymmetric broadening. A local off-centering of the Te ion, qualitatively similar to the emphanitic distortions in other thermoelectrics, is therefore consistent with the PDF data. We would expect this local distortion to contribute to the favorable thermoelectric figure of merit in MnTe by disrupting heat transport via phonons, effectively reducing the thermal conductivity and increasing zT.

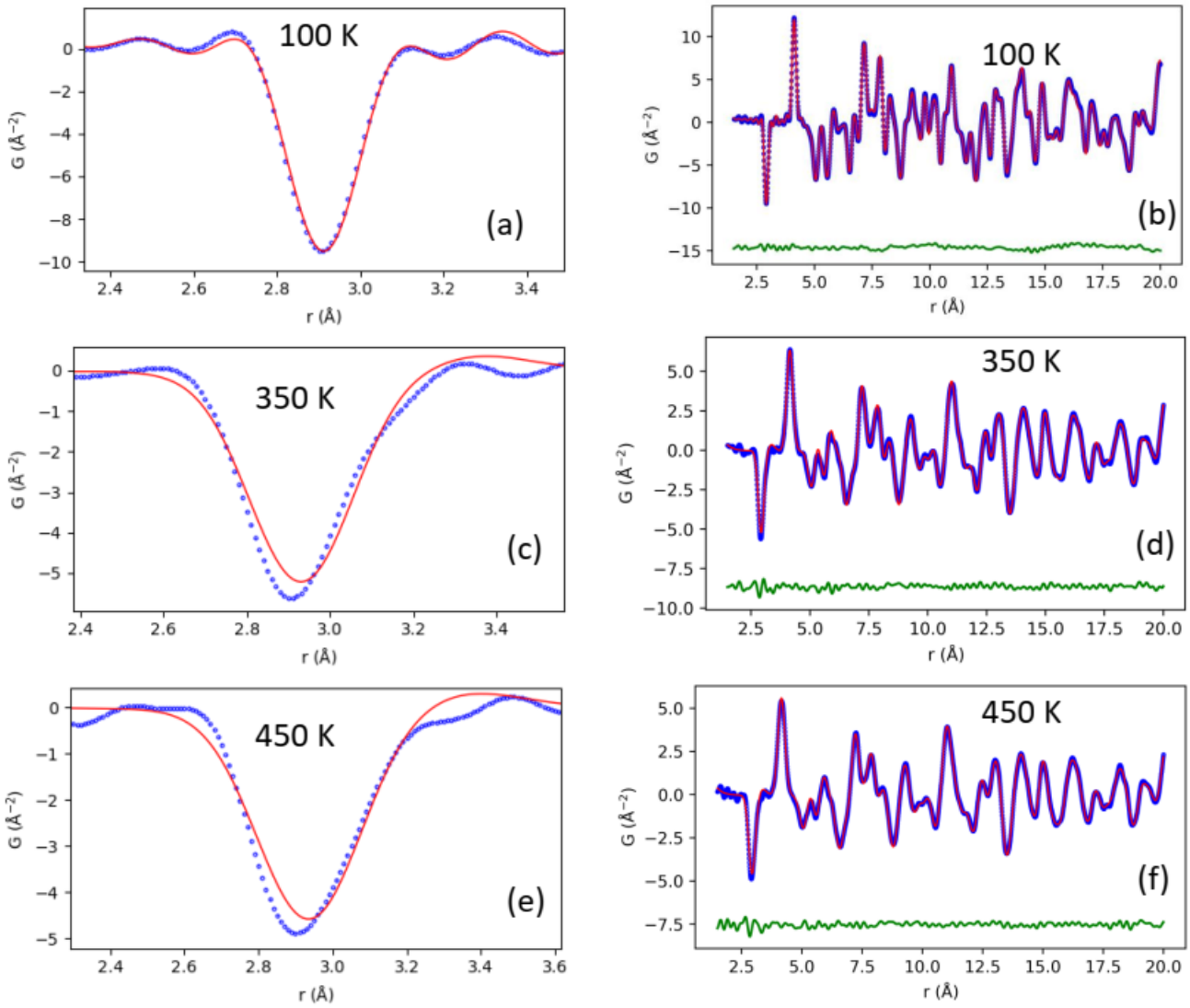

Figure 6.5 Neutron PDF (nPDF) fits of MnTe. Blue open circles represent the experimental nPDF data and the red solid line represents the calculated PDF fits using the $P63/mmc$ model. The green curve (offset for clarity) is the fit residual. Right panel graphs show the nPDF fits over the range 1.5 - 20 Å at 100K, 250 K, and 450 K, respectively, while the left panel graphs show the zoomed-in figure of first nearest neighbor peak at those same temperatures.

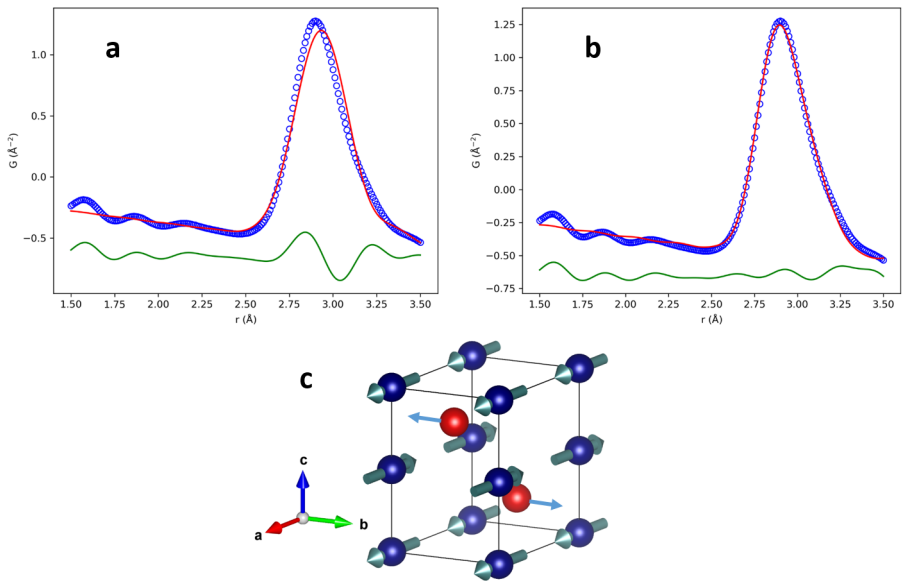

Figure 6.6 X-ray PDF fit for MnTe at 400 K over the range 1.5 – 3.5 Å using a distorted model where the Te atoms shift off center. (a) Fit with the undistorted model. (b) Fit with the distorted model. (c) Representation of the local distortion, with the arrows indicating the direction of the Te atom displacements.

To investigate the possibility of such an emphanisis-like distortion in other materials without any lone pairs, we performed comparative fits on other Mn-based materials, the antiferromagnetic cubic systems MnO (data source [70]; used with permission) and MnS (data source [86]; used with permission). Fig. 6.7 (b) shows the xPDF fit for MnS at 295 K, and a zoomed-in view of the first peak is shown in Fig. 6.7 (a). Similarly, Fig. 6.7 (d) shows the nPDF fit to MnO at 300 K, with a zoomed-in view of the first peak in Fig. 6.7 (c). We can clearly see that both compounds show very similar distortions as MnTe.

The origin of this distortion in the antiferromagnetic binary compounds MnTe, MnO, and MnS cannot be explained in terms of lone pair dynamics as observed in PbTe and other emphanitic materials. Another possibility is a magnetic origin, considering that the three examples we have found so far are all antiferromagnetic compounds. However, this is somewhat difficult to reconcile with the fact that the distortion increases with temperature and shows no clear response to the

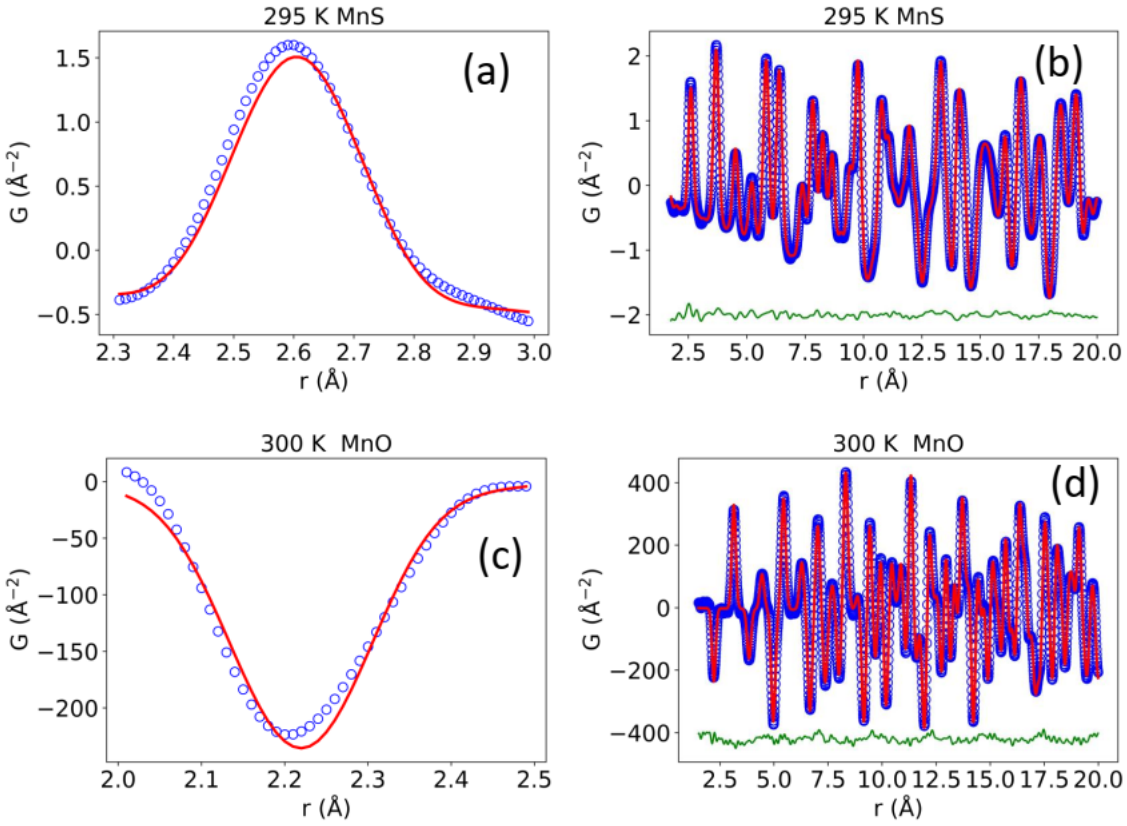

Figure 6.7 Local distortion in MnS and MnO. (a) xPDF fit to MnS at 295 K zoomed into the first peak, and (b) shown over the full fitting range. (c, d) Same as (a, b), but for MnO using neutron PDF data at 300 K.

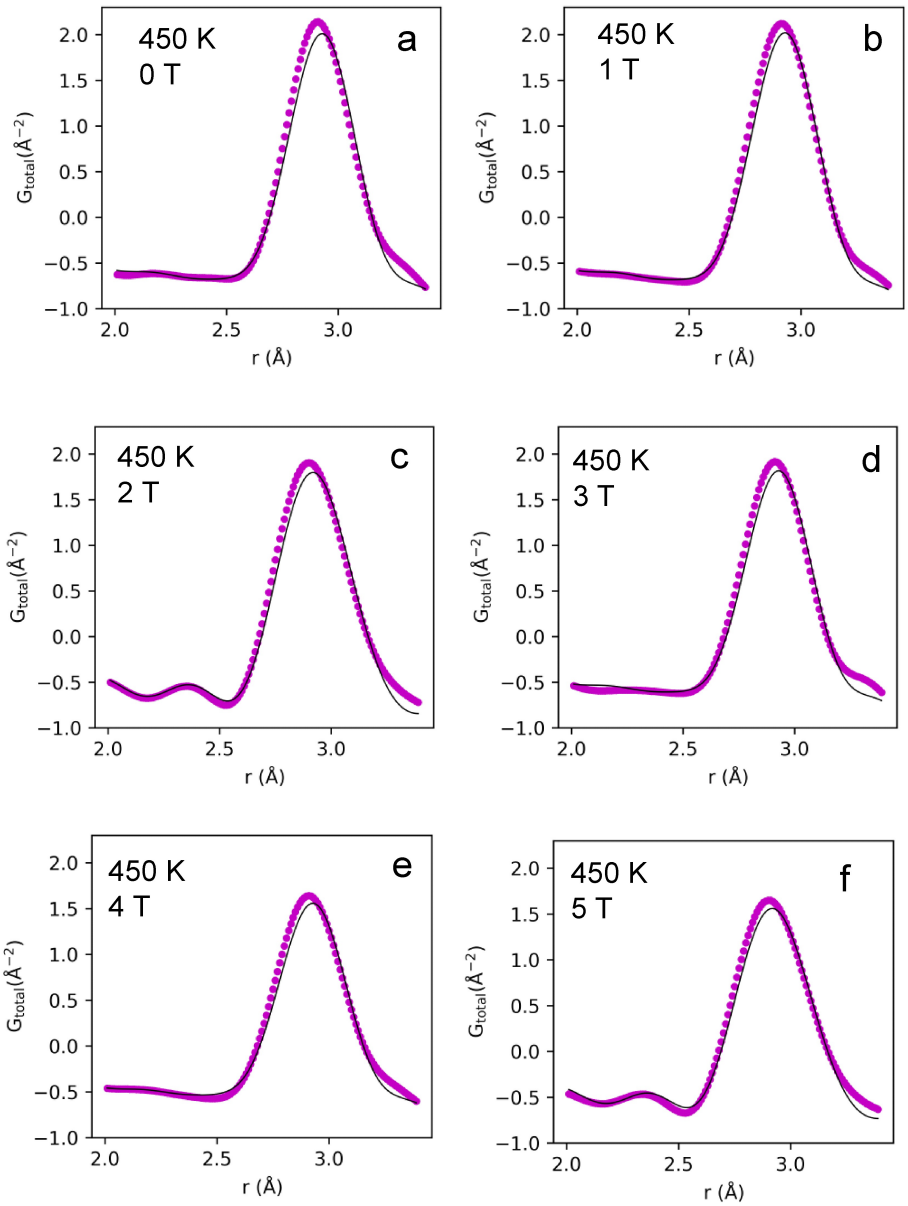

Figure 6.8 xPDF plots of the first peak of MnTe at various magnetic fields at 450 K.

antiferromagnetic ordering temperature. Furthermore, we measured the X-ray PDF for MnTe in applied magnetic fields up to 5 T, and we saw no systematic change in the local distortion with field (see Fig. 6.8.) We note that 5 T may not be a large enough field to significantly affect the internal behavior of the antiferromagnetic interactions in MnTe, so this does not disprove a magnetic

origin. To investigate this further, it will be important to measure nonmagnetic compounds like NiAs and perform theoretical calculations to determine whether magnetic exchange interactions or other factors could lead to the observed local distortion.

6.5 Conclusion

In summary, we observed a local distortion in MnTe that grows with temperature and can be described by an off-centering of the Te atoms, similar to the emphanisis phenomenon observed in other thermoelectric materials. A similar type of local distortion is observed in other Mn-based antiferromagnets MnS and MnO. The precise origin of this distortion in the Mn compounds requires further investigation.

Chapter 7

Conclusion

This thesis comprises three different projects on MnTe which were studied using atomic and magnetic pair distribution function analysis. Our magnetic pair distribution function analysis along with theoretical calculations revealed the real-space picture of the short-range correlations in the paramagnetic state. We have shown that robust, short-range magnetic correlations persist on the nanometer scale well above the Néel temperature, consistent with the paramagnon picture proposed to explain the high value of thermoelectric figure of merit. These short-range magnetic correlations are anisotropic, with a longer correlation length along the *c*-axis than in the *ab*-plane. *Ab initio* calculations using the DLM-DFT-SIC method predict the observed anisotropic magnetic correlations with quantitative accuracy, validating the approach of the theoretical study of magnetically enhanced thermoelectric materials.

A detailed picture of the magnetostrutrual response in MnTe was revealed by combining magnetic pair distribution function and atomic X-ray pair distribution function results. We have demonstrated that the spontaneous volume contraction was nearly 1%, which is the largest spontaneous volume contraction observed so far for any antiferromagnetic material. We also showed that the lattice strain couples linearly with the local magnetic order parameter, in contrast to the quadratic coupling observed for the conventional magnetostriciton.

Finally, by combining the atomic neutron and X-ray pair distribution function analysis, we revealed a local distortion in MnTe that increases with the increase in temperature due to the off-centering of Te atoms. This is very similar to the local distortion known as emphanisis in numerous other thermoelectric systems, yet it is the first time such behavior has been observed in a hexagonal system without any lone pairs. This type of distortion is also expected to enhance the thermoelectric figure of merit by decreasing the thermal conductivity. We have shown a similar local distortion in other Mn-based system, MnS and MnO, although the precise origin of this distortion require further investigation.

These results on local magnetic correlations, magnetostructural coupling, and local distortions in MnTe provide a vital benchmark for further understanding and optimizing the spin-driven thermoelectric enhancement due to short-range magnetic order in MnTe and other magnetic semiconductors, as well as fully understanding and exploiting the magnetostructural properties of MnTe.

The study of the local atomic and magnetic structure of materials with PDF methods revealed important features that would not be observed from conventional diffraction analysis, highlighting the value of taking a local structure view of scientifically and technologically relevant materials. It is also striking that even a chemically and structurally simple compound like MnTe exhibits such unexpectedly rich and complex behavior, imbuing the field of materials physics with continued excitement about the ongoing discovery of interesting and useful properties of matter.

Bibliography

[1] C. A. Young and A. L. Goodwin, "Applications of pair distribution function methods to contemporary problems in materials chemistry," Journal of Materials Chemistry **21,** 6464–6476 (2011).

[2] T. Peake, "Paramagnetic spins take electrons for a ride, produce electricity from heat," (September 13, 2019).

[3] Y. Zheng *et al.*, "Paramagnon drag in high thermoelectric figure of merit Li-doped MnTe," Science advances **5,** eaat9461 (2019).

[4] S. J. Billinge, "The rise of the X-ray atomic pair distribution function method: a series of fortunate events," Philosophical Transactions of the Royal Society A **377,** 20180413 (2019).

[5] J. Neuefeind, M. Feygenson, J. Carruth, R. Hoffmann, and K. K. Chipley, "The nanoscale ordered materials diffractometer NOMAD at the spallation neutron source SNS," Nuclear Instruments and Methods in Physics Research Section B: Beam Interactions with Materials and Atoms **287,** 68–75 (2012).

[6] B. Frandsen, X. Yang, and S. J. Billinge, "Magnetic pair distribution function analysis of local magnetic correlations," Acta Crystallographica Section A: Foundations and Advances **70,** 3–11 (2014).

[7] R. Baral *et al.*, "Real-space visualization of short-range antiferromagnetic correlations in a magnetically enhanced thermoelectric," Matter **5,** 1853–1864 (2022).

[8] M. Dutta, K. Pal, M. Etter, U. V. Waghmare, and K. Biswas, "Emphanisis in Cubic (SnSe) 0.5 (AgSbSe2) 0.5: Dynamical Off-Centering of Anion Leads to Low Thermal Conductivity and High Thermoelectric Performance," Journal of the American Chemical Society **143,** 16839–16848 (2021).

[9] T. Proffen, S. Billinge, T. Egami, and D. Louca, "Structural analysis of complex materials using the atomic pair distribution function—A practical guide," Zeitschrift für Kristallographie-Crystalline Materials **218,** 132–143 (2003).

[10] M. W. Gaultois, T. D. Sparks, C. K. Borg, R. Seshadri, W. D. Bonificio, and D. R. Clarke, "Data-driven review of thermoelectric materials: performance and resource considerations," Chemistry of Materials **25,** 2911–2920 (2013).

[11] S. Twaha, J. Zhu, Y. Yan, and B. Li, "A comprehensive review of thermoelectric technology: Materials, applications, modelling and performance improvement," Renewable and sustainable energy reviews **65,** 698–726 (2016).

[12] J. Mao, G. Chen, and Z. Ren, "Thermoelectric cooling materials," Nature Materials **20,** 454–461 (2021).

[13] Q. Jiang, H. Yan, J. Khaliq, H. Ning, S. Grasso, K. Simpson, and M. J. Reece, "Large ZT enhancement in hot forged nanostructured p-type Bi 0.5 Sb 1.5 Te 3 bulk alloys," Journal of Materials Chemistry A **2,** 5785–5790 (2014).

[14] M. Bailyn, "Maximum variational principle for conduction problems in a magnetic field, and the theory of magnon drag," Physical Review **126,** 2040 (1962).

[15] F. Blatt, D. Flood, V. Rowe, P. Schroeder, and J. Cox, "Magnon-drag thermopower in iron," Physical Review Letters **18,** 395 (1967).

[16] M. M. H. Polash, F. Mohaddes, M. Rasoulianboroujeni, and D. Vashaee, "Magnon-drag thermopower in antiferromagnets versus ferromagnets," Journal of Materials Chemistry C **8,** 4049–4057 (2020).

[17] M. M. H. Polash, F. Mohaddes, M. Rasoulianboroujeni, and D. Vashaee, "Magnon-drag thermopower in antiferromagnets versus ferromagnets," Journal of Materials Chemistry C **8,** 4049–4057 (2020).

[18] B. Sherman, R. R. Heikes, and R. W. Ure Jr, "Calculation of efficiency of thermoelectric devices," Journal of Applied Physics **31,** 1–16 (1960).

[19] Y. Xu, W. Li, C. Wang, J. Li, Z. Chen, S. Lin, Y. Chen, and Y. Pei, "Performance optimization and single parabolic band behavior of thermoelectric MnTe," Journal of Materials Chemistry A **5,** 19143–19150 (2017).

[20] N. Kunitomi, Y. Hamaguchi, and S. Anzai, "Neutron diffraction study on manganese telluride," Journal de Physique **25,** 568–574 (1964).

[21] W. Szuszkiewicz, E. Dynowska, B. Witkowska, and B. Hennion, "Spin-wave measurements on hexagonal MnTe of NiAs-type structure by inelastic neutron scattering," Physical Review B **73,** 104403 (2006).

[22] V. Baltz, A. Manchon, M. Tsoi, T. Moriyama, T. Ono, and Y. Tserkovnyak, "Antiferromagnetic spintronics," Reviews of Modern Physics **90,** 015005 (2018).

[23] T. Jungwirth, X. Marti, P. Wadley, and J. Wunderlich, "Antiferromagnetic spintronics," Nature nanotechnology **11,** 231–241 (2016).

[24] D. Kriegner *et al.*, "Multiple-stable anisotropic magnetoresistance memory in antiferromagnetic MnTe," Nature communications **7,** 1–7 (2016).

[25] J. Allen, G. Lucovsky, and J. Mikkelsen Jr, "Optical properties and electronic structure of crossroads material MnTe," Solid State Communications **24,** 367–370 (1977).

[26] S. Youn, B. Min, and A. J. Freeman, "Crossroads electronic structure of MnS, MnSe, and MnTe," physica status solidi (b) **241,** 1411–1414 (2004).

[27] Y. Ren, J. Yang, Q. Jiang, D. Zhang, Z. Zhou, X. Li, J. Xin, and X. He, "Synergistic effect by Na doping and S substitution for high thermoelectric performance of p-type MnTe," Journal of Materials Chemistry C **5,** 5076–5082 (2017).

[28] J. Dong, C.-F. Wu, J. Pei, F.-H. Sun, Y. Pan, B.-P. Zhang, H. Tang, and J.-F. Li, "Lead-free MnTe mid-temperature thermoelectric materials: facile synthesis, p-type doping and transport properties," Journal of Materials Chemistry C **6,** 4265–4272 (2018).

[29] M. M. H. Polash, D. Moseley, J. Zhang, R. P. Hermann, and D. Vashaee, "Understanding and design of spin-driven thermoelectrics," Cell Reports Physical Science **2,** 100614 (2021).

[30] M. G. Kanatzidis, "Nanostructured thermoelectrics: The new paradigm?," Chemistry of materials **22,** 648–659 (2010).

[31] T. Dietl and H. Ohno, "Dilute ferromagnetic semiconductors: Physics and spintronic structures," Reviews of Modern Physics **86,** 187 (2014).

[32] T. Egami and S. J. Billinge, *Underneath the Bragg peaks: structural analysis of complex materials* (Newnes, 2012).

[33] B. A. Frandsen and S. J. Billinge, "Magnetic structure determination from the magnetic pair distribution function (mPDF): ground state of MnO," Acta Crystallographica Section A: Foundations and Advances **71,** 325–334 (2015).

[34] N. Roth, A. F. May, F. Ye, B. C. Chakoumakos, and B. B. Iversen, "Model-free reconstruction of magnetic correlations in frustrated magnets," IUCrJ **5,** 410–416 (2018).

[35] S. W. Lovesey, *Theory of neutron scattering from condensed matter. Vol. 1. Nuclear scattering* (United Kingdom, 1984).

[36] D. S. Sivia, *Elementary scattering theory: for X-ray and neutron users* (Oxford University Press, 2011).

[37] F. S. Varley, "Neutron scattering lengths and cross sections," Neutron news **3,** 29–37 (1992).

[38] E. H. Kisi and C. J. Howard, *Applications of neutron powder diffraction* (Oxford University Press, 2012), Vol. 15.

[39] P. Juhás, C. L. Farrow, X. Yang, K. R. Knox, and S. J. Billinge, "Complex modeling: a strategy and software program for combining multiple information sources to solve ill posed structure and nanostructure inverse problems," Acta Crystallographica Section A **71,** 562–568 (2015).

[40] F. Ye, Y. Liu, R. Whitfield, R. Osborn, and S. Rosenkranz, "Implementation of cross correlation for energy discrimination on the time-of-flight spectrometer CORELLI," Journal of applied crystallography **51,** 315–322 (2018).

[41] O. Arnold *et al.*, "Mantid—Data analysis and visualization package for neutron scattering and μ SR experiments," Nuclear instruments and methods in physics research section a: accelerators, spectrometers, detectors and associated equipment **764,** 156–166 (2014).

[42] J. Weng, E. D. Dill, J. D. Martin, R. Whitfield, C. Hoffmann, and F. Ye, "K-space algorithmic reconstruction (KAREN): a robust statistical methodology to separate Bragg and diffuse scattering," Journal of Applied Crystallography **53,** 159–169 (2020).

[43] T. Weber and A. Simonov, "The three-dimensional pair distribution function analysis of disordered single crystals: basic concepts," (2012).

[44] X. Yang, P. Juhas, C. L. Farrow, and S. J. Billinge, "xPDFsuite: an end-to-end software solution for high throughput pair distribution function transformation, visualization and analysis," arXiv preprint arXiv:1402.3163 (2014).

[45] M. McDonnell, D. Olds, K. Page, J. Neufeind, M. Tucker, J. Bilheux, W. Zhou, and P. Peterson, "ADDIE: ADvanced DIffraction Environment—a software environment for analyzing neutron diffraction data," Acta Crystallogr. Sect. A **73,** a377 (2017).

[46] C. Farrow, P. Juhas, J. Liu, D. Bryndin, E. Božin, J. Bloch, T. Proffen, and S. Billinge, "PDFfit2 and PDFgui: computer programs for studying nanostructure in crystals," Journal of Physics: Condensed Matter **19,** 335219 (2007).

[47] B. Frandsen and S. J. Billinge, "Investigating short-range magnetic correlations in real space with the magnetic pair distribution function (mPDF)," Neutron News **27,** 14–16 (2016).

[48] N. Roth, F. Ye, A. F. May, B. C. Chakoumakos, and B. B. Iversen, "Magnetic correlations and structure in bixbyite across the spin-glass transition," Physical Review B **100,** 144404 (2019).

[49] B. A. Frandsen, P. K. Hamilton, J. A. Christensen, E. Stubben, and S. J. Billinge, "diffpy. mpdf: open-source software for magnetic pair distribution function analysis," Journal of Applied Crystallography 55 (2022).

[50] B. H. Toby and R. B. Von Dreele, "GSAS-II: the genesis of a modern open-source all purpose crystallography software package," Journal of Applied Crystallography **46,** 544–549 (2013).

[51] B. Gyorffy, A. Pindor, J. Staunton, G. Stocks, and H. Winter, "A first-principles theory of ferromagnetic phase transitions in metals," Journal of Physics F: Metal Physics **15,** 1337 (1985).

[52] I. Hughes, M. Däne, A. Ernst, W. Hergert, M. Lüders, J. Staunton, Z. Szotek, and W. Temmerman, "Onset of magnetic order in strongly-correlated systems from ab initio electronic structure calculations: application to transition metal oxides," New Journal of Physics **10,** 063010 (2008).

[53] D. H. Moseley *et al.*, "Giant doping response of magnetic anisotropy in MnTe," Physical Review Materials **6,** 014404 (2022).

[54] A. J. C. Wilson and V. Geist, "International Tables for Crystallography. Volume C: Mathematical, Physical and Chemical Tables. Kluwer Academic Publishers, Dordrecht/Boston/London 1992 (published for the International Union of Crystallography), 883 Seiten, ISBN 0-792-3-16-38X,", 1993.

[55] S. Blundell, *Magnetism in condensed matter*, 1st ed. (Oxford Series, New York, 2001), Vol. 29.

[56] J. Staunton, R. Banerjee, M. dos Santos Dias, A. Deák, and L. Szunyogh, "Fluctuating local moments, itinerant electrons, and the magnetocaloric effect: Compositional hypersensitivity of FeRh," Physical Review B **89,** 054427 (2014).

[57] I. Hughes, M. Däne, A. Ernst, W. Hergert, M. Lüders, J. Poulter, J. Staunton, A. Svane, Z. Szotek, and W. Temmerman, "Lanthanide contraction and magnetism in the heavy rare earth elements," Nature **446,** 650–653 (2007).

[58] E. Mendive-Tapia and J. B. Staunton, "Theory of magnetic ordering in the heavy rare earths: Ab initio electronic origin of pair-and four-spin interactions," Physical Review Letters **118,** 197202 (2017).

[59] C. E. Patrick and J. B. Staunton, "Rare-earth/transition-metal magnets at finite temperature: Self-interaction-corrected relativistic density functional theory in the disordered local moment picture," Physical Review B **97,** 224415 (2018).

[60] C. E. Patrick and J. B. Staunton, "Temperature-dependent magnetocrystalline anisotropy of rare earth/transition metal permanent magnets from first principles: the light R Co 5 (R= Y, La-Gd) intermetallics," Physical Review Materials **3,** 101401 (2019).

[61] M. Lüders, A. Ernst, M. Däne, Z. Szotek, A. Svane, D. Ködderitzsch, W. Hergert, B. Györffy, and W. Temmerman, "Self-interaction correction in multiple scattering theory," Physical Review B **71,** 205109 (2005).

[62] E. Mendive-Tapia and J. B. Staunton, "Ab initio theory of the Gibbs free energy and a hierarchy of local moment correlation functions in itinerant electron systems: The magnetism of the mn 3 a materials class," Physical Review B **99,** 144424 (2019).

[63] J. Staunton and B. Gyorffy, "Onsager cavity fields in itinerant-electron paramagnets," Physical review letters **69,** 371 (1992).

[64] A. Fry-Petit, A. Rebola, M. Mourigal, M. Valentine, N. Drichko, J. Sheckelton, C. Fennie, and T. McQueen, "Direct assignment of molecular vibrations via normal mode analysis of the neutron dynamic pair distribution function technique," The Journal of Chemical Physics **143,** 124201 (2015).

[65] S. Mu, R. P. Hermann, S. Gorsse, H. Zhao, M. E. Manley, R. S. Fishman, and L. Lindsay, "Phonons, magnons, and lattice thermal transport in antiferromagnetic semiconductor MnTe," Physical Review Materials **3,** 025403 (2019).

[66] P. W. Anderson, "Theory of magnetic exchange interactions: exchange in insulators and semiconductors," in *Solid state physics* (Elsevier, 1963), Vol. 14, pp. 99–214.

[67] J. Staunton, S. Ostanin, S. Razee, B. Gyorffy, L. Szunyogh, B. Ginatempo, and E. Bruno, "Temperature dependent magnetic anisotropy in metallic magnets from an ab initio electronic structure theory: L 1 0-ordered FePt," Physical review letters **93,** 257204 (2004).

[68] S. Ostanin, A. Ernst, L. Sandratskii, P. Bruno, M. Däne, I. Hughes, J. Staunton, W. Hergert, I. Mertig, and J. Kudrnovskỳ, "Mn-stabilized zirconia: from imitation diamonds to a new potential high-T c ferromagnetic spintronics material," Physical review letters **98,** 016101 (2007).

[69] J. D. Aldous, C. W. Burrows, A. M. Sánchez, R. Beanland, I. Maskery, M. K. Bradley, M. dos Santos Dias, J. B. Staunton, and G. R. Bell, "Cubic MnSb: Epitaxial growth of a predicted room temperature half-metal," Physical Review B **85,** 060403 (2012).

[70] B. A. Frandsen, M. Brunelli, K. Page, Y. J. Uemura, J. B. Staunton, and S. J. Billinge, "Verification of Anderson superexchange in MnO via magnetic pair distribution function analysis and ab initio theory," Physical Review Letters **116,** 197204 (2016).

[71] T. Krenke, E. Duman, M. Acet, E. F. Wassermann, X. Moya, L. Mañosa, and A. Planes, "Inverse magnetocaloric effect in ferromagnetic Ni–Mn–Sn alloys," Nature materials **4,** 450–454 (2005).

[72] N. A. Spaldin and M. Fiebig, "The renaissance of magnetoelectric multiferroics," Science **309,** 391–392 (2005).

[73] J. Ma, J. Hu, Z. Li, and C.-W. Nan, "Recent progress in multiferroic magnetoelectric composites: from bulk to thin films," Advanced materials **23,** 1062–1087 (2011).

[74] H. K. Singh, I. Samathrakis, N. M. Fortunato, J. Zemen, C. Shen, O. Gutfleisch, and H. Zhang, "Multifunctional antiperovskites driven by strong magnetostructural coupling," npj Computational Materials **7,** 1–9 (2021).

[75] E. Hristoforou and A. Ktena, "Magnetostriction and magnetostrictive materials for sensing applications," Journal of Magnetism and Magnetic Materials **316,** 372–378 (2007).

[76] A. Hammersley, "FIT2D V12. 012 Reference Manual V6. 0," ESRF International Report No. ESRF98HA01T. Program available at http://www. esrf. eu/computing/scientific/FIT2D (2004).

[77] T. Chatterji, G. N. Iles, B. Ouladdiaf, and T. C. Hansen, "Magnetoelastic effect in MF2 (M= Mn, Fe, Ni) investigated by neutron powder diffraction," Journal of Physics: Condensed Matter **22,** 316001 (2010).

[78] T. Chatterji and T. C. Hansen, "Magnetoelastic effects in Jahn–Teller distorted CrF2 and CuF2 studied by neutron powder diffraction," Journal of Physics: Condensed Matter **23,** 276007 (2011).

[79] Y. M. Oey, J. D. Bocarsly, D. Mann, E. E. Levin, M. Shatruk, and R. Seshadri, "Structural changes upon magnetic ordering in magnetocaloric AlFe2B2," Applied Physics Letters **116,** 212403 (2020).

[80] V. Zapf *et al.*, "Direct measurement of spin correlations using magnetostriction," Physical Review B **77,** 020404 (2008).

[81] E. S. Božin, C. D. Malliakas, P. Souvatzis, T. Proffen, N. A. Spaldin, M. G. Kanatzidis, and S. J. Billinge, "Entropically stabilized local dipole formation in lead chalcogenides," Science **330,** 1660–1663 (2010).

[82] R. Yu, E. S. Bozin, M. Abeykoon, B. Sangiorgio, N. A. Spaldin, C. D. Malliakas, M. G. Kanatzidis, and S. J. Billinge, "Emphanitic anharmonicity in PbSe at high temperature and anomalous electronic properties in the Pb Q (Q= S, Se, Te) system," Physical Review B **98,** 144108 (2018).

[83] K. Knox, E. Bozin, C. Malliakas, M. Kanatzidis, and S. Billinge, "Local off-centering symmetry breaking in the high-temperature regime of SnTe," Physical Review B **89,** 014102 (2014).

[84] D. H. Fabini *et al.*, "Dynamic stereochemical activity of the Sn2+ lone pair in perovskite CsSnBr3," Journal of the American Chemical Society **138,** 11820–11832 (2016).

[85] M. Saura-Múzquiz, F. P. Marlton, B. G. Mullens, A. M. Manjón-Sanz, J. C. Neuefeind, M. Everett, H. E. Brand, S. Mondal, G. Vaitheeswaran, and B. J. Kennedy, "Understanding the Re-entrant Phase Transition in a Non-magnetic Scheelite," Journal of the American Chemical Society **144,** 15612–15621 (2022).

[86] J. K. Clark, V. Yannello, A. M. Samarakoon, C. Ross, M. C. Uible, V. O. Garlea, and M. Shatruk, "Inelastic Neutron Scattering Study of Magnetic Exchange Pathways in MnS," The Journal of Physical Chemistry C **125,** 16183–16190 (2021).